EXPERIMENTAL AND CFD SIMULATION OF A MULTIPHASE CANNED MOTOR PUMP

A Dissertation

by

WENFEI ZHANG

Submitted to the Office of Graduate and Professional Studies of
Texas A&M University
in partial fulfillment of the requirements for the degree of

DOCTOR OF PHILOSOPHY

Chair of Committee,	Gerald L. Morrison
Committee Members,	Debjyoti Banerjee
	Je-Chin Han
	Robert Randall
Head of Department,	Andreas A. Polycarpou

December 2016

Major Subject: Mechanical Engineering

ABSTRACT

Canned motor pumps are well suited for pumping hazardous and radioactive fluids due to their compact design and low maintenance cost. However, their application on artificial lift has not been investigated yet. ESP (Electric Submersible Pump) has been used as an artificial lift method for pumping high volume flow rate in deep wells. However, due to its seal leaking and bearing abrasive problems, pump performance is deteriorated during operation. This work investigated utilizing a canned motor pump instead of ESP in downhole application. The performance of a canned motor pump under multiphase flow was studied experimentally and computationally.

A canned motor pump demonstrator manufactured by Curtiss-Wright EMD was installed in the pump test loop built at Turbomachinery Laboratory at Texas A&M University. The water baseline performance test and multiphase flow (water/air) test was performed. GVF (Gas Volume Fraction) in pump stator jacket was varied from 0% to 20%, and the pump speed varied from 2000 RPM to 3930 RPM. The pump's performance at these flow conditions was recorded and learned.

The air inside the bearing house and rotor-stator annulus causes cooling and lubrication problems for normal pump operation. The air distribution of the secondary circulation flow inside the pump is the main concern. Thus, multiphase flow inside the pump was simulated with CFD commercial code, ANSYS Fluent. Different GVF with different water flow rate was simulated. Also, pressure at flow region outlet and bubble diameter

effect were also simulated. Flow rate distribution trend predicted by CFD method is validated by experimental test results.

Impedance probe was designed and built to measure multiphase flow in a pipe. The GVF is the main calibrated parameter. The fluid's dimensionless admittance was found to have linear correlation with GVF. The phase of CPSD from probe's signal is a promising calibration tool for the future probe application.

DEDICATION

To my wife, parents and sister

ACKNOWLEDGEMENTS

I would like to thank Dr. Gerald Morrison as my supervisor for all his tremendous help, support and guidance in the completion of this work. It was a great working experience under his supervisory. His kindness and trust, expertise and patience encouraged me to pursue the unknown truth in the engineering world. I will always remember his advice for the rest of my life. Thanks also goes to my committee members, Dr. Banerjee, Dr. Han and Dr. Randall, for their support and advice throughout the research.

I also wants to appreciate Dr. Stuart Scott and Hector Casillas from Shell Inc. for providing financial support for this project. Eric Conaway, Ryan Mesiano and Jose Matos from Curtiss Wright EMD provided a lot of technical support before and during the pump testing. I would like to thank them for their help and knowledge.

Also, I would like to thank my colleagues in Turbomachiney lab during my PhD study. They are Dr. Sahand Pirouzanah, Dr. Min-Hsiu Chien, Dr. Abhay Patil, Dr. Sujan Reddy, Dr. Peng Liu, Yong Zheng, Yi Chen, Yintao Wang, Changrui Bai, Yiming Chen, Ke Li, Joey Marchetti, Ted Hatch, Clayton Kirkland, Dezhi Zheng, Daniel Steck, Andrew Johnson, Craig Nolen, Gautham and Dohar.

Last, I need to thank my family. My wife Jingyuan, who is also studying her PhD, always gives me support and encouragement whenever I feel frustrated. Her patience and love will lead us to the bright future. I thank my parents, Yulian and Ping, for their selfless devotion and love. Without them, it is impossible for me to complete this work.

NOMENCLATURE

ESP	Electrical Submersible Pump
GVF	Gas Volume Fraction
IATE	Interfacial Area Transport Equation
MUSIG	Multiple-size-group
CFD	Computational Fluid Dynamics
BWR	Boiling Water Reactor
Y	Admittance of a material
k_g	Geometry factor
κ	Electrical conductivity
ω	Angular frequency
ε_0	Permittivity of vacuum
ε_r	Relative permittivity of fluid
V_0	Measured output voltage
V_i	Excitation voltage

Y_f	Admittance of feedback loop
Y_M	Admittance of measured fluids
R	Resistance
C	Capacitance
X_C	Reactance
Z	Impedance
G	Conductance
B	Susceptance
X(f)	Fourier Transform of x(t)
Y(f)	Fourier Transform of y(t)
x(t)	Time series
y(t)	Time series
Sxx	Auto-correlation of x(t)
Sxy	Cross-correlation of y(t)
CPSD	Cross Power Spectral Density
ϕ	Phase of Cross Power Spectral Density

ε_r^*	Complex relative permittivity
P&ID	Pipe and Instrumentation Diagram
GPM	Gallons per Minute
RPM	Reciprocal per Minute
SCFM	Standard Cubic Feet per Minute
NPT	National Pipe Thread
VFD	Variable Frequency Drive
Q_{motor}	Flow rate passing motor can
$Q_{statorjacket}$	Flow rate passing stator jacket
Q_{inlet}	Flow rate at pump inlet
$DP_{Venturi}$	Differential pressure between stator jacket and Venturi throat
C_d	Discharge coefficient
x	Quality of mixture
$\dot{m}$	Mass flow rate
$DPT-140$	Differential pressure at venturi
k	Turbulent kinetic energy

ε	Turbulent kinetic energy dissipation rate
u_i	Fluid total velocity at direction i
$\overline{u}_i$	Mean velocity in time
u_i'	Fluctuation velocity
μ	Dynamic viscosity
μ_t	Turbulent viscosity
$\bar{p}$	Mean pressure
δ_{ij}	Kronecker delta
G_k	Generation of turbulence kinetic energy due to mean velocity gradient
G_b	Generation of turbulence kinetic energy due to buoyancy
β	Coefficient of thermal expansion
c	Speed of sound
M_t	Turbulent Mach number
U^*	Dimensionless velocity
y^*	Dimensionless distance from wall

U_P	Mean velocity of the fluid at the wall-adjacent cell centroid P
k_P	Turbulence kinetic energy at the wall-adjacent cell centroid P
y_P	Distance from the centroid of wall-adjacent cell P to the wall
V_q	Volume occupied by phase q
α_q	Volume fraction of phase q
$\hat{\rho}_q$	Effective density of phase q
$\vec{v}_q$	Velocity of phase q
$\dot{m}_{pq}$	Mass transfer from pth to qth phase
$\bar{\bar{\tau}}_q$	qth phase stress-strain tensor
$\vec{F}_q$	External body force
$\vec{F}_{lift,q}$	Lift force
$\vec{F}_{wl,q}$	Wall lubrication force
$\vec{F}_{vm,q}$	Virtual mass force
$\vec{F}_{td,q}$	Turbulent dispersion force
$\bar{R}_{pq}$	Interaction force between phases

$\dot{m}_{pq}\vec{v}_{pq}$	Momentum transfer between phase p and phase q
h_q	Specific enthalpy of the qth phase
$\vec{q}_q$	Heat flux
Q_{pq}	Intensity of heat exchange between pth and qth phase
h_{qp}	Enthalpy between phase exchange
η	Pump Efficiency
P_{motor}	Pump Motor Consumed Power

TABLE OF CONTENTS

Page

LIST OF FIGURES

Page

LIST OF TABLES

Page

1. INTRODUCTION

A canned motor pump is a combination of a centrifugal pump and a canned motor. This combination was first used in chemical plants for economic reasons, as it avoids leaking expensive fluid into the environment. Later, as the regulations on environment became stricter, canned motor pumps were developed to circulate toxic, radioactive and environmentally hazardous fluid in industry applications. Due to its seal-less design, the canned motor pump has advantages of maintenance free and low cost.

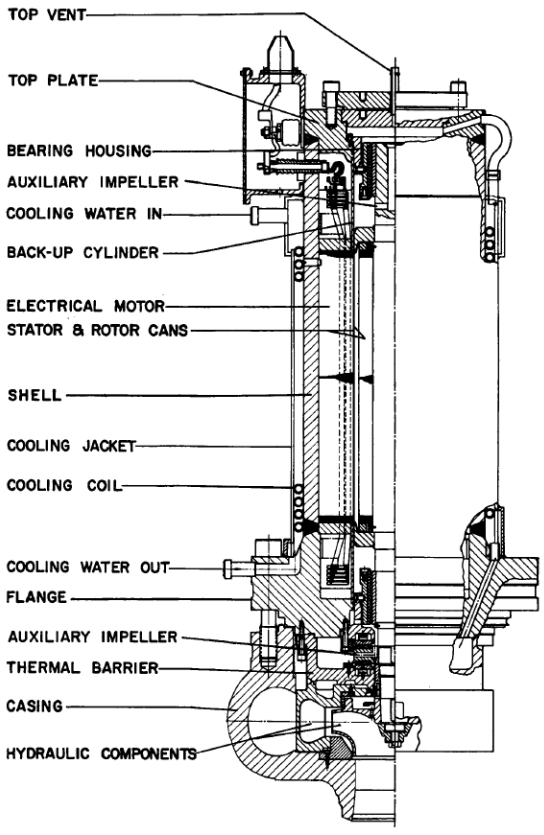

Figure 1-1: Canned Motor Pump (Hagen 1969)

Canned motor pump design is composed of a one stage or multi stage impeller, diffuser passage, canned motor, cooling jacket and bearings. An early design of this kind of pump is shown in Figure 1-1. One part of the pumped fluid is directed through the gap between rotor and stator to cool the motor and lubricate the bearings. At the same time, external cooling water is circulated through the pump jacket to cool the pumping fluid. The can is the crucial part that separates the rotating shaft from stationary motor winding. The can needs to be as thin as possible for high motor efficiency and as thick as necessary for strength and safe operation.

Artificial lift method is widely used in oil and gas. When the well pressure decreases during the production of oil and gas, the fluid cannot overcome the pressure losses flowing from the bottom to the well head. Thus more hydraulic head will be needed to keep the well productive.

There are three kinds of artificial lift methods: gas lift, jet pumping and pumping. Gas lift method injects high pressure gas (water vapor or air) into well fluids to reduce the density of the fluid. Thus, the pressure head that the fluid needs to overcome pressure from the bottom hole to the top is reduced. The remaining pressure at bottom then can push the liquid/gas mixture up to well head. Jet pumping is a method that uses the Venturi effect that fluid accelerates when passing through a Venturi shaped passage. Water is pumped from well surface into the well tube, passing through a Venturi pipe to form a high velocity jet flow. The jet flow then is mixed with oil and flows through a diffuser to change kinematic energy to pressure head. Thus, the oil is pumped along with the jet pumped fluid.

Pumping is another way of hydraulic lift method. Usually this method can be divided into rod and rod-less pumping. The rod pumping methods utilize a string of rods connecting the downhole pump to the well surface. The downhole pump is usually a positive displacement pump, which is also known as rod sucker pump. The rod sucker pump is driven by a surface motor and walk beam which converts the rotary movement to reciprocating movement of the rod. The rod-less pumping does not need a rod string, while it is driven by other means such as electrical or hydraulic. ESP utilizes a submerged electrical motor and a rod-less pump which could be centrifugal, positive displacement or hydraulic types. The motor is connected to the surface power through an electric cable. The ESP method is suitable for pumping high liquid volume in deep wells.

Figure 1-2 compares the differences between these three types of methods in terms of maximum liquid production rate versus lifting depth. As shown in the graph, gas lift can generate most liquid across a wide range of well depth.

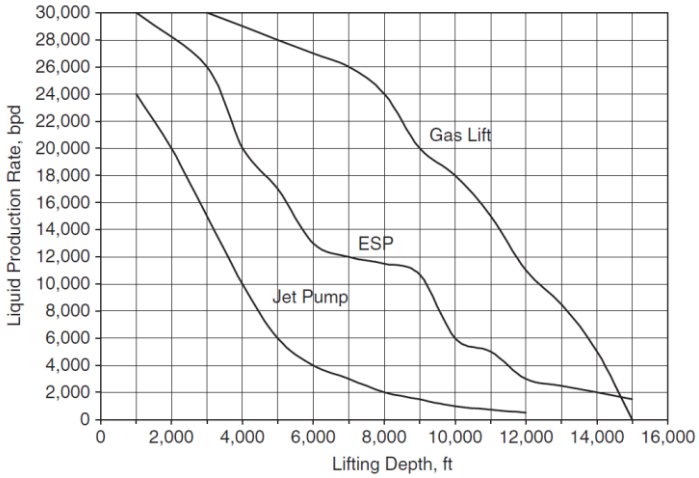

Figure 1-2: Maximum Liquid Production Rates vs Lifting Depth (Takacs 2009)

1.1 Literature Review

1.1.1 Canned Motor Pump

O. Hagen (Hagen 1969) introduced a canned motor pump design, the working principle, manufacturing problems, and problems analysis. The canned motor pump specification is 16000 gal/min and a head of 356 ft at speed of 1800 rpm. Figure 1-3 shows the pumps cross section view. Circulation flow inside the motor is designed to cool the motor heat loss and the heat load from pumped fluid. Material stress analysis also should be considered as internal pressure and thermal stress could cause bolts fatigue. Another problem of canned motor pump is can fatigue caused by thermal cyclic during start-up and shut-down and for speed changing. Since the can length could be expanded after being heated and under internal pressure, the can always undergoes strain stress and buckling could happen. The can material is usually Hastelloy or Inconel. Hagen pointed out that for the same can thickness, the fatigue life of Hastelloy can is longer than that of an Inconel can.

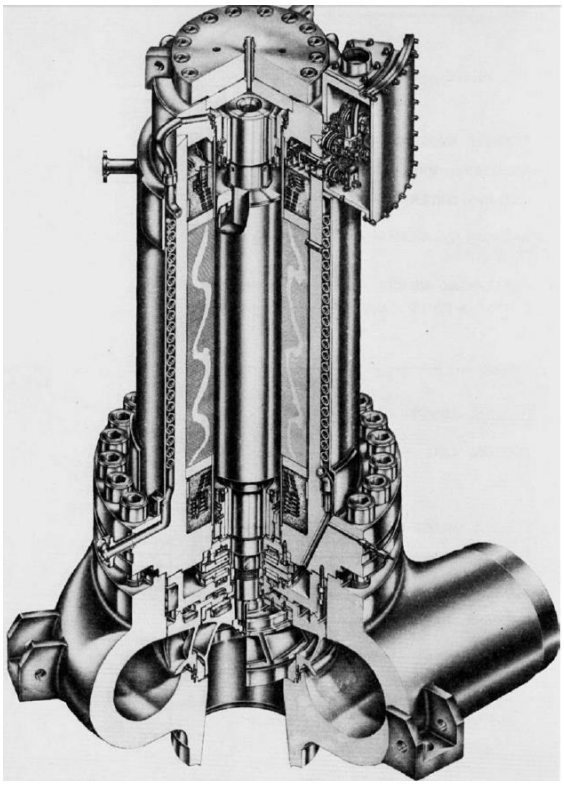

Figure 1-3: Cross Section of Canned Motor Pump (Hagen 1969)

In 1967, Michael Stark and George Bollibon applied for patent No. 3475631 (Stark and Bollibon 1967). The authors invented a gas cooling features for canned motor pump. Figure 1-4 shows a cross section of a canned motor pump. The air can be blown from 128 through the stator assembly housing then away from 134. The stator assembly is designed to have six longitudinal bars and a plurality of annular laminations 24. These radial slots are fin-shaped, thus effectively strengthens cooling of the stator winding. Also, the invention has a passageway for liquid cooling. The circulating fluid can flow through the thrust bearing assembly 82 to the rotor cavity 26 and piping 144. The latter fluid will go

up to the upper journal bearing assembly. The secondary impeller 18 can suck the fluid to the can cavity to cool the rotor.

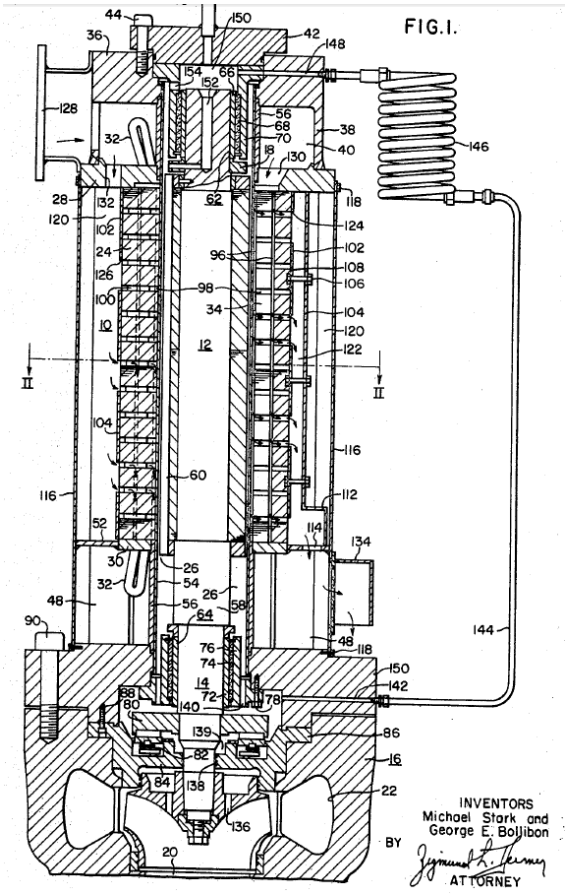

Figure 1-4: New Design of Cooling Passage(Stark and Bollibon 1967)

In another patent (Thomas and Michael 1967), Thomas Heathcote and Michael Stark invented a replaceable stator can assembly. By welding two rings at each end of the stator can, engineers can pull the stator can to the right position inside the pump to seal rotor winding and pumping fluid. Thus, the stator can will be able to be replaced in field, rather than sent back to factory for maintenance. The authors also designed the assembling way

of the canned motor pump, which allows the pump to be disassembled and repaired in the field.

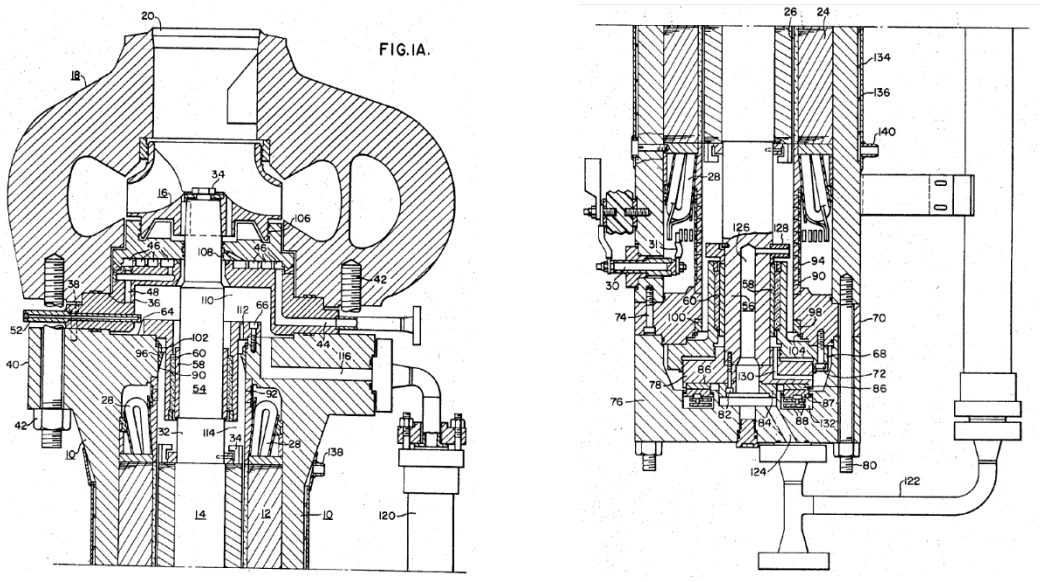

Figure 1-5: Top and Bottom Bearing House(Thomas and Michael 1967)

Jian Li (Li, Song et al. 2010) studied the thermal analysis of a canned induction motor with consideration of eddy current loss. The author used the time-step finite element method to analyze the electromagnetic field of a canned motor. Thus, the eddy current loss was calculated, which is the source of the motor heat load. Then the temperature field was conducted through finite element method.

Alexandrina Untaroiu (Alexandrina Untaroiu 2009) simulated the annulus flow region between the stator and can rotor in a canned motor pump. The author compared two methods for calculating the rotor dynamics coefficients: the bulk-flow method developed by Fritz and 3D CFD method. Both methods modeled the annulus region between the rotor

can and the stator without pre-swirl and axial component. CFD method can validate the bulk flow method. In addition, CFD method simulated the case with axial flow component and pre-swirl inlet flow condition. The results show the direct stiffness terms are negative in all cases, and decreases in magnitude. This trend is not captured by the bulk flow method. Moreover, the effect of direct stiffness, cross-couple stiffness and direct damping on the rotor stability needs further investigation.

R. Kisner (Kisner, D. Fugate et al. 2013) introduced a canned rotor pump with both magnetic bearing and highly integrated I&C (Instrumentation and Control) for a nuclear power plant to pump liquid metal. The author identified the materials availability for building this canned rotor pump assembly, the manufacture methods and electrical control methods. This canned rotor pump design has the following advantages: 1. Embedded sensors and control will help pump operation more robust in nuclear power plant. 2. Integrated design combines materials, electronics, thermal management, mechanics, hydraulics, sensors and control at the first stage of product development. 3. Compared with currently used induction pump, centrifugal pumps has higher efficiency.

A.V. Ruddy (Ruddy 1980) analyzed the effect of journal bearing with helical grooves on the stability of a vertical canned motor pump. In this canned motor pump, external water is injected at the top of pump to lubricated two journal bearings in the can cavity. Back pressure is kept high enough so that pumped process fluid will not flow back into can cavity. The author build a finite element model to analyze the rotor bearing system of the canned motor pump. The lateral analysis of rotor shows that a two groove bearings fitted

in the top shaft position will be beneficial for stable operation of the rotor system. However, this configuration also may cause process fluid flowing back into lubricated water.

Thus, the above limited canned motor pump research literatures shows that multiphase flow in canned motor pump has not been well studied. The multiphase flow distribution inside the canned motor pump will affect the pump's performance, reliability and failure life. The bearings under multiphase flow and motor cooling by internal flow will be an interesting topic to investigate. All these topics will provide a fundamental understanding for utilizing the canned motor pump as ESP.

1.1.2 CFD of Multiphase Flow

Multiphase flow exists generally in many engineering applications. In oil and gas industry, multiphase flow coming from underground is three-phase flow: liquid phase of water/oil, gas phase of natural gas and solid phase of sand. After two phase flow characteristic is studied, pump under three-phase flow should be tested. In this paper, only gas/liquid mixture (two-phase) flow is concerned for preliminary research purpose. The gas/liquid flow can be grouped into several flow regime types based on phase phenomenological distribution. In Figure 1-6, the flow regime map is generated by Mandhane in 1974 (Mandhane, Gregory et al. 1974) for a horizontal pipe flow. The flow regime map provides researchers a quantitative way of organizing different flow patterns and finding respective research methods for them.

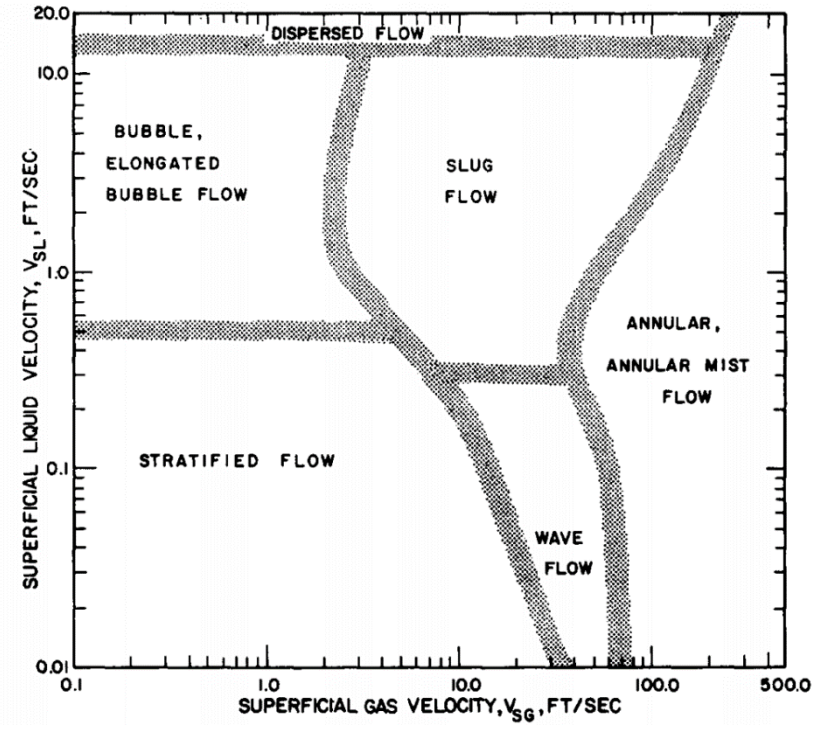

Figure 1-6: Flow Regime Map(Mandhane, Gregory et al. 1974)

In Figure 1-7, the air-water flow patterns in a vertical pipe are recorded. From left to right, the flow patterns are bubbly flow, cap flow, slug flow, churn-turbulent flow and annular flows, respectively.

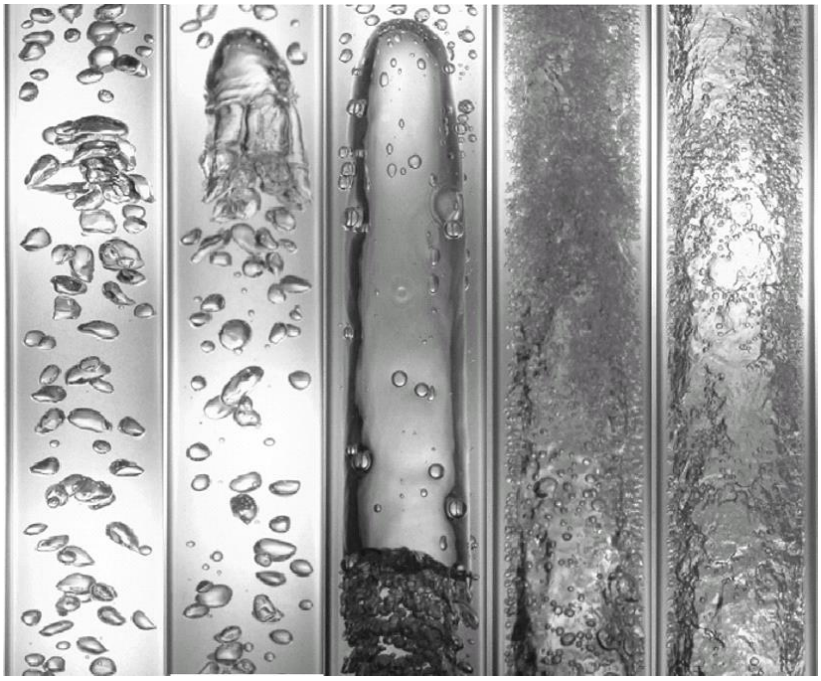

Figure 1-7: Typical Air-water Flow Images in a Vertical Pipe(Ishii 2011)

Ishii (Ishii 1971) built a two-fluid model for bubbly multiphase flow. This two-fluid model treats two phase independently with two groups of conservation equations. The water is regarded as a continuous phase and air is the dispersed phase which penetrates into water. In a later published paper, Ishii investigated the drag force effect on air bubbles. The author found that the drag force based on mixture viscosity plays an important role in predicting relative motions of interfacial phase (Ishii and Zuber 1979).

Since then, the two-fluid model has been developed as the most popular model in computational model for multiphase flow, which is also known as an Eulerian-Eulerian model. Based on this model, conservation of mass, conservation of momentum and conservation of energy stands for each phase until the phase interface. Then several

closure models are developed to cover the phase interfacial transport (mass, momentum and energy). The forces exerting on the dispersed bubbles, which adversely changes the flow pattern, have been investigated during the past 40 years.

D. Lucas (Lucas, Krepper et al. 2007) investigated a set of bubble forces models to calculate the radial gas volume fraction profiles for vertical pipe flow. Based on a very detailed experimental database obtained from a sophisticated measuring method, the measured radial gas volume fraction profile was compared with the one calculated from the force models. According to the author, a combination of the Tomiyama lift force, Tomiyama wall force and Faver averaged turbulent dispersion force was found to provide best fit with the experimental data. However, when liquid superficial velocities are higher than 1 m/s, the force models are not able to describe the shift of the peak of gas volume fraction away from the wall.

Xia Wang and Xiaodong Sun (Wang and Sun 2009) simulated an adiabatic upward bubbly flow using Fluent. The authors implemented a group of "interfacial area transport equation (IATE)" into Fluent two-fluid model. The IATE consists of the following bubble interaction mechanisms: the coalescence of bubbles due to random collisions driven by liquid phase turbulence, the coalescence of bubbles due to wake entrainment and bubble disintegration due to turbulent eddy impact. By comparing with experimental results and simulation data, the one-group implemented IATE shows good agreement in predicting void fraction, interfacial concentration and bubble Sauter mean diameter. However, the author also pointed out that IATE would not predict wall region void fraction and

interfacial area concentration. Wall lubrication model and negative lift force coefficient should be added in the source term of momentum equation in the further study.

Liao and Lucas (Liao, Lucas et al. 2011) developed a new model for inhomogeneous MUSIG (Multiple-size-group) model. The homogeneous MUSIG model was first proposed by Lo (Lo 1996), in which the diameter range of bubble size is divided into M size groups. In this model, it is assumed that all bubbles travel with a common gas velocity. The inhomogeneous MUSIG model was first proposed by Krepper, in which the bubble is divided firstly into N velocity groups. Then, each velocity group is divided into a set of sub-group based on different bubble sizes. There are already many standard bubble breakup and coalescence models which have been developed during the past 10 years, among which are the breakup kernel function developed by Luo and Svendsen in 1996 (Luo and Svendsen 1996), coalescence kernel function developed by Prince and Blanch in 1990 (Prince and Blanch 1990). The author developed a new breakup and coalescence kernel functions, in which the breakup model considers turbulence fluctuation, velocity shear and interfacial friction force, and the coalescence model considers turbulence fluctuation, laminar shear, wake-entrainment and eddy-capture. This new model is implanted into ANSYS CFX 12.0 via subroutines code to simulate upward bubbly flow in a pipe. By comparing with experimental data, the new model result shows better agreement than that of standard model in concerning of gas bubble size distribution. However, both models cannot predict well the transition region from bubbly flow to churn-turbulent flow. Thus the model will need to be further improved.

Stephen Yamoah et al (Yamoah, Martinez-Cuenca et al. 2015) investigated models for drag, lift, wall lubrication and turbulent dispersion forces for simulation of bubbly flow in a vertical pipe. The authors pointed out that suitable closure models (interphase forces) should be selected for simulating the momentum exchanges between bubbles and liquid. Among those interphase forces, the drag force, lift force, wall lubrication force and turbulent dispersion force affected mainly the accuracy of the CFD simulation. And also, there are many force models that have been developed and widely used. A set of these force models is selected and implemented in the ANSYS CFX solver. By comparing with experimental results, the author studied the simulation results in the following aspects: the gas volume fraction profile, interfacial area concentration, gas velocity and liquid velocity. Then, the applicability of these force models is investigated. According to the author, a set of composed of a Grace drag coefficient model, a Tomiyama lift coefficient model, Antal et al.'s wall force model, and Favre averaged turbulent dispersion force was found to have best agreement with experimental data. However, the author also pointed out the limitation of these models. For example, the drag coefficient model is based on the assumption of bubble moving in quiescent liquid scenario. And also the simulation is based on an assumption of fully developed bubbly flow region. Thus, the breakup and coalescence are not taken into account.

Roland Rzehak (Rzehak and Kriebitzsch 2015) built a multiphase adiabatic bubbly flow model in vertical pipes with OpenFOAM, and compared the results with experimental data from Liu and MTloop. Based on a successful model on a commercial code ANSYS CFX, the author rebuilt it in OpenFOAM. The simulation results from OpenFOAM shows good

similarity compared with that of ANSYS CFX. The model's prediction of radial profiles of liquid velocity and gas velocity fit well with experimental data from Liu and MTloop. However, comparing with Liu's data, for square root of turbulent kinetic energy, the model result over-predicted data at center of pipe, and under-predicted it near wall region. Concerning gas volume fraction profile, the model did not predict well near the wall region comparing with MTloop data. Thus, the author suggests further multiphase model study should be performed considering the near wall bubble forces.

1.1.3 Multiphase Flow on a T-junction

For this canned motor pump multiphase test, multiphase flow diverts inside the canned motor. There exists a T-junction when flow passes from stator jacket annulus to the pump discharge pipe. The side branch is vertical downwards, and part of fluid in main path flows into pump thrust bearing cavity. Thus, the multiphase flow redistribution at this T-junction will affect the thrust bearing performance and motor cooling capacity. Here we introduce the previous research on multiphase flow passing a T-junction causing different pressure drop and phase redistribution in downstream.

Azzopardi (Azzopardi and Whalley 1982) founded that flow patterns of two-phase flow affects the flow distribution in a Tee junction. Bubbly flow, churn flow and annular flow were compared for horizontal and vertical Tee. The author concluded that local flux momentum variance is a reason that diverts gas and liquid. However, these conclusions are based on specific flow range and pipe geometry.

When upstream flow patterns are annular and stratified flow, splitting flow rate in main flow pipe and side branch is studied in (Shoham, Brill et al. 1987), (Shoham, Arirachakaran et al. 1989) and (Azzopardi and Smith 1992). Both experimental and theoretical methods are applied. The theoretical model can agree well with experimental for same diameter and reduced diameter branch.

Hwang (Hwang, Soliman et al. 1988) studied phase separation in T and Y junction experimentally and analytically. The phenomenological model showed good agreement with the experimental results only for similar diameter side branch. Mudde (Mudde, Groen et al. 1993) studied the effect of pipe geometry on phase separation in a large T-junction. An industrial-scale flow rig was built to study the flow redistribution and pressure drop of two-phase flow splitting in a horizontal upward reduced T-junction. Experimental results revealed that both upstream flow pattern and downstream geometry plays an important role in determining phase redistribution.

For inlet flow regimes of stratified, wavy, slug and annular flow, the phase distribution and pressure drop data are presented in (Buel, Soliman et al. 1994) for a horizontal equal-sided tee junction. The data showed good agreement with data and models in other literatures. In (Charron and Whalley 1995), the author reported gas-liquid annular flow redistribution at a vertical tee junction with horizontal outlet. Walters (Walters, Soliman et al. 1998) extended the experiment result of (Buel, Soliman et al. 1994) to cases with reduced tee junctions. Also, the experiment results can agree with models developed by Azzopardi.

By far, the annular flow and stratified flow on a T-junction has been well researched. However, bubbly flow on a T-junction is not fully investigated both experimentally and theoretically. Considering this canned motor pump's application, it is applicable to model the bubbly flow in a horizontal Tee with downward reduced side branch with CFD method.

1.1.4 Impedance Needle Probe

Measuring multiphase flow rate is important for many engineering industry, such as in nuclear power plant and oil&gas well testing. There are many literature reviews (Corneliussen 2005, Powell 2008, Silva 2008) covering the multiphase flow measurement techniques. Thus, the multiphase flow meter types are introduced here briefly. Based on measurement principles, the multiphase flow meter can be grouped into:

(1) Electromagnetic measurement principles: capacitance and conductance meter
(2) Gamma ray attenuation densitometer
(3) Differential pressure type using Venturi or V-cone
(4) Cross-section void fraction tomography: Electrical Resistance Tomography, X-ray or neutron tomography, Magnetic Resonant Imaging

Among all these methods, the capacitance and conductance meter is a cheap, safe and quick responsive method comparing with other measuring types. The impedance needle probe can measure the liquid's impedance or permittivity. As permittivity is related to GVF of multiphase flow, the impedance probe can act as a multiphase flow meter. Here, only needle shaped impedance probe research is introduced. Other shaped probes like ring

or plate electrodes were studied in the past two decades (Andreussi, Di Donfrancesco et al. 1988, Fossa 1998, Devia and Fossa 2003).

Uga (Uga 1972) designed a digital void meter and bubble speed meter for measuring bubble-size distribution in an operating BWR (Boiling Water Reactor). The digital void meter's drawing is shown in Figure 1-8. The author established an integral equation to describe the relationship of void signal and bubble size. Then, the normalized bubble frequency vs bubble diameter diagram can be depicted, which measured the bubble-size distribution in the reactor.

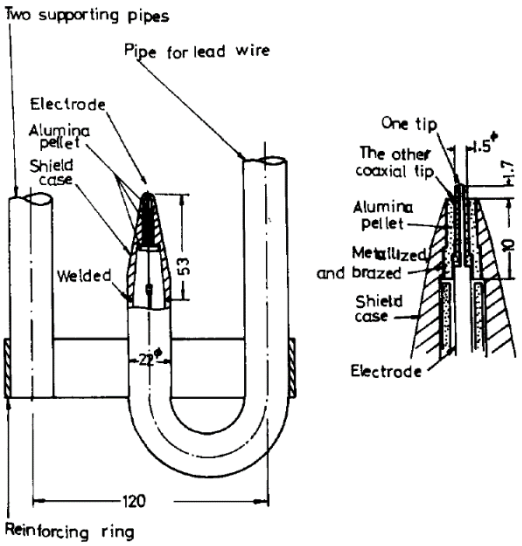

Figure 1-8: Details of Digital Void Meter(Uga 1972)

Da Silva (Silva, Schleicher et al. 2007) designed a novel needle probe to measure complex permittivity of multiphase flow. There are two types of electrode sensors used in the study in Figure 1-9. Probe 1 has larger probe tip, thus is more likely to capture bubbly flow characteristics. Probe 2's smaller tip is unlikely to cause disturbance in the flow, but would

be insensitive to the small bubbles. Thus, probe 2 was used to measure mixing process of water and isopropanol. The electronics apply a sinusoidal voltage to the excitation electrode, and then the measure electrode voltage is amplified through an op-amp and measured in amplitude and phase detector.

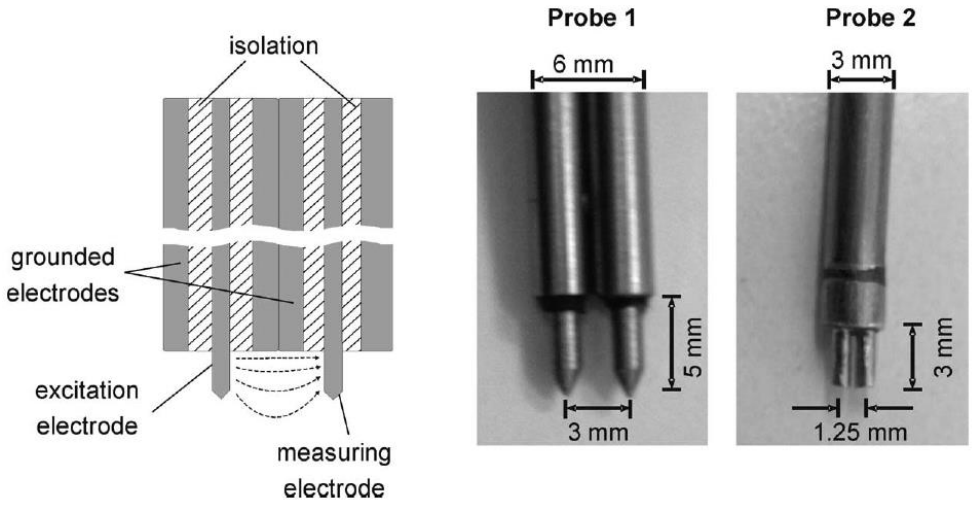

Figure 1-9: Details of Separated Impedance Needle Probe(Silva, Schleicher et al. 2007)

The admittance of a material is determined as:

$$Y = k_g(\kappa + j\omega\varepsilon_0\varepsilon_r) \qquad 1.1$$

The geometry factor k_g reflects the ratio of the area sampled fluid volume and distance between electrodes. κ is the electrical conductivity; ε_0 is the permittivity of vacuum; ε_r is relative permittivity of the fluids at tip (it is a temperature-dependent dielectric constant); ω is the angular frequency. The measured output voltage from the amplifier is used to calculate the admittance.

$$V_0 = V_i \frac{Y_M}{Y_f} \tag{1.2}$$

Y_f is the admittance in the feedback loop of the op-amp; V_i is the excitation voltage; Y_M is the admittance of measured fluids. The complex relative permittivity ε_r^* is defined as:

$$\varepsilon_r^* = \varepsilon_r + \frac{\kappa}{j\varepsilon_0\omega} \tag{1.3}$$

Thus, admittance and complex relative permittivity can be connected by:

$$Y = k_g j\omega\varepsilon_0\varepsilon_r \tag{1.4}$$

According to the author, the complex relative permittivity change can be detected when there is bubble passing through the probe tip, as shown in Figure 1-10 and Figure 1-11.

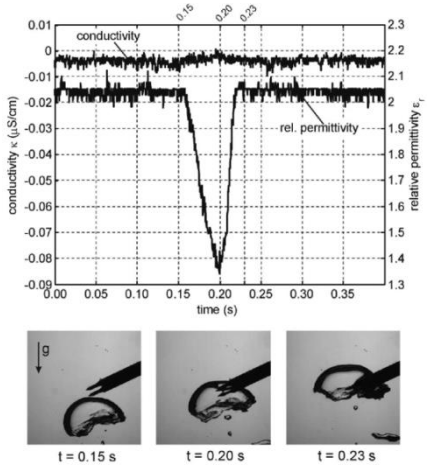

Figure 1-10: Air Bubbles in Water

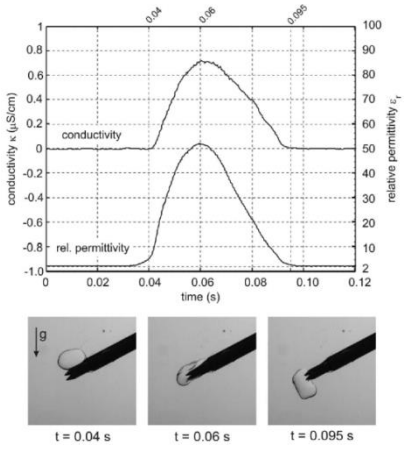

Figure 1-11: Water Droplet in Gasoline

Schleicher (Schleicher, Silva et al. 2008) developed a new thermoneedle probe measuring system for multiphase flow instrumentation. The detail of the probe is shown in Figure

1-12. The sheathed thermocouple can measure the fluid temperature with time constant of 3.6 ms. By applying AC voltage between the measuring electrode and reference electrode, the phase change upon the probe tip can be detected.

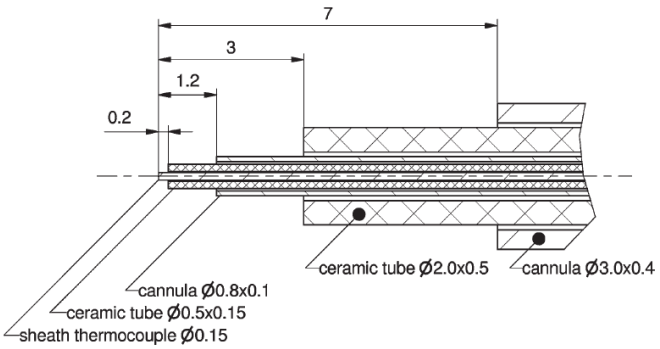

Figure 1-12: Details of Dual Modularity Thermoneedle Probe(Schleicher, Silva et al. 2008)

Another advantage of this design is that it can distinguish the condensable and non-condensable bubbles. The condensable gas bubble will cause both temperature change and conductivity change, while non-condensable gas bubble will only cause conductivity change. Figure 1-13 shows the result.

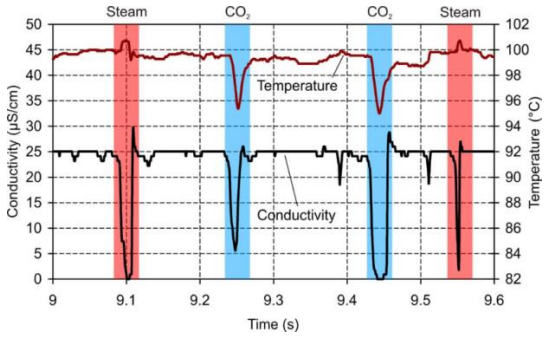

Figure 1-13: Conductivity and Temperature Response to Phase Change

Luke Munholand (Munholand and Soucy 2005) compared four conductive needle probe designs for measuring bubble velocity and local gas void fraction. The effect of probe size and geometry are studied. The author found that probe size with 2 mm shows the best results due to its excellent signal-to-noise ratio. It is noted that here only one condition is tested with global gas fraction hold 0.018 and mean bubble velocities at 0.296 m/s.

Paranjape (Paranjape, Ritchey et al. 2012) used an electrical impedance meter to measure void fraction in microchannel two-phase flow. The impedance meter is calibrated against the time-averaged void fraction determined from flow visualization. Also, the probability density function of the time series signal from impedance meter is utilized for determining the flow regimes. Thus, the impedance meter can be used to measure the void fraction and distinguish flow regime transition for the microchannel flows.

Hogsett (Hogsett and Ishii 1997) measured local void fraction, local interfacial area concentration, bubble interfacial velocity and Sauter mean diameter with a double sensor probe method. Also, the liquid velocity and turbulent intensity are measured with a hot-film anemometry. The double sensor probe is an electrical conductance probe that can detect bubble passing between two needle electrodes. The local void fraction up to 0.07 and interfacial area concentration from 5 to 160 1/m are measured. In this paper, the superficial gas velocity is 0.067 m/s and the superficial liquid velocity is 1.3 m/s. With the measurement of interfacial area concentration and turbulent intensity, the closure model for two phase interfacial interaction can be completed.

Several impedance multiphase flow measurement devices have been designed and custom manufactured at Turbomachinery Lab, Texas A&M University. Sahand (Sahand Pirouzpanah 2013) used a needle conductance probe to measure the local and temporal gas volume fraction. By counting the time that the air bubble travel between two needles, bubble velocity can be calculated. Sihombing (Sihombing 2015) used a pair of cylinder electrode flush-mounted on a PVC pipe wall. The output gain of the circuit is correlated with known GVF and temperature. Thus, a regression curve is obtained with respect to GVF and electrodes gain at different frequencies.

In the 1990s, Dr. Gerald Morrison began to research the slotted orifice plate as a better alternative to standard orifice flow meter. He found that the slotted orifice flow meter has better tolerance to the irregularity of upstream velocity profile when measuring the air flow (Morrison, Hall et al. 1994) . And also for the same flow pass area, the slotted orifice plate has less total head loss compared to the standard orifice flow meter. Gerald Morrison and Dwayne (Morrison, Terracina et al. 2001) studied the slotted orifice plate pressure drop coefficient under wet gas condition. It was found that the KY factor is only a function of flow quality over a range of air flow rates. Gautham (Annamalai, Pirouzpanah et al. 2016) studied the homogenization effect of a slotted orifice plate by using ERT system at different downstream positions. It is found that, by using a beta=0.467 slotted orifice plate, shown in Figure 1-14, the multiphase flow has best homogenization at 1.5D at the downstream of the slotted orifice plate.

Figure 1-14: Slotted Orifice Plate for Test

In this paper, an impedance needle probe coupled with a slotted orifice plate is applied to measure water/air mixture flow. Since the slotted orifice plate will break the long bubble columns into smaller bubbles, it acts as a gas/liquid homogenizer. Thus the needle probe can be used to measure the macroscopic GVF in the fluid without changing the probe position.

2. OBJECTIVE

In previous studies, the canned motor pump has never been considered as an alternative ESP for downhole application. However, the multiphase flow in the well is a big challenge for the canned motor cooling and safe operation. Thus, this work aims to research canned motor pump with respect to its application in multiphase flow, which will help its further development for oil and gas industry. The first step is to evaluate a canned motor pump performance under different operating conditions. Motor temperature history, pump hydraulic head, and pump thrust load is studied with multiphase flow. Also, the multiphase flow inside the pump will be simulated in commercial CFD code.

To study the canned motor pump performance under multiphase flow condition, a multiphase flow pump test rig is built. The pump is run with water, and air is injected into pump stator jacket during test. Pump performance data is recorded for different fluid flow rates, different GVF and different pump speeds.

To better understand the multiphase flow distribution inside the canned motor pump, a CFD model is built to simulate the internal circulation multiphase flow with ANSYS Fluent. Multiphase turbulence flow model is applied to simulate the flow under different pump operation conditions. GVF distribution and gas velocity profile will predict the air concentration in the thrust bearing housing. The CFD results of predicting flow distribution trend inside the canned motor pump can be validated by experimental results by analyzing the Venturi multiphase flow test results.

3. METHODOLOGY

3.1 Experimental Setup

3.1.1 Test Rig

Test rig was built in Texas A&M University Turbomachinery Laboratory. Figure 3-1 shows the P&ID (Pipe and Instrumentation Diagram) of the whole test facility. Figure 3-2 shows the test pump as installed in the flow loop. The main flow loop of this test rig is described as: water is supplied from a charge pump which pumps water from an open water tank. Then it flows through the water control valve, canned motor pump and back pressure control valve then back to the tank. Compressed air is supplied by oil free screw compressors with a common reservoir. Air is injected into the pump at the stator jacket annulus, which is located between the diffuser and discharge of the pump.

There is also a secondary flow loop for cooling the pumping fluids. The water flow from the tank can be directed through a circulation pump to an air-fan heat exchanger (shown in blue line in Figure 3-1). By adjusting the air-fan motor speed, the water temperature can be stabilized at a desirable range. During this test, the ambient air temperature varied between 50 and 80 degree F. The water temperature varied between 75 and 100 degree F.

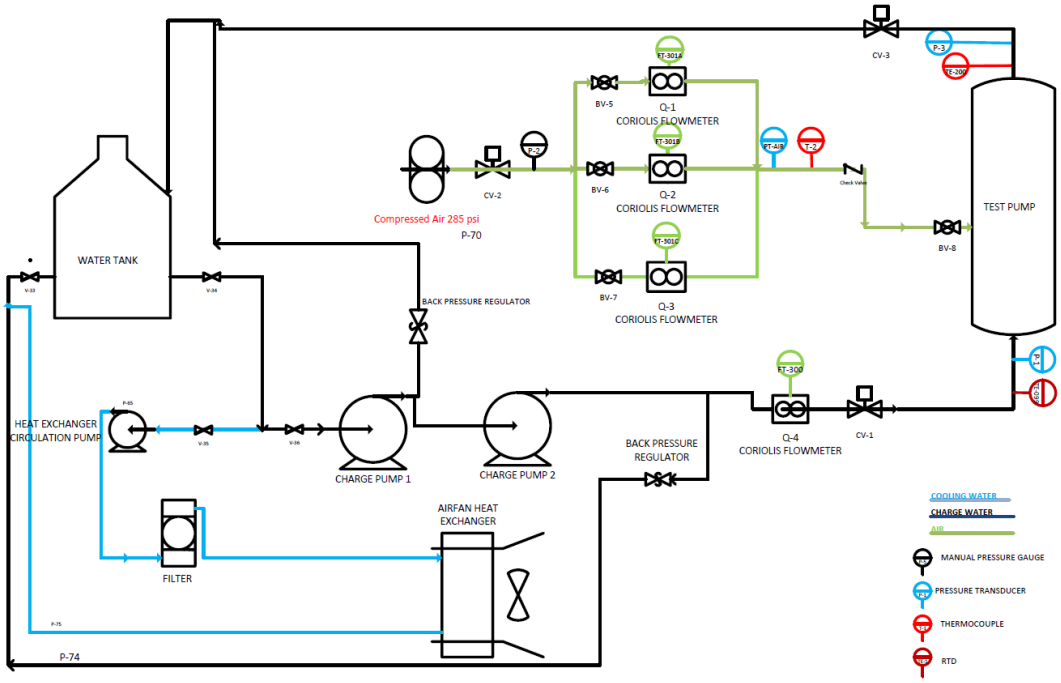

Figure 3-1: P&ID of the Canned Motor Pump Test

Fluid flow rate can be adjusted automatically by the Masoneilan Rotary Globe Control Valves remotely from computer program. Based on the target water flow rate and GVF, the pump was run at different speeds, and performance data was recorded.

Figure 3-2: Curtiss Wright Pump in Test Loop

3.1.2 Test Procedure

The canned motor winding is cooled by the internal circulation flow between the winding and pump shaft. Figure 3-3 shows the internal flow path of this pump when the performance test is applied. The motor cooling flow rate Q_{motor} is defined as:

$$Q_{motor} = Q_{statorjacket} - Q_{inlet} \quad 3.1$$

To measure the stator jacket flow rate, Curtiss Wright engineers designed a Venturi flow path in the stator jacket annulus. Under Venturi calibration test configuration of the pump, the internal flow path is blocked, which implies Q_{motor} equals to 0. Thus $Q_{statorjacket}$

equals to Q_{inlet}. By measuring the Venturi relative pressure (differential pressure across the Venturi passage), GVF, and Q_{inlet}, $Q_{statorjacket}$ can be calibrated by a function of these variables:

$$Q_{statorjacket} = f(DP_{Venturi}, \rho_{mixture}) \tag{3.2}$$

When multiphase flow passes a Venturi passage, there exists a relation:

$$\dot{m}_{mixture} = \frac{C_d}{\sqrt{1-\beta^4}} A_2 \sqrt{2\rho_{mixture}\Delta p} \tag{3.3}$$

Where the $\dot{m}_{mixture}$ is the total mixture mass flow rate passing the Venturi, A_2 is the cross sectional area of Venturi throat. $\rho_{mixture}$ is the density of homogeneous liquid/gas mixture. C_d is discharge coefficient. The equation 3.3 can be closed by the following equation group.

$$\begin{cases} \dot{m}_{mixture} = \dot{m}_{air} + \dot{m}_{water} \\ \Delta p = DP_{Venturi} + \rho_{mixture} g h \\ \rho_{mixture} = \dfrac{1}{\dfrac{x}{\rho_{air}} + \dfrac{1-x}{\rho_{water}}} \\ \beta = \sqrt{\dfrac{A_2}{A_1}} \\ x = \dfrac{\dot{m}_{air}}{\dot{m}_{air} + \dot{m}_{water}} \end{cases} \tag{3.4}$$

x is the quality of mixture, A_1 is the annulus area of stator jacket of canned motor pump. $DP_{Venturi}$ is the relative Venturi differential pressure measured by pressure transducer DPT-140. h is the height difference between the measured points at Venturi throat and

stator jacket annulus. Thus, discharge coefficient C_d can be calibrated by the Venturi calibration test.

After the Venturi calibration test, the pump was reconfigured to make internal flow path accessible. During performance test, the inlet water and air flow rate, temperature, pressure and $DP_{Venturi}$, were measured. Based on the equation 3.3, the $Q_{statorjacket}$ can be approximately predicted. The Q_{motor} can be calculated, although assumption has to be made that air volume in circulation flow is neglected.

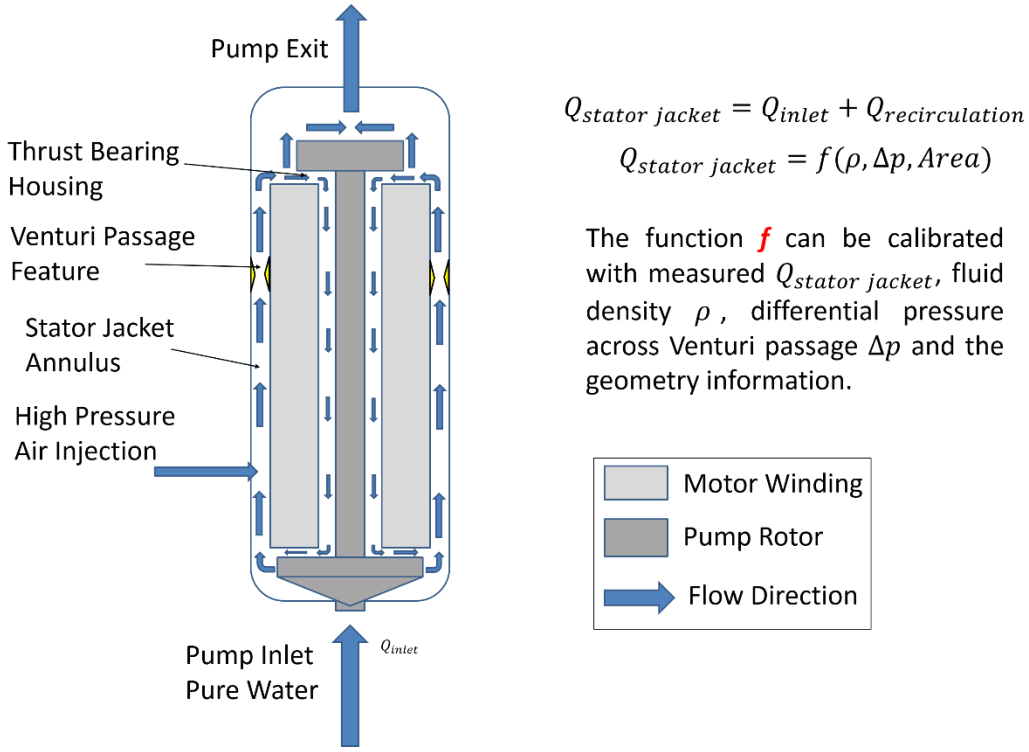

Figure 3-3: Curtiss Wright Canned Motor Pump Flow Sketch

The detailed pump performance test is described as:

Firstly, the water baseline test was performed under different pump speeds. The test matrix is shown in Table 3-1.

Speed (RPM)	Water flow rate (GPM)
2000	75
	100
	150
3000	75
	115
	130
	190
3930	150
	175
	200
	225
	250

Table 3-1: Test Matrix of Water Baseline Test

Secondly, air was injected into the stator jacket annulus under different operation conditions. The test matrix is show in Table 3-2.

Speed (RPM)	Water flow rate(GPM)	GVF %
2000	75	0
3000	100	3
3930	115	6
	130	9
	150	12
	175	15
	190	20
	200	
	225	
	250	

Table 3-2: Test Matrix of Multiphase Test

3.1.3 Instrumentations

There are four Coriolis flow meters installed in the flow loop as shown in Figure 3-1. One of them is installed in water line, and the other three in the air line. The three air flow meters cover a full range of air flow rate to satisfy experimental requirement. Each flow meter is equipped with a transmitter which converts vibration frequency signal to measurable 4-20 mA signal. Table 3-3 shows the details of all flow meters.

Flow meter	Model NO.	End Connection	Range	Minimum accuracy
Water	CMF300M	3” 150# Flange	25-1200 GPM	±0.25%
Air	CMF010M	1/4” NPT	0.5-14 SCFM	±0.35%
Air	CMFS040	1/2” 300# Flange	10-150 SCFM	±0.25%
Air	CMF100M	1” 300# Flange	100-500 SCFM	±0.35%

Table 3-3: List of Flow Meters

Pressure transducers and differential pressure transducers were installed on the pump to measure the pressure rise across the pump and the differential pressure among different portions of the pump. Figure 3-4 shows a sketch of the differential pressure transducers setup. 1/16” stainless steel tubes were used to connect the measuring positions on the pump to the transducer panel. Each differential pressure transducer has control valves on the high pressure side and the low pressure side. Valves are closed before the test begins

to protect the transducers from possible transient flow damage. Table 3-4 lists the models of differential pressure transducers and pressure transducers.

Label	Transducer Model	Range (psig)	Output	Accuracy
DPT-110	Omega-PX 429	0-30	4-20 mA	±0.08%
DPT-130	Omega-PX 429	0-50	4-20 mA	±0.08%
DPT-140	Omega-PX 429	0-30	4-20 mA	±0.08%
DPT-150	Omega-PX 429	0-50	4-20 mA	±0.08%
DPT-160	Omega-PX 429	0-15	4-20 mA	±0.08%
DPT-170	Omega-PX 429	0-150	4-20 mA	±0.08%
DPT-175	Omega-PX 429	0-150	4-20 mA	±0.08%
DPT-180	Omega-PX 429	0-50	4-20 mA	±0.08%
DPT-190	Omega-PX 429	0-500	4-20 mA	±0.08%
PT-110	Omega-PX 429	0-500	4-20 mA	±0.08%
PT-120	Omega-PX 429	0-500	4-20 mA	±0.08%

Table 3-4: List of Pressure Transducers and Specifications

Transducer	Model	Range	Resolution	Sensitivity
Accelerometer	PCB-356A17	±10g peak	0.00006 g in RMS level	500 mV/g
Proximity Probe	Bently Nevada-3300XL NSv	10 – 70 mils		200 mV/mil

Table 3-5: List of Accelerometers and Proximity Probes

The vibration and shaft orbit were monitored during the performance test. Two tri-axial accelerometers and two proximity probes were installed on the pump. The two proximity probes are pointed towards the perimeter of the impeller in the perpendicular direction.

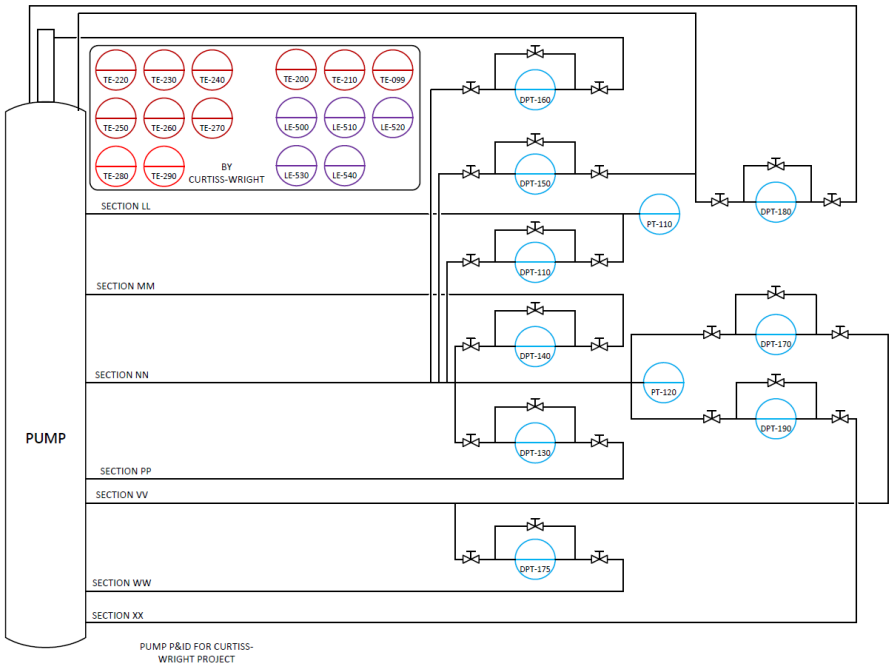

Figure 3-4: Differential Pressure Transducer Layout along Pump

All of the sensors and transducers were connected to A/D adapters manufactured by National Instruments Inc. The analog signal is converted to digital signal that can be recorded into the computer. The detail of the data acquisition system is shown in Figure 3-5. LabVIEW program was written to visualize and save the measured data during the test as shown in Figure 3-6 and Figure 3-7. The vibration and proximity probe data were monitored separately as they needs as high as 5 kHz sampling frequency. The other signals

including temperature, pressure and thrust forces were recorded by time averaging 60 seconds of data at 1 Hz sampling frequency.

The pump motor is controlled through a VFD (Variable Frequency Drive) during test. The VFD is pre-programmed to protect motor from over current limit, while changing the speed of motor smoothly during operation. Thus, pump performance monitoring and pump operation were completed remotely.

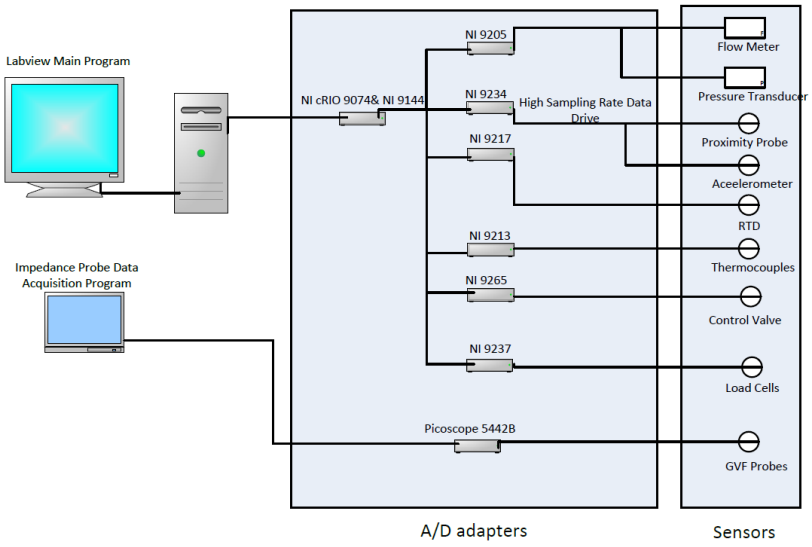

Figure 3-5: Data Acquisition System

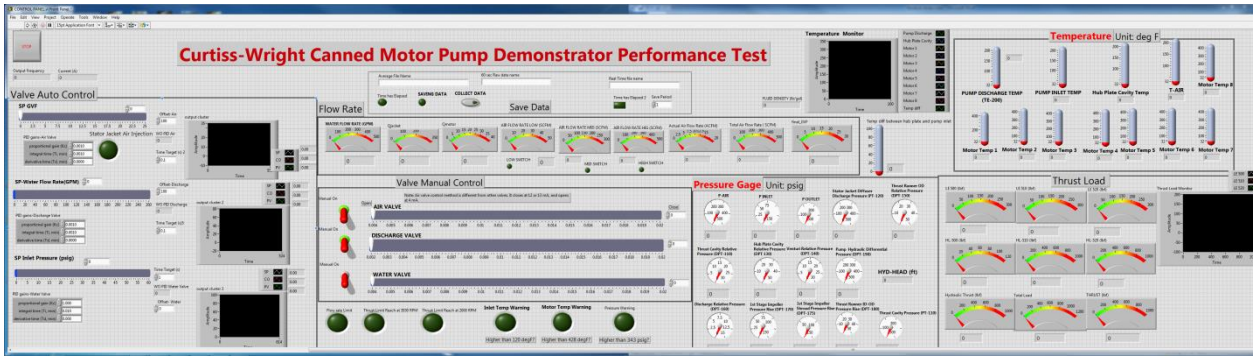

Figure 3-6: LabVIEW Program of Performance Test Panel

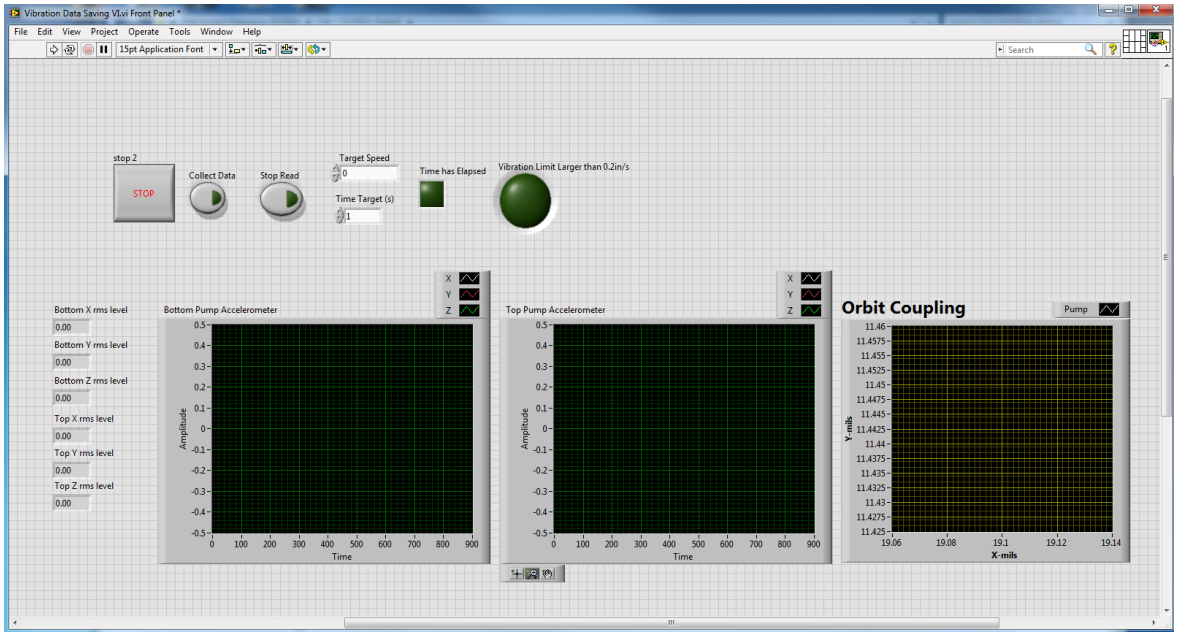

Figure 3-7: LabVIEW Program of Vibration Data Monitor Panel

3.1.4 Impedance Needle Probe

The impedance needle probe is designed and built at Turbo Lab TAMU. The sensor is comprised of three parts: Needle probe, Signal process and Data acquisition system. The needle probe part contains two separated electrodes inserted into alumina insulation layer.

The resistance and capacitance changes when the fluid mixture (water/air) passes between the electrodes. The variance of the resistance and capacitance then can reflect the local gas content where the sensor is positioned. The two separated electrodes can be regarded as one excitation pole and one measuring pole. The PicoScope USB Oscilloscope can generate a programmable AC voltage signal with arbitrary waveform. 12 sine voltage signals at different frequencies are superimposed together to form the input excitation signal into the PicoScope. The measuring pole is connected to an Op-amp circuit to sense the phase change of fluid. The voltage output from the Op-amp is measured by the PicoScope Oscilloscope with 125 MHz of sampling frequency. Figure 3-8 shows the exploded view of the impedance probe assembly and how it measures the multiphase flow. Figure 3-9 and Figure 3-10 show circuit diagram and integrated circuit box.

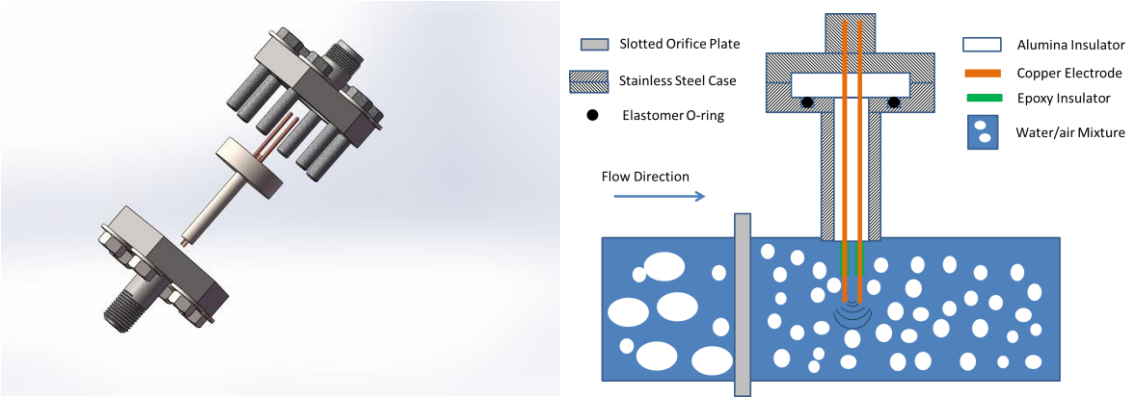

Figure 3-8: Impedance Probe Assembly

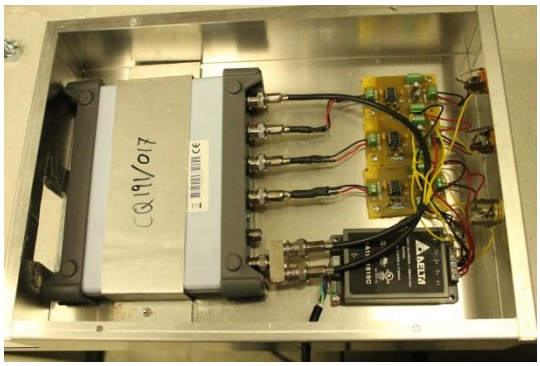

Figure 3-9: PicoScope Measuring Box

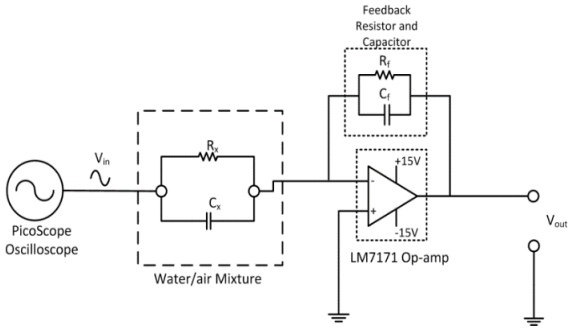

Figure 3-10: Op-amp Circuit

The probe is installed on a multiphase flow test rig for calibration, the P&ID of the test rig is shown in Figure 3-11. The calibration test can correlate measured electrical signal and known water flow rate and GVF. A slotted orifice plate is placed upstream of the impedance needle probe with a distance of 1.5 times of pipe diameter. The flow test conditions are listed shown in Figure 3-12. Compared with the flow regime map, the calibration test mainly covers bubbly flow.

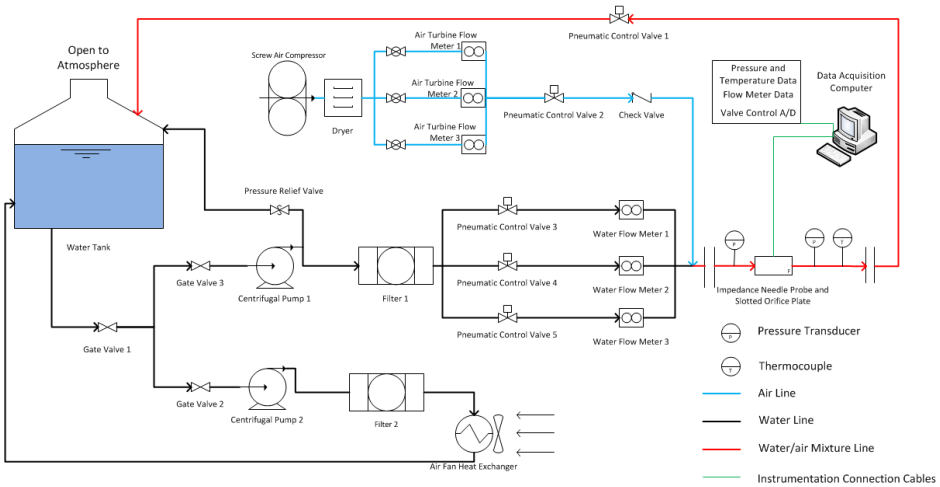

Figure 3-11: P&ID of Impedance Calibration Test

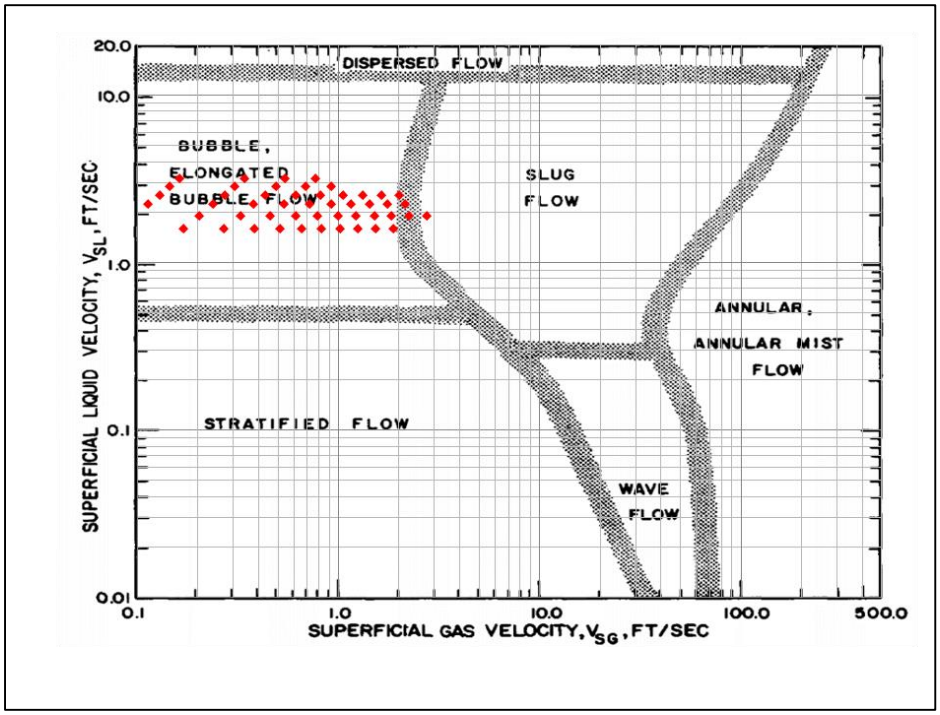

Figure 3-12: Flow Regime of Calibration Test Condition

The input signal's frequency and its corresponding magnitude are shown in Table 3-. Assuming the op-amp is ideal, the output voltage V_{out} is determined by:

$$\frac{V_{out}}{V_{in}} = -\frac{Z_f}{Z_x} \tag{3.5}$$

Where Z_f is the feedback circuit impedance determined by R_f and C_f, Z_x is the impedance of measured multiphase flow. With measured V_{out} and V_{in}, known Z_f, we can determine Z_x. Note that all the variables in the above formula are complex numbers.

Frequency (MHz)	Magnitude (V)
0.2	0.1675

Table 3-6: Excitation Signal Frequency and Magnitude

Frequency (MHz)	Magnitude (V)
0.6	0.1236
1	0.1432
1.28	0.1434
2.37	0.1080
3.46	0.0728
4.55	0.0581
5.64	0.0466
6.73	0.0306
7.82	0.0152
8.91	0.0150
10	0.0277

Table 3-6: Continued

From definition, the impedance of a material can be expressed by:

$$\boldsymbol{Z} = R + jX_c \tag{3.6}$$

Where R is the resistance of the material, Xc is called reactance. By definition,

$$X_c = -\frac{1}{2\pi f C} \tag{3.7}$$

Thus, Z is frequency dependent, measured in Ohms.

The inverse of impedance is called admittance, measured in Siemens.

$$\boldsymbol{Y} = \frac{1}{\boldsymbol{Z}} \tag{3.8}$$

By definition, Y can be expressed by:

$$\boldsymbol{Y} = G + jB \tag{3.9}$$

Where G is conductance, B is susceptance.

By substituting equation (5) into equation (2) and taking modulus, we have:

$$|Y_x| = \left|Y_f\right| \frac{|V_{out}|}{|V_{in}|} \tag{3.10}$$

To non-dimensionalize the admittance measured by this needle probe, Y^* is introduced by:

$$Y^* = \frac{|Y_x| - |Y_x|_{(GVF=100)}}{|Y_x|_{(GVF=0)} - |Y_x|_{(GVF=100)}} \tag{3.11}$$

For GVF=0, Y^*=1. Y_x is the admittance measured at any GVF.

For a signal or time series x(t), the power spectral density describes how the power or energy is distributed in frequency domain. It is defined by:

$$S_{xx}(f) = \lim_{T\to\infty} E[|\boldsymbol{X}(f)|^2] \tag{3.12}$$

Where **X**(f) is the Fourier transform of x(t), E denotes the estimated value. If there is another time series y(t), the CPSD (cross power spectral density) can be defined as:

$$S_{xy}(f) = \lim_{T\to\infty} E[\boldsymbol{X}(f)^* \cdot \boldsymbol{Y}(f)] \tag{3.13}$$

Where the $\mathbf{X}(f)^*$ is the conjugate of **X**(f), **Y**(f) is the Fourier transform of y(t).

The phase of CPSD between measured input signal and output signal is calculated through the whole frequency domain of sampling. It is found that the phase of CPSD ϕ has strong correlation with the GVF changing at some specific frequencies. For simplicity, we calculate the $\cos(\frac{\phi}{2})$ to non-dimensionalize it.

3.2 Numerical Methodology

Numerical simulations were studied on the transition part of the canned motor pump. The transition part is the place where annulus flow is divided into four flow paths. On each flow path, there is a slot flow passage connecting to thrust bearing cavity. This four flow paths merges together to the discharge pipe at the axial center of the pump. Since the symmetry of the flow characteristics, only one quarter of the annulus flow region is modeled. The simulated flow region is shown in Figure 3-13.

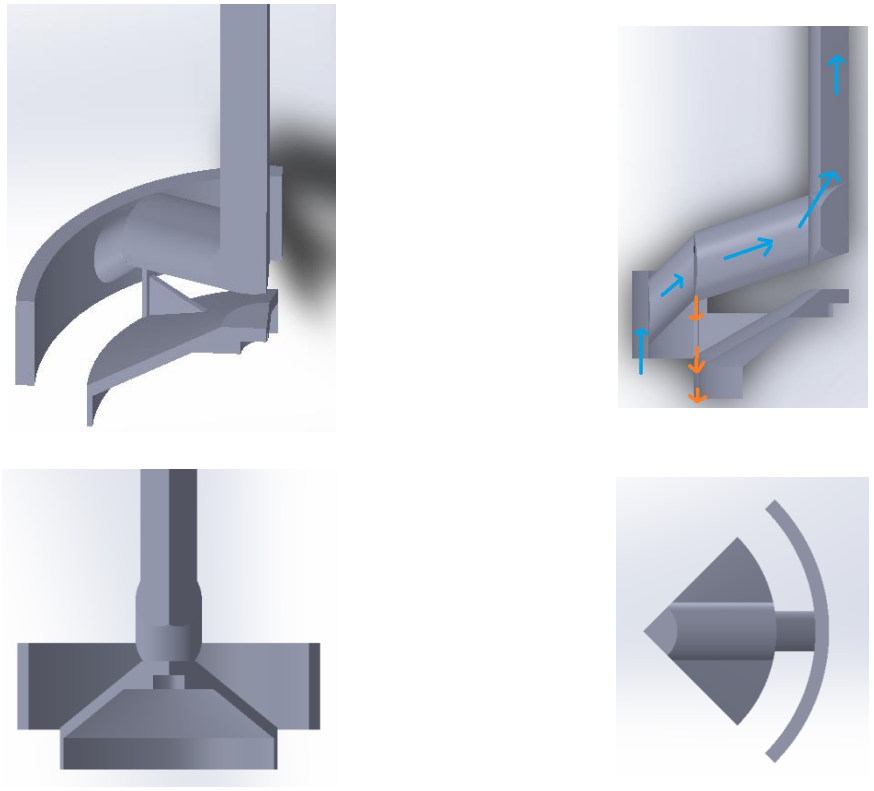

Figure 3-13: 3D Model of Flow Region

The flow region is meshed in ANSYS Meshing. To save meshing time, the flow region is meshed with Multi-zone method. With this method, the mesh has hexahedron elements in

the center, tetra and pyramids elements at the boundaries of different zones to connect each zone mesh. Such method saves both meshing time cost and later calculation time cost for this complex geometry.

From the mesh statistics data, the final meshes have 1142580 nodes and 1843154 elements. Mesh quality check in ANSYS Fluent is passed. Figure 3-14 shows the cross sectional and part view of the meshed region.

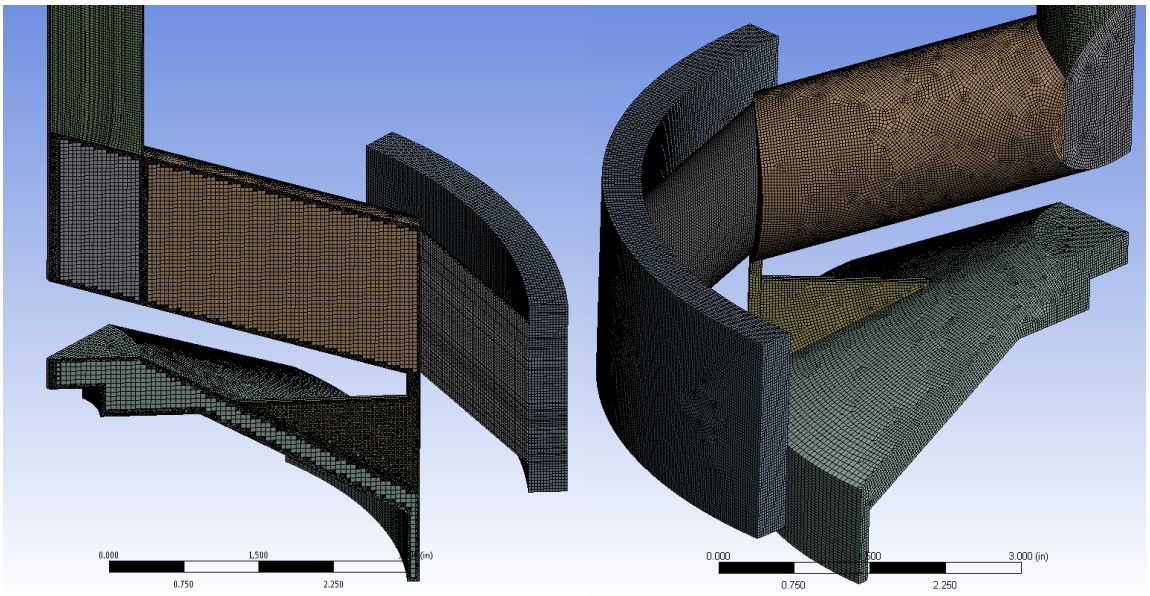

Figure 3-14: Meshed Flow Region

3.2.1 $k - \varepsilon$ model

In ANSYS Fluent, k – ε model was chosen to simulate the flow region inside the pump. The k – ε model is one type of eddy viscosity model that is based on Reynolds Averaged Navier-Stokes (RANS) equation. The RANS equations are based on Reynolds averaging theory that fluctuating velocity, pressure or density quantities can be expressed as:

$$u_i = \overline{u}_i + u_i' \tag{3.14}$$

Where $\overline{u}_i$ and u_i' are the mean and fluctuating velocity components. Substituting the expression into differential form of continuity and momentum equations, the RANS equations in Cartesian tensor form can be written as:

$$\frac{\partial \rho}{\partial t} + \frac{\partial}{\partial x_i}(\rho \overline{u_i}) = 0 \tag{3.15}$$

$$\begin{aligned} &\frac{\partial}{\partial t}(\rho \overline{u_i}) + \frac{\partial}{\partial x_j}\left(\rho \overline{u_i} * \overline{u_j}\right) \\ &\quad = -\frac{\partial \overline{p}}{\partial x_i} + \frac{\partial}{\partial x_j}\left[\mu\left(\frac{\partial \overline{u_i}}{\partial x_j} + \frac{\partial \overline{u_j}}{\partial x_i} - \frac{2}{3}\delta_{ij}\frac{\partial \overline{u_l}}{\partial x_l}\right)\right] + \frac{\partial}{\partial x_j}\left(-\rho \overline{u_i' u_j'}\right) \end{aligned} \tag{3.16}$$

In the above equation, one additional term from N-S equation is the gradient of $-\rho \overline{u_i' u_j'}$ which is called Reynolds stresses. Based on Boussinesq's assumption the Reynolds stresses are related to the mean velocity gradients:

$$-\rho \overline{u_i' u_j'} = \mu_t\left(\frac{\partial \overline{u_i}}{\partial x_j} + \frac{\partial \overline{u_j}}{\partial x_i}\right) - \frac{2}{3}(\rho k + \mu_t \frac{\partial \overline{u_l}}{\partial x_l})\delta_{ij} \tag{3.17}$$

μ_t is the turbulent viscosity, and k is the turbulent kinetic energy.

In standard $k-\varepsilon$ model, two additional transport equations are needed to model the turbulent viscosity. They are k equation for modeling turbulent kinetic energy:

$$\begin{aligned} &\frac{\partial}{\partial t}(\rho k) + \frac{\partial}{\partial x_i}(\rho k \overline{u_i}) \\ &\quad = \frac{\partial}{\partial x_j}\left[\left(\mu + \frac{\mu_t}{\sigma_k}\right)\frac{\partial k}{\partial x_j}\right] + G_k + G_b - \rho\varepsilon - Y_M + S_k \end{aligned} \tag{3.18}$$

and ε equation for modeling turbulent dissipation rate:

$$\frac{\partial}{\partial \mathrm{t}}(\rho\varepsilon) + \frac{\partial}{\partial \mathrm{x_i}}(\rho\varepsilon\overline{\mathrm{u_i}}) = \frac{\partial}{\partial \mathrm{x_j}}\left[\left(\mu + \frac{\mu_t}{\sigma_\varepsilon}\right)\frac{\partial \varepsilon}{\partial \mathrm{x_j}}\right] + C_{1\varepsilon}\frac{\varepsilon}{k}(G_k + C_{3\varepsilon}G_b) - C_{2\varepsilon}\rho\frac{\varepsilon^2}{k} + S_\varepsilon \quad (3.19)$$

G_k represents the generation of turbulence kinetic energy due to the mean velocity gradient.

$$G_k = -\rho\overline{\mathrm{u_i'u_j'}}\frac{\partial \overline{\mathrm{u_j}}}{\partial \mathrm{x_i}} \quad (3.20)$$

$$G_k = \mu_t S^2 \quad (3.21)$$

Where S is the modulus of the mean rate of strain tensor,

$$S = \sqrt{2S_{ij}S_{ij}} \quad (3.22)$$

G_b is the generation of turbulent kinetic energy due to buoyancy.

$$G_b = \beta g_i \frac{\mu_t}{Pr_t}\frac{\partial T}{\partial x_i} \quad (3.23)$$

Pr_t is the turbulent Prandtl number for energy and g_i is the component of the gravitational vector in the i the direction. For the standard and realizable k- ε model, Pr_t equals 0.85. β is the coefficient of thermal expansion:

$$\beta = -\frac{1}{\rho}\left(\frac{\partial \rho}{\partial T}\right)_P \quad (3.24)$$

Y_M represents the contribution of the fluctuating dilatation in compressible turbulence to the overall dissipation rate.

$$Y_M = 2\rho\varepsilon M_t^2 \tag{3.25}$$

Where M_t is the turbulent Mach number.

$$M_t = \sqrt{\frac{k}{c^2}} \tag{3.26}$$

c is the speed of sound.

The turbulent viscosity or eddy viscosity, μ_t, is modeled by the following:

$$\mu_t = \rho C_\mu \frac{k^2}{\varepsilon} \tag{3.27}$$

The model constants are given as:

$C_{1\varepsilon} = 1.44$, $C_{2\varepsilon} = 1.92$, $C_\mu = 0.09$, $\sigma_k = 1.0$, $\sigma_\varepsilon = 1.3$

The standard k − ε model has advantages of low computational cost and wide application in most industry flow problems. However, due to its assumption of isotropic turbulent viscosity, it is not well suited for flow with streamline curvature or rotations. Thus, RNG k − ε model and realizable k − ε model are developed to improve its performance. The major differences of this two model from the standard one lie on the method of computing turbulent viscosity from k and ε, the turbulent Prandtl numbers and the generation and destruction terms in the ε equation.

The realizable k − ε model is utilized in Fluent with changing the standard model in the following: Variable C_μ is used to better model the turbulent viscosity, and new model for ε equation is based on the dynamic equation of the mean square vorticity fluctuation.

The transport equations for k and ε in the realizable $\mathrm{k}-\varepsilon$ model are:

$$\frac{\partial}{\partial \mathrm{t}}(\rho \mathrm{k})+\frac{\partial}{\partial \mathrm{x_j}}\left(\rho k \overline{\mathrm{u_j}}\right) = \frac{\partial}{\partial \mathrm{x_j}}\left[\left(\mu+\frac{\mu_t}{\sigma_k}\right)\frac{\partial \mathrm{k}}{\partial \mathrm{x_j}}\right]+G_k+G_b-\rho\varepsilon-Y_M+S_k \tag{3.28}$$

And

$$\frac{\partial}{\partial \mathrm{t}}(\rho \varepsilon)+\frac{\partial}{\partial \mathrm{x_j}}\left(\rho \varepsilon \overline{\mathrm{u_j}}\right) = \frac{\partial}{\partial \mathrm{x_j}}\left[\left(\mu+\frac{\mu_t}{\sigma_\varepsilon}\right)\frac{\partial \varepsilon}{\partial \mathrm{x_j}}\right]+\rho C_1 S_\varepsilon-\rho C_2\frac{\varepsilon^2}{k+\sqrt{\nu\varepsilon}}+C_{1\varepsilon}\frac{\varepsilon}{k}C_{3\varepsilon}G_b+S_\varepsilon \tag{3.29}$$

Where $C_1=\max[0.43,\frac{\eta}{\eta+5}]$, $\eta=\mathrm{S}\frac{k}{\varepsilon}$, $\mathrm{S}=\sqrt{2S_{ij}S_{ij}}$.

In realizable $\mathrm{k}-\varepsilon$ model, C_μ is not constant.

$$C_\mu=\frac{1}{A_0+A_s\frac{kU^*}{\varepsilon}} \tag{3.30}$$

Where $U^*\equiv\sqrt{S_{ij}S_{ij}+\tilde{\Omega}_{ij}\tilde{\Omega}_{ij}}$, and $\tilde{\Omega}_{ij}=\Omega_{ij}-2\varepsilon_{ijk}\omega_k,\ \Omega_{ij}=\bar{\Omega}_{ij}-\varepsilon_{ijk}\omega_k$.

$\bar{\Omega}_{ij}$ is the mean rate of rotation tensor viewed in a moving reference frame with the angular velocity ω_k. The model constants are $A_0=4.04, A_s=\sqrt{6}cos\phi$, where

$\phi=\frac{1}{3}cos^{-1}(\sqrt{6}W)$, $W=\frac{S_{ij}S_{jk}S_{ki}}{\tilde{S}^3}$, $\tilde{S}=\sqrt{S_{ij}S_{ij}}$, $S_{ij}=\frac{1}{2}(\frac{\partial u_j}{\partial x_i}+\frac{\partial u_i}{\partial x_j})$

Model constants are

$C_{1\varepsilon} = 1.44$, $C_2 = 1.9$, $\sigma_k = 1.0$, $\sigma_\varepsilon = 1.2$.

The $k-\varepsilon$ model is only suitable for solving fully turbulent flow. Near the wall region, the turbulent viscosity is negligible and molecular viscosity becomes dominant. Thus, $k-\varepsilon$ model will not be able to solve the near wall viscous layer. Two approaches are usually used to solve this problem: wall function method or low Reynold number approach. In Fluent, wall function method is applicable for both $k-\varepsilon$ model and Reynolds Stress Model. The wall function method is to utilize empirical relations to calculate turbulence dissipation rate mathematically rather than from the transport equation.

The law-of-the-wall for mean velocity is

$$U^* = \frac{1}{\kappa}\ln(Ey^*) \tag{3.31}$$

$$U^* \equiv \frac{U_P C_\mu^{1/4} k_P^{1/2}}{\tau_w/\rho} \tag{3.32}$$

U^* is the dimensionless velocity.

$$y^* \equiv \frac{\rho C_\mu^{1/4} k_P^{1/2} y_P}{\mu} \tag{3.33}$$

y^* is the dimensionless distance from the wall.

$\kappa = 0.4187$, $E = 9.793$. U_P is mean velocity of the fluid at the wall-adjacent cell centroid P. k_P is turbulence kinetic energy at the wall-adjacent cell centroid P. y_P is distance from the centroid of wall-adjacent cell P to the wall.

When $y^* > 11.225$, the log-law is employed. When $y^* < 11.225$, $U^* = y^*$.

3.2.2 Multiphase Model

In ANSYS Fluent, the Euler-Euler approach is able to simulate two-phase flow when the volume of the discrete phase cannot be negligible. The Euler-Euler approach treat each phase as interpenetrating continua, and the total volume fraction of all phases is equal to one. In this study, Eulerian model is chosen to simulate the water-air mixture considering water/air slip velocity.

Volume fraction equation is used to describe the volume occupied by each phase. V_q, the volume of phase q, is

$$V_q = \int_V \alpha_q dV \tag{3.34}$$

Where α_q is the volume fraction of phase q.

The effective density of phase q is

$$\hat{\rho}_q = \alpha_q \rho_q \tag{3.35}$$

Where ρ_q is the physical density of phase q.

The continuity equation for phase q is

$$\frac{\partial}{\partial t}(\alpha_q \rho_q) + \nabla \cdot (\alpha_q \rho_q \vec{v}_q) = \sum_{p=1}^{n} (\dot{m}_{pq} - \dot{m}_{qp}) + S_q \tag{3.36}$$

Where $\vec{v}_q$ is the velocity of phase q and $\dot{m}_{pq}$ represents the mass transfer from p^{th} to q^{th} phase.

The momentum equation for phase q is:

$$\begin{aligned}\frac{\partial}{\partial t}\left(\alpha_q \rho_q \vec{v}_q\right) + \nabla \cdot \left(\alpha_q \rho_q \vec{v}_q \vec{v}_q\right) \\ = -\alpha_q \nabla \mathrm{p} + \nabla \cdot \bar{\bar{\tau}}_q + \alpha_q \rho_q \vec{g} \\ + \sum_{p=1}^{n} \left(\vec{R}_{pq} + \dot{m}_{pq} \vec{v}_{pq} - \dot{m}_{qp} \vec{v}_{qp}\right) + (\vec{F}_q + \vec{F}_{lift,q} \\ + \vec{F}_{wl,q} + \vec{F}_{vm,q} + \vec{F}_{td,q})\end{aligned} \tag{3.37}$$

Where $\bar{\bar{\tau}}_q$ is the q^{th} phase stress-strain tensor, $\vec{F}_q$ is an external body force, $\vec{F}_{lift,q}$ is a lift force, $\vec{F}_{wl,q}$ is a wall lubrication force, $\vec{F}_{vm,q}$ is a virtual mass force, and $\vec{F}_{td,q}$ is a turbulent dispersion force. $\vec{R}_{pq}$ is an interaction force between phases, and p is the pressure shared by all phases. $\dot{m}_{pq} \vec{v}_{pq}$ and $\dot{m}_{qp} \vec{v}_{qp}$ is the momentum transfer term between phase p and phase q due to mass transfer.

The energy equation for phase q is:

$$\begin{aligned}\frac{\partial}{\partial t}\left(\alpha_q \rho_q h_q\right) + \nabla \cdot \left(\alpha_q \rho_q \vec{v}_q h_q\right) \\ = \alpha_q \frac{\partial p_q}{\partial t} + \bar{\bar{\tau}}_q : \nabla \vec{v}_q - \nabla \cdot \vec{q}_q + S_q \\ + \sum_{p=1}^{n} (Q_{pq} + \dot{m}_{pq} h_{pq} - \dot{m}_{qp} h_{qp})\end{aligned} \tag{3.38}$$

where h_q is the specific enthalpy of the q^{th} phase, $\vec{q}_q$ is the heat flux, S_q is a source term, Q_{pq} is the intensity of heat exchange between p^{th} and q^{th} phase, and h_{qp} is the enthalpy between phase exchange (such as evaporation or condensation).

4. RESULTS AND DISCUSSION

4.1 Experimental Results of Multiphase Canned Motor Pump

4.1.1 Venturi Calibration Test

The Venturi calibration test purpose is to calibrate the stator jacket flow rate vs Venturi pressure drop. According to the test procedure discussed in 3.1.2 Test Procedure, the relationship between stator jacket mixture flow rate, Venturi differential pressure, and pump inlet flow rate are obtained. After that, based on measured performance data, the stator jacket mixture flow rate is interactively calculated, as well as the motor internal cooling flow rate.

The discharge coefficient of the Venturi feature is calculated from the Venturi calibration test. The equation was previously listed in Equation 3.3. The average C_d is 0.9844 with a standard deviation 0.0058. The C_d result is shown in Figure 4-1 with error bar of 95% confidence.

An iteration algorithm for calculating the stator jacket mixture is shown in Figure 4-2. First, input the test measured stator jacket air flow rate, pump inlet water flow rate, pump stator jacket pressure data to the program, then with a guessed stator jacket mass flow rate, the quality x and $\rho_{mixture}$ in stator jacket can be calculated. With $\rho_{mixture}$ and Venturi difference pressure data, a new stator jacket mixture mass flow rate is calculated through Equation 3.3. Then this new mass flow rate is looped back to the start of the program to

update. The iteration ends once the stator jacket mass flow rate difference in two loops is less than ε=2.2204e-16. The program algorithm flow chart is shown in Figure 4-2.

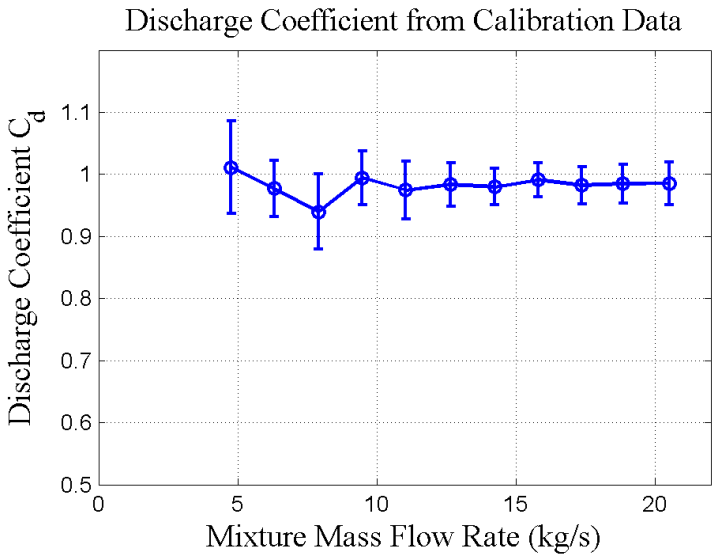

Figure 4-1: Discharge Coefficient of Venturi

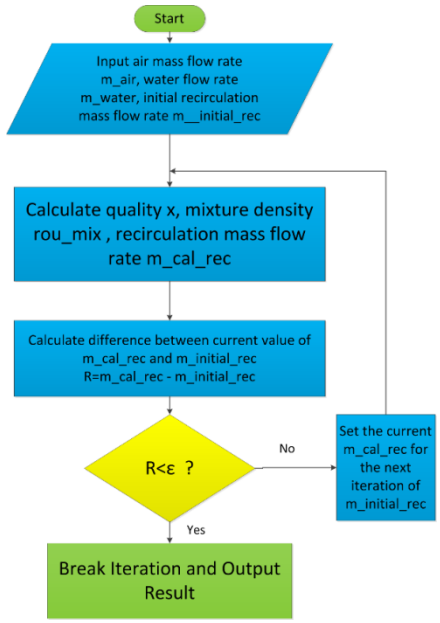

Figure 4-2: Iteration Algorithm Flow Chart

After the iteration, the stator jacket mixture mass flow rate, mixture density, internal cooling mixture mass flow rate and pump discharge pipe mixture mass flow rate are obtained. The stator jacket GVF can also be obtained by:

$$GVF_{stator\ jacket} = \frac{\rho_{water} - \rho_{mixture}}{\rho_{water} - \rho_{air}} \times 100\% \quad 4.1$$

With known stator jacket pressure and temperature, ρ_{air} in stator jacket is known. Thus, the water volume flow rate in stator jacket and air volume flow rate in stator jacket is calculated by:

$$Q_{w,st} = (1 - GVF) * Q_{mix,st} \quad 4.2$$

$$Q_{a,st} = GVF * Q_{mix,st} \quad 4.3$$

A non-dimensional parameter m^* is defined by:

$$m^* = \frac{m_{internal\ cooling}}{m_{stator\ jacket}} \quad 4.4$$

With $m_{internal\ cooling}$ is the internal cooling mixture mass flow rate, $m_{stator\ jacket}$ is the stator jacket mixture mass flow rate. The m^* vs GVF at different pump operation conditions are shown in the following figures.

From Figure 4-3 through Figure 4-5, the stator jacket water flow rate is shown for all the multiphase flow test conditions. The difference between this two flow rates is the internal cooling water flow rate. Here the water volume flow rate is calculated based on Equation 4.1. It can be seen that stator jacket volume flow rate increases with the pump inlet water flow rate. In Figure 4-3, when inlet water flow rate is 75 GPM and 100 GPM, the stator

jacket volume flow rate is varying about 20 GPM. This is due to the error of calculating Venturi discharge coefficient and Venturi pressure drop measurement at low flow rate and low stator jacket pressure. In Figure 4-5, when inlet water flow rate is near 200 GPM, the variance of stator jacket water flow rate reduces to 10 GPM. This variance is caused by GVF variance and Venturi pressure drop measurement error.

Figure 4-6 to Figure 4-8 show the GVF effect on flow distribution between stator jacket and internal cooling path. As for 3930 RPM cases, all the m^* is below 0.1. While for 2000 RPM and 3000 RPM case, m^* can reach as high as 0.3 when pump inlet volume flow rate is 75 GPM. As the Venturi pressure drop has larger errors for low pressure and low flow rate cases, the m^* for the 75 GPM case may overestimate the actual flow distribution. With the increase of GVF in stator jacket, m^* will decrease. This trend is also consistent with CFD results. Detailed CFD results will be presented in Section 4.2.

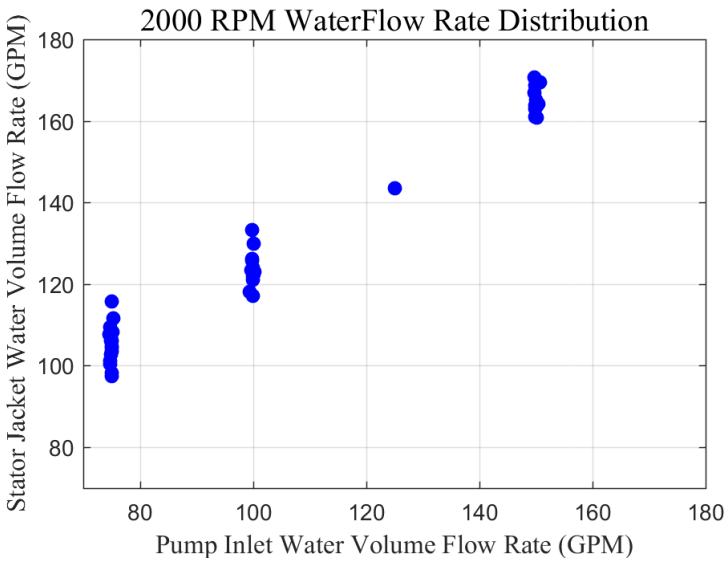

Figure 4-3: 2000 RPM Water Flow Rate Distribution

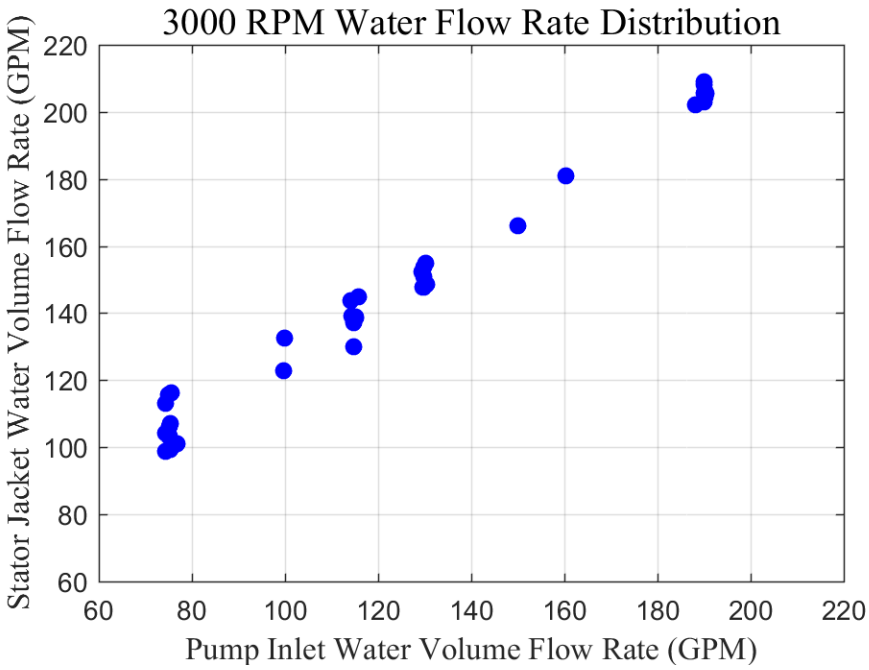

Figure 4-4: 3000 RPM Water Flow Rate Distribution

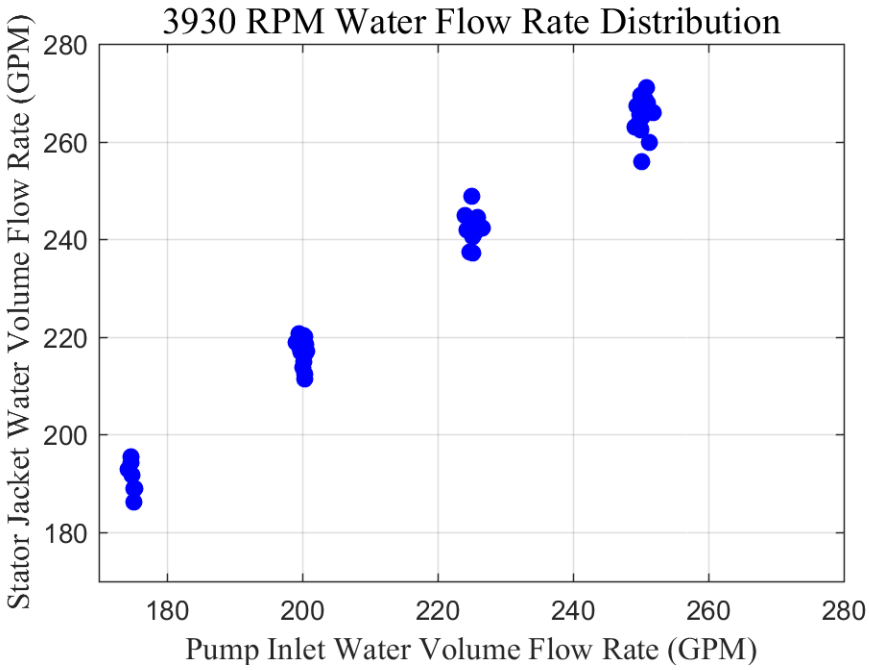

Figure 4-5: 3930 RPM Water Flow Rate Distribution

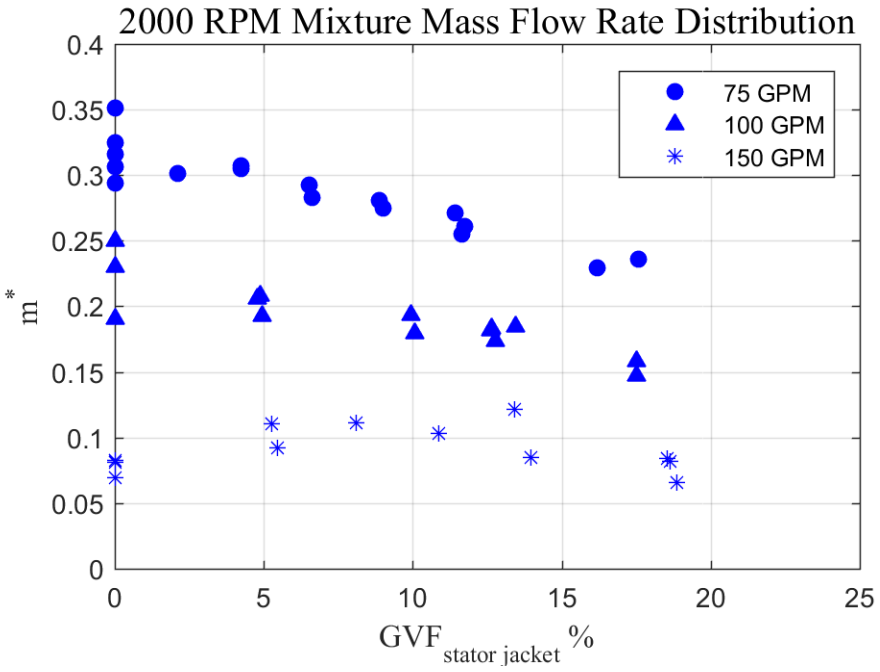

Figure 4-6: 2000 RPM Mass Flow Rate Ratio

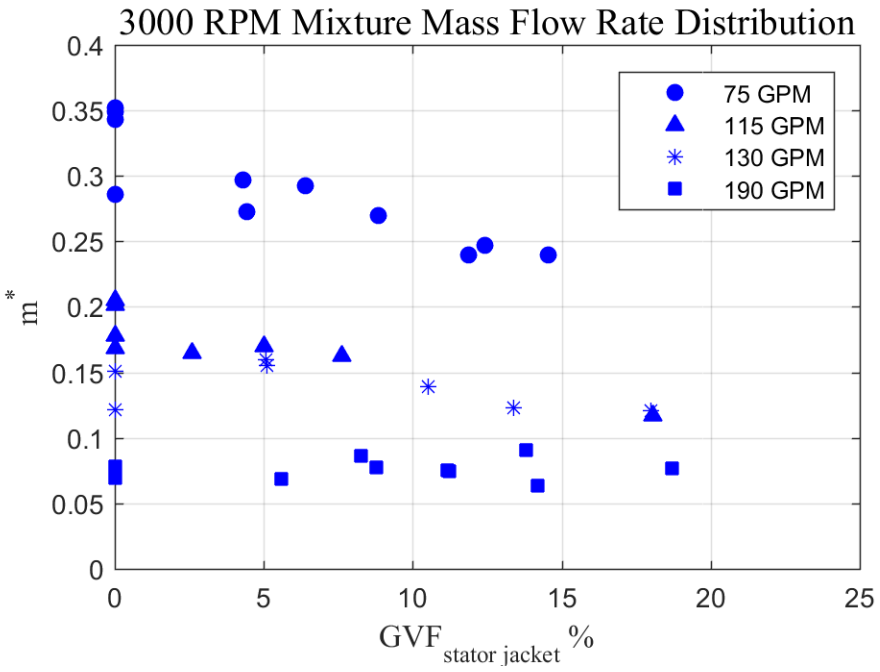

Figure 4-7: 3000 RPM Mass Flow Rate Ratio

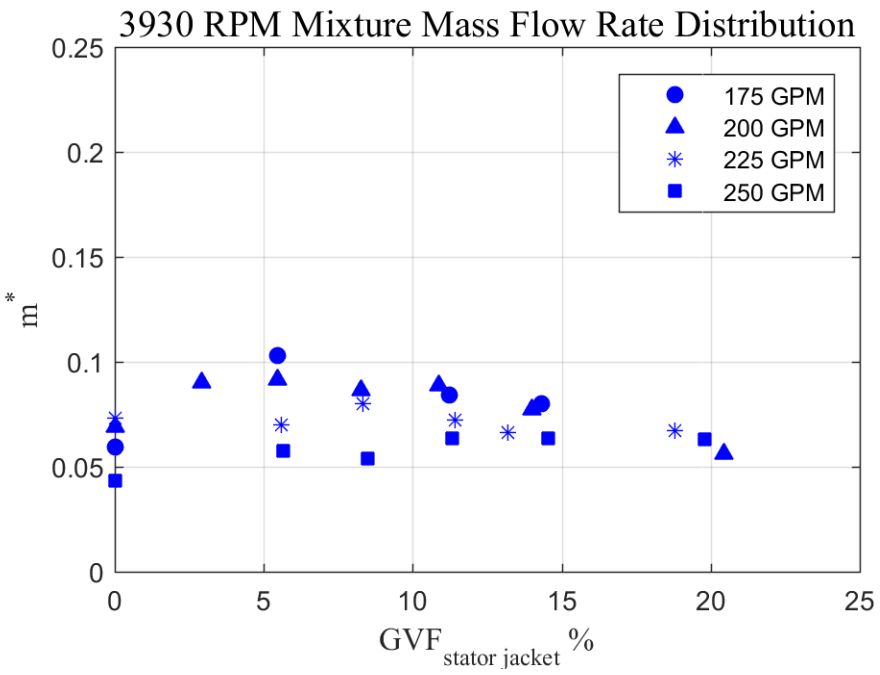

Figure 4-8: 3930 RPM Mass Flow Rate Ratio

4.1.2 Thrust Load Cell Calibration Test

There are five thrust load cells installed inside the thrust bearing housing to measure the axial load force during the test. The static pressure caused force needs to be subtracted to obtain the actual hydraulic thrust force. Thus, the thrust load cells are calibrated under static pressure changing.

$$Thrust\ Load = F_{load\ cell} - F_{pressure} \tag{4.5}$$

$F_{load\ cell}$ is the force reading from the load cell on thrust bearing, $F_{pressure}$ is the force caused by the static pressure of the fluid in thrust bearing cavity. When the pump is not running and the thrust cavity pressure is 0 psig, $F_{load\ cell}$ represents the rotor wet weight. $F_{pressure}$ vs thrust cavity pressure is obtained by a static pressure calibration test. During

the test, both the thrust bearing on top and impellers at the bottom are immersed into liquid. The upstream and downstream valves of the pump are closed to form a pressurized space. No flow exists in the system. A hand piston pump is connected to one port on the stator jacket. With this hand pump, static pressure in the whole system can be adjusted manually and kept at a target value. Neglecting the static pressure due to height difference, the load cell on the thrust bearing will feel the static pressure change in the thrust bearing cavity. During the test, all the pressure and load cell data are recorded and averaged digitally. The calibration curve is shown in Figure 4-9. A linear regression curve shown here is used for calculating the actual hydraulic thrust load in the future tests. Note that when p=0 psig, measured thrust load is the rotor wet weight, which is 87 lbf here.

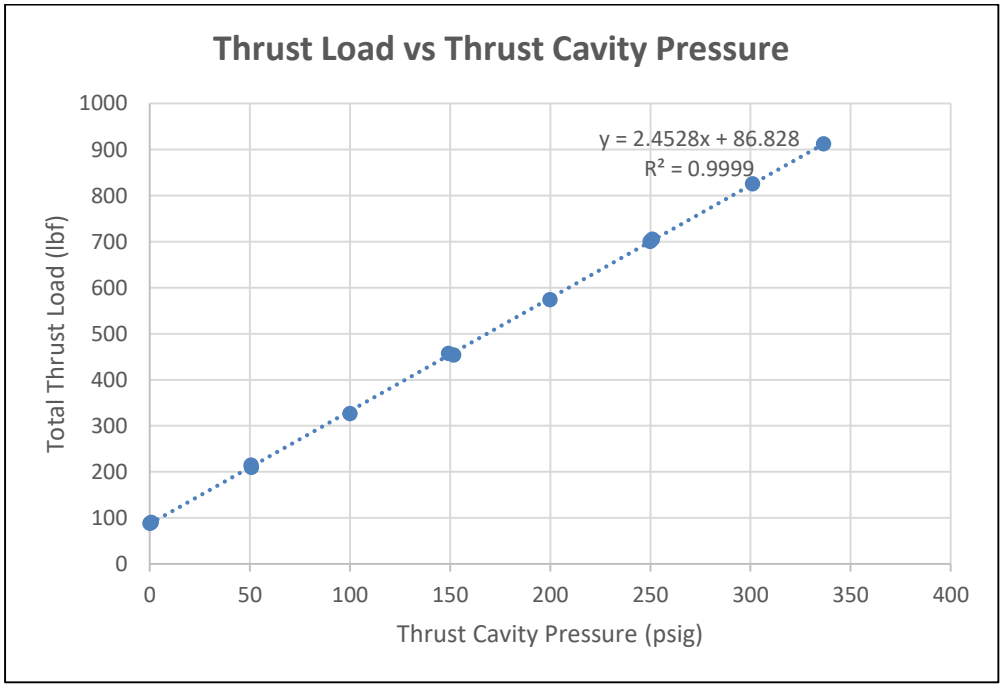

Figure 4-9: Thrust Load vs Thrust Bearing Cavity Pressure

4.1.3 Multiphase Performance Test

Figure 4-10 to Figure 4-12 show the performance curve of this canned motor pump under multiphase flow conditions. Since the air is injected behind the pump impeller and diffuser, the hydraulic head is not affected by increasing GVF at stator jacket. The pump's rotation speed is adjusted by a VFD. Three speeds are tested at 2000 RPM, 3000 RPM and 3930 RPM. 2000 RPM is the minimum rotation speed or working condition for this pump. 3930 RPM is the standard design operation speed. From the performance curve, the pump's working range is found at: 2000 - 3930 RPM, 50 - 270 GPM, 140 - 600 head of feet. The standard error bars represents the 95% confidence interval of the measurement.

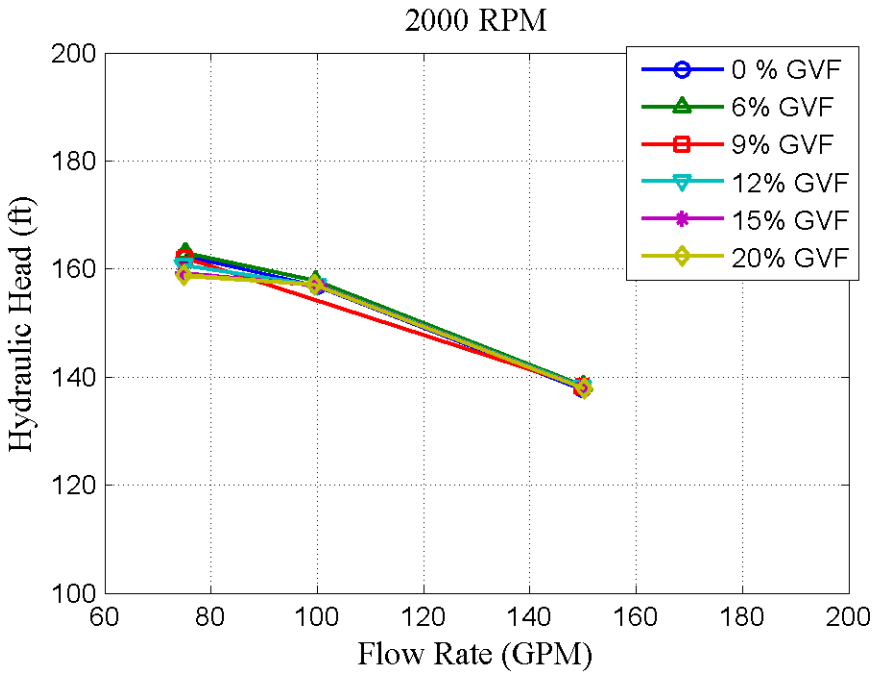

Figure 4-10: Hydraulic Head @2000 RPM

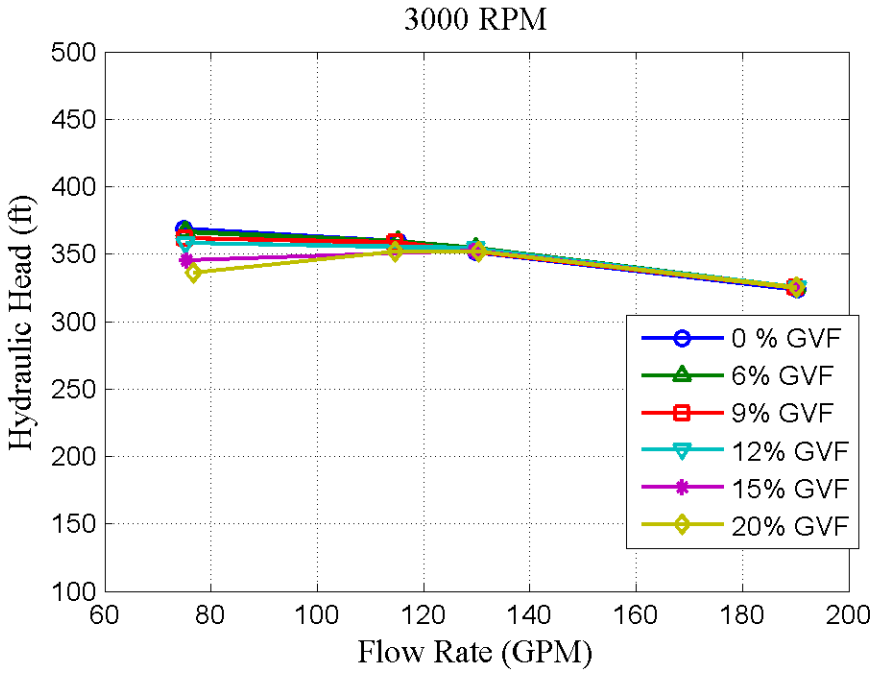

Figure 4-11: Hydraulic Head @3000 RPM

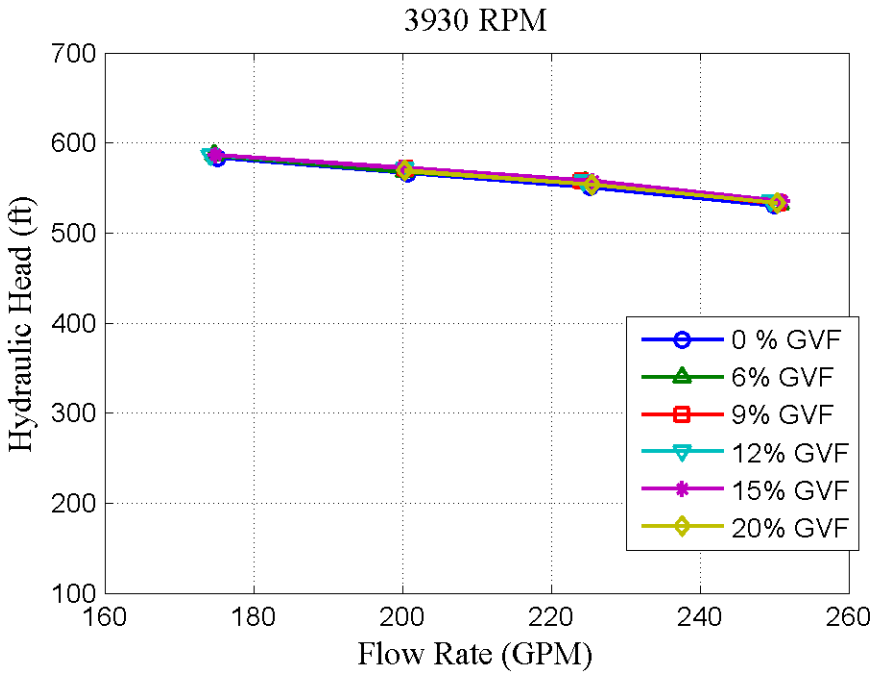

Figure 4-12: Hydraulic Head @3930 RPM

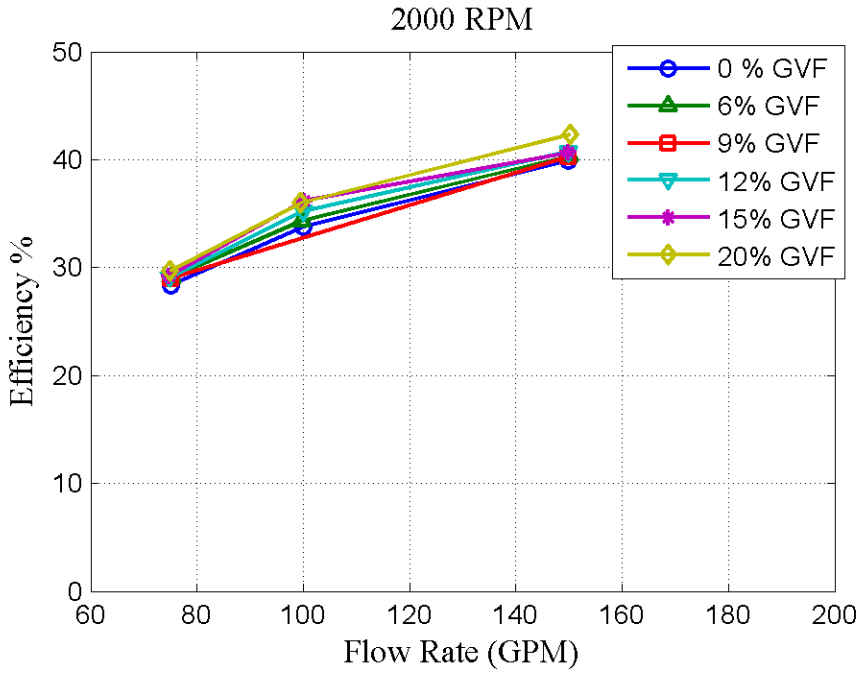

Figure 4-13: Pump Efficiency @ 2000 RPM

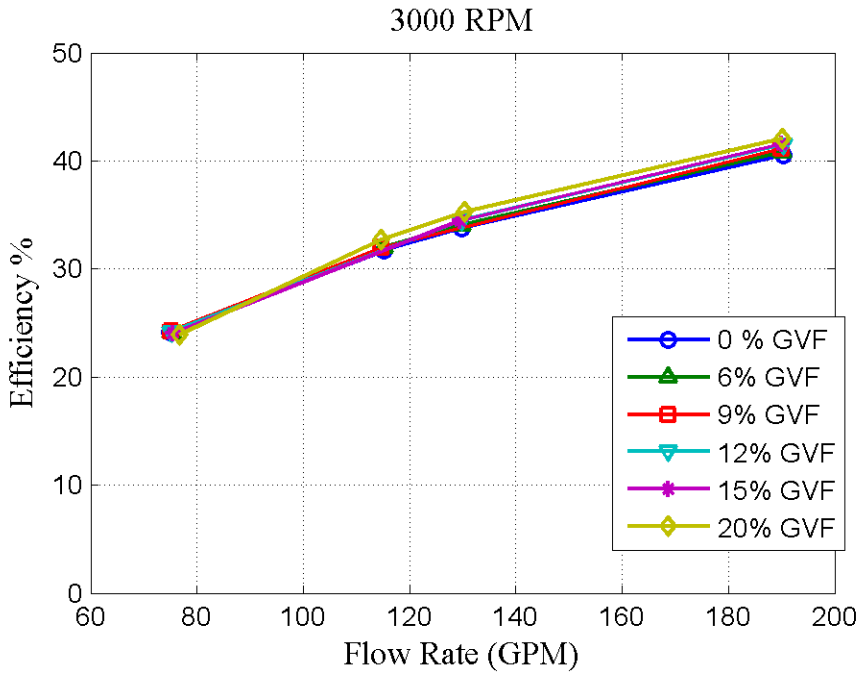

Figure 4-14: Pump Efficiency @ 3000 RPM

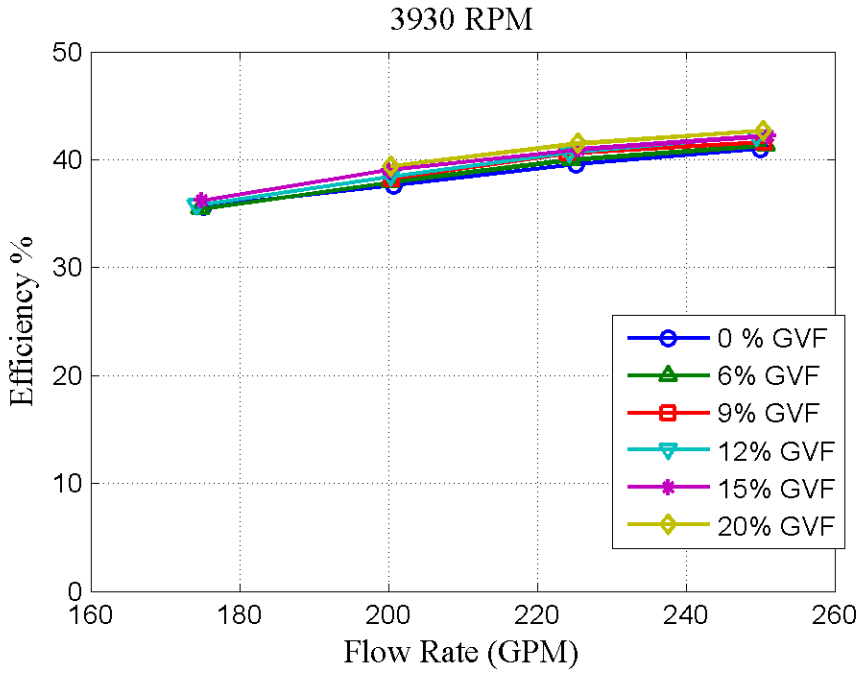

Figure 4-15: Pump Efficiency @ 3930 RPM

Pump efficiency η is defined as:

$$\eta = \frac{\Delta p * Q}{P_{motor}} \tag{4.6}$$

Where Δp is the pressure difference between pump stator jacket and pump inlet, Q is the pump inlet water flow rate measured by inlet water flow meter, P_{motor} is the power consumed by the motor, measured from VFD. In Figure 4-13 to Figure 4-15, the pump efficiency vs inlet flow rate are shown for different rotation speed. For the same pump efficiency, the pump inlet flow rate increases as the pump rotation speed increases from 2000 RPM to 3930 RPM. The GVF in stator jacket doesn't significantly affect the pump efficiency, though minor differences exists between different GVF conditions.

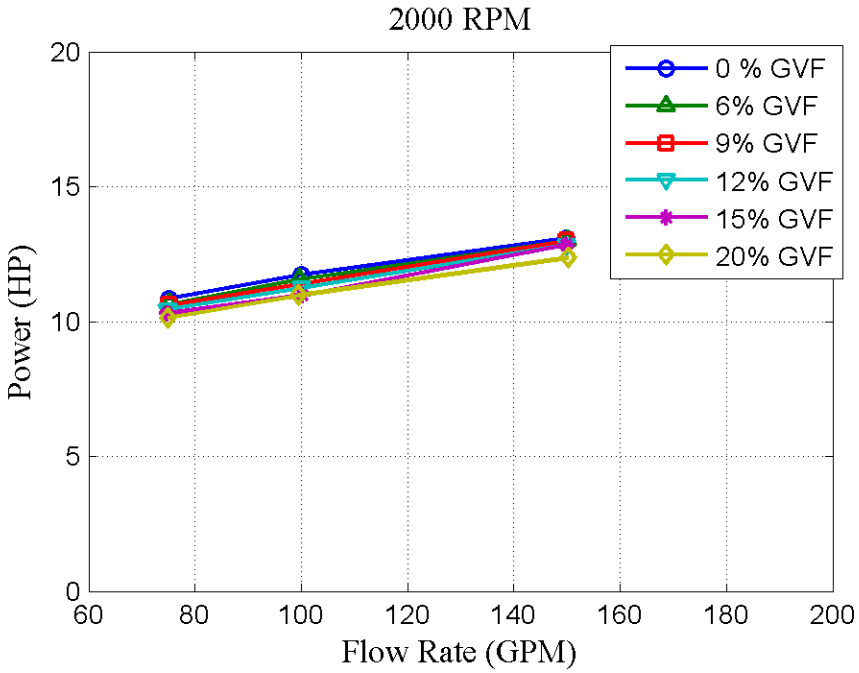

Figure 4-16: Motor Power @ 2000 RPM

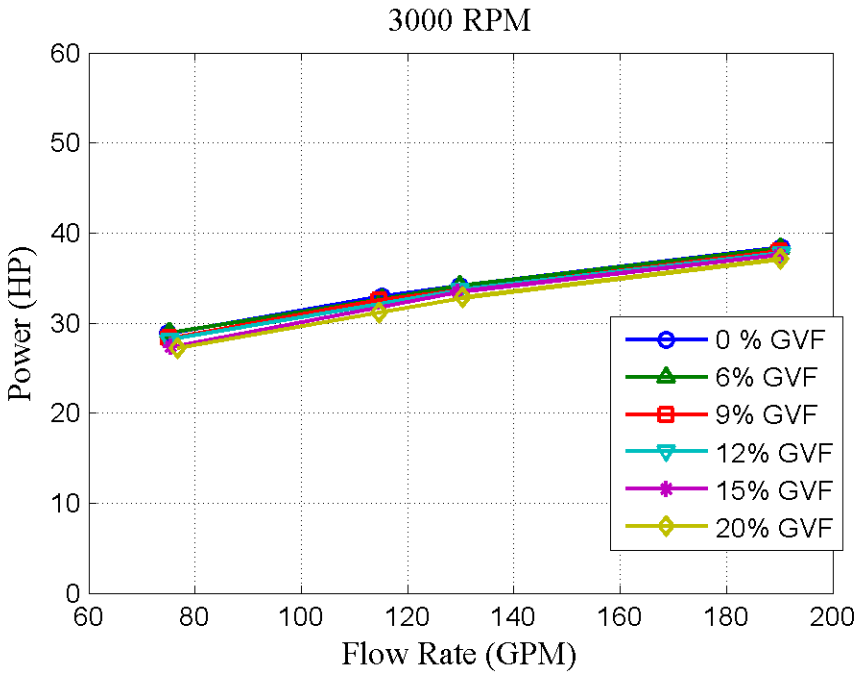

Figure 4-17: Motor Power @ 3000 RPM

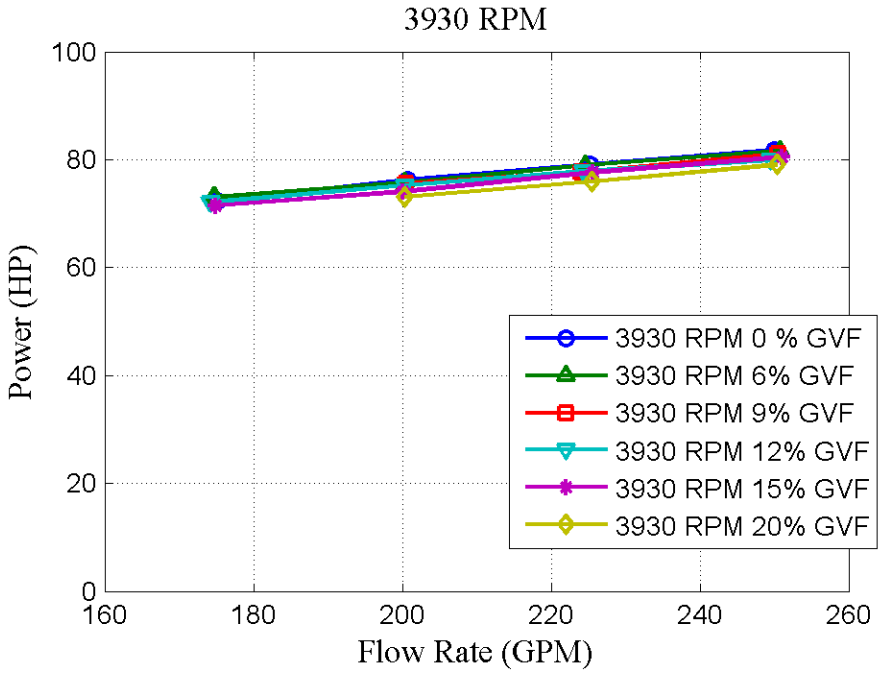

Figure 4-18: Motor Power @ 3930 RPM

The power consumed by the canned motor pump is shown in Figure 4-16 to Figure 4-18. As the rotation speed and inlet flow rate increases, the pump consumes more power to deliver more fluid through system. With GVF increasing from 0% to 20%, the canned motor pump consumes less power for all speed cases. This trend is also consistent with motor current vs GVF in Figure 4-22 to Figure 4-24.

4.1.4 Multiphase Flow Effect on Canned Motor Pump Performance

The multiphase flow effect on the canned motor pump performance is shown in this section. The GVF in the stator jacket will affect the pump's power consumption, pressure distribution and flow rate in the thrust bearing cavity. By analyzing these data, the reason for these effect can be predicted with knowledge of fluid mechanics.

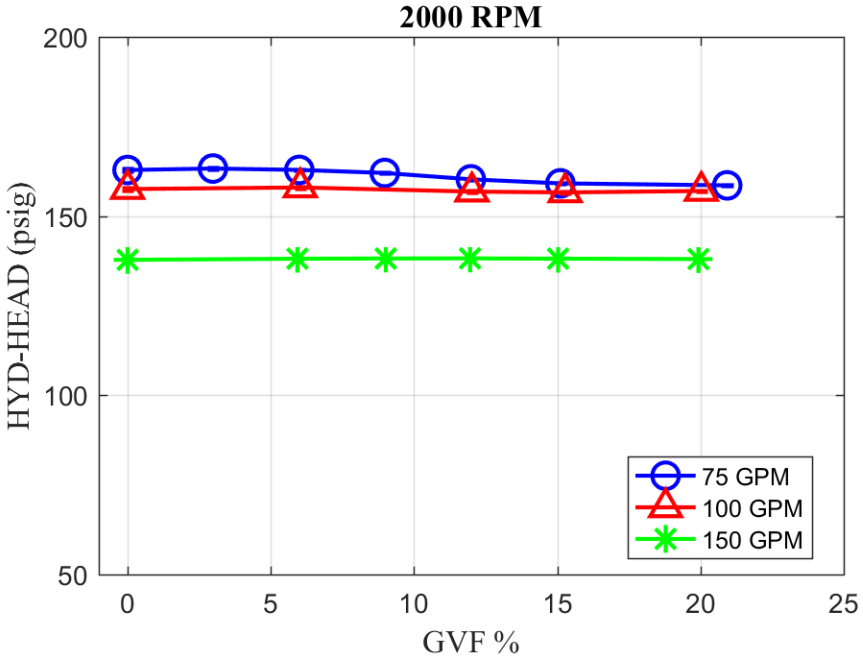

Figure 4-19: GVF vs Hydraulic Head @ 2000 RPM

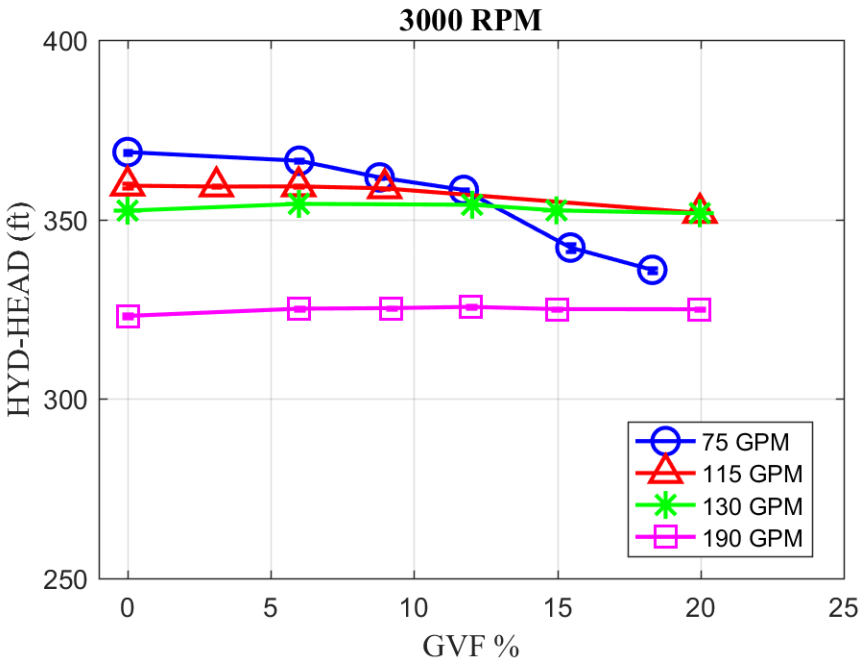

Figure 4-20: GVF vs Hydraulic Head @ 3000 RPM

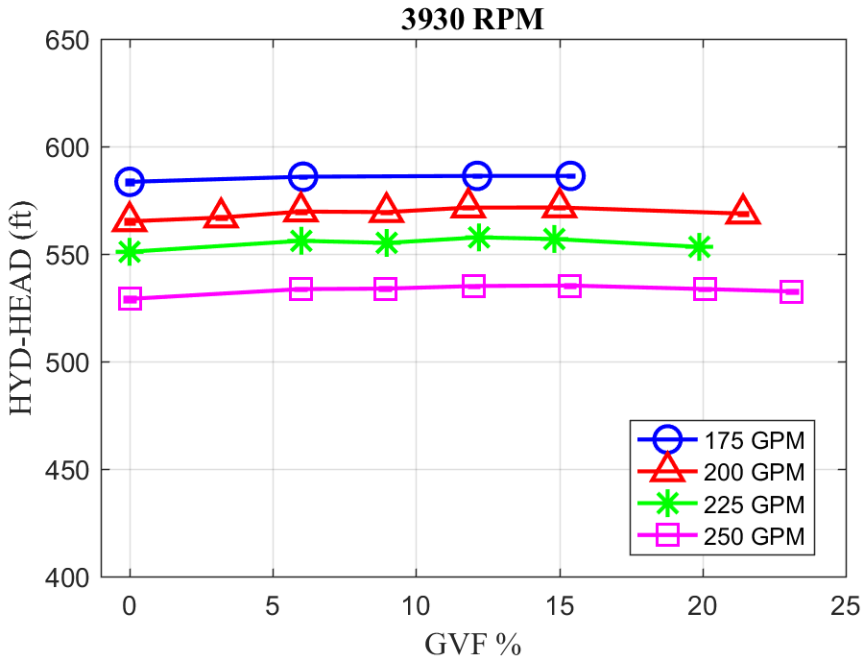

Figure 4-21: GVF vs Hydraulic Head @ 3930 RPM

Hydraulic head of the pump is not affected by stator jacket GVF in all flow range except for 3000 RPM 75 GPM from Figure 4-20. Since, air is not injected into the pump inlet, no cavitation or gas lock should be expected. Thus, the pressure difference between pump inlet and stator jacket is not changing with stator jacket GVF. This also indicates that there should be very little content of air flowing through pump internal cooling flow path.

From the Figure 4-22 to Figure 4-24, the VFD current shows a decreasing trend with increasing of the stator jacket GVF at 3930 RPM. This indicates that with more injection of air at the stator jacket, the pump consumes less power. However, when rotation speed reduces to 2000 RPM, this current decrease trend is not obvious. This implies the gas decreases the drag on the rotor.

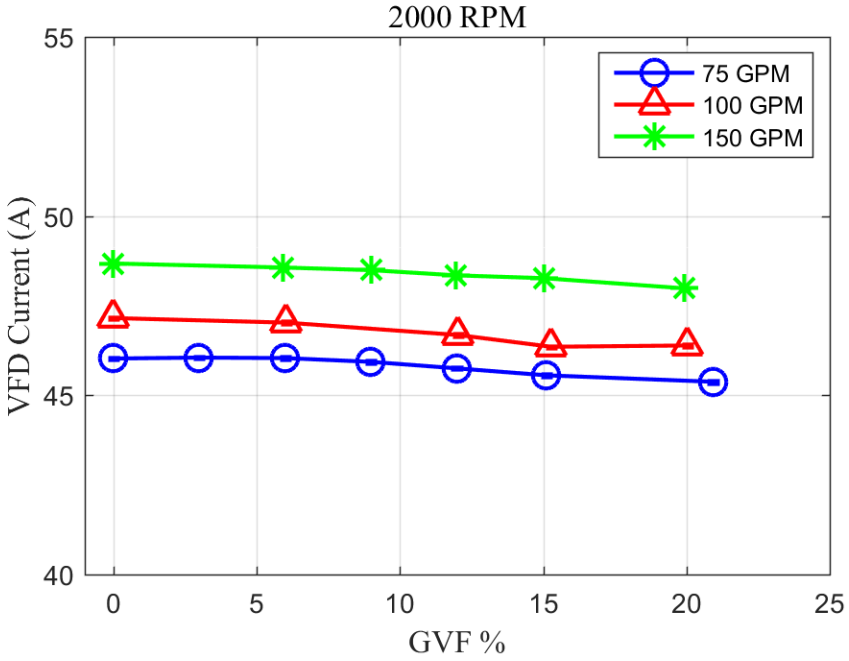

Figure 4-22: GVF vs VFD Current @ 2000 RPM

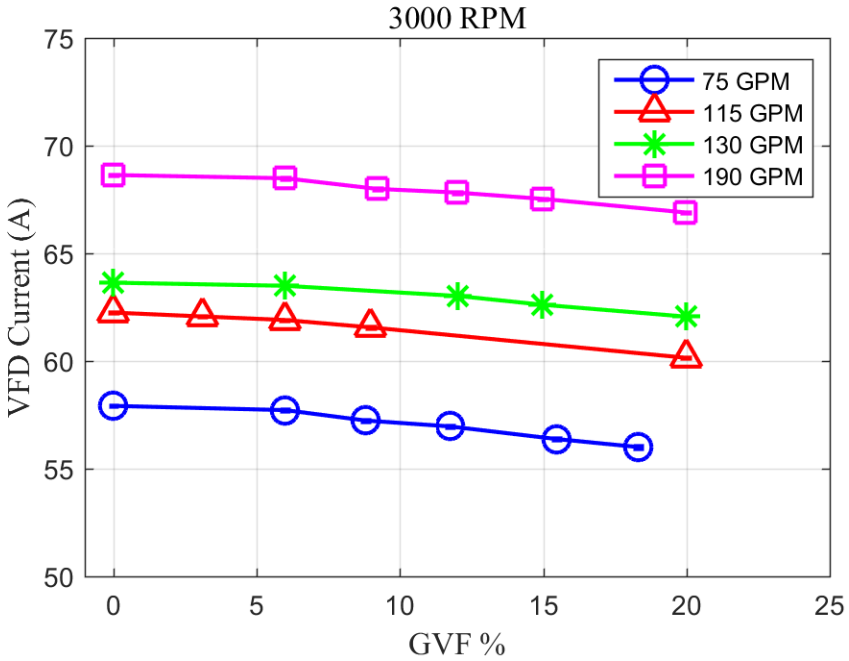

Figure 4-23: GVF vs VFD Current @ 3000 RPM

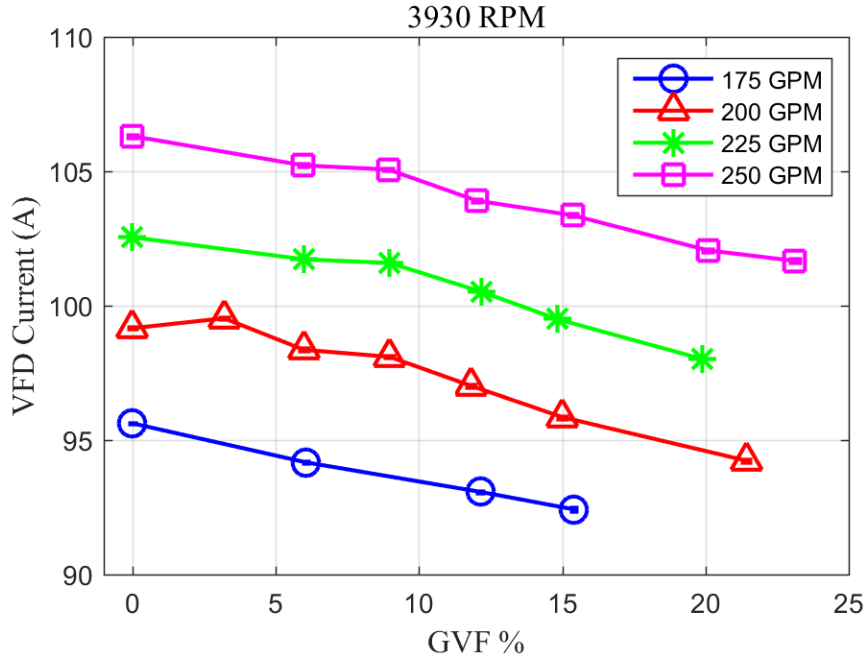

Figure 4-24: GVF vs VFD Current @ 3930 RPM

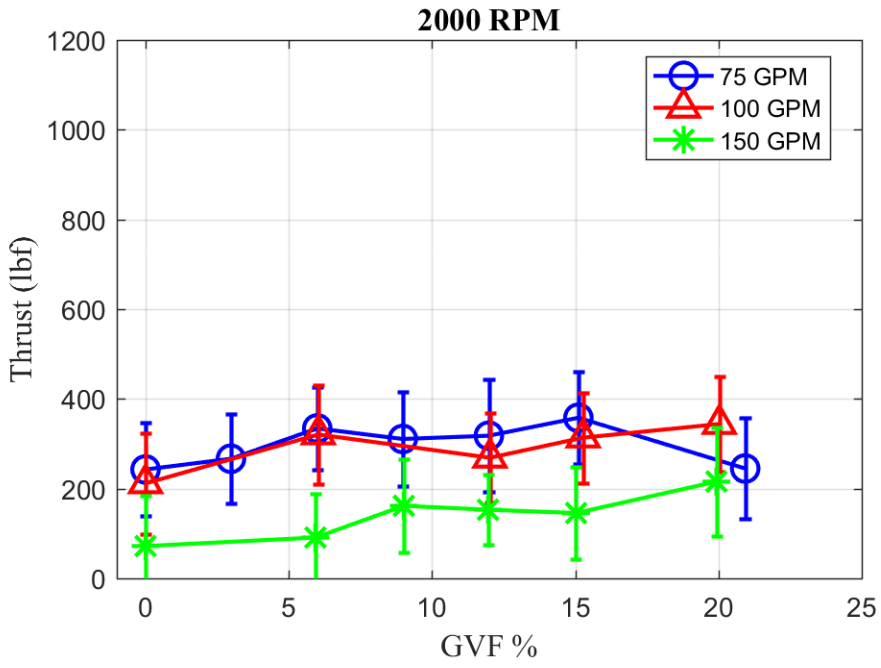

Figure 4-25: GVF vs Thrust @ 2000 RPM

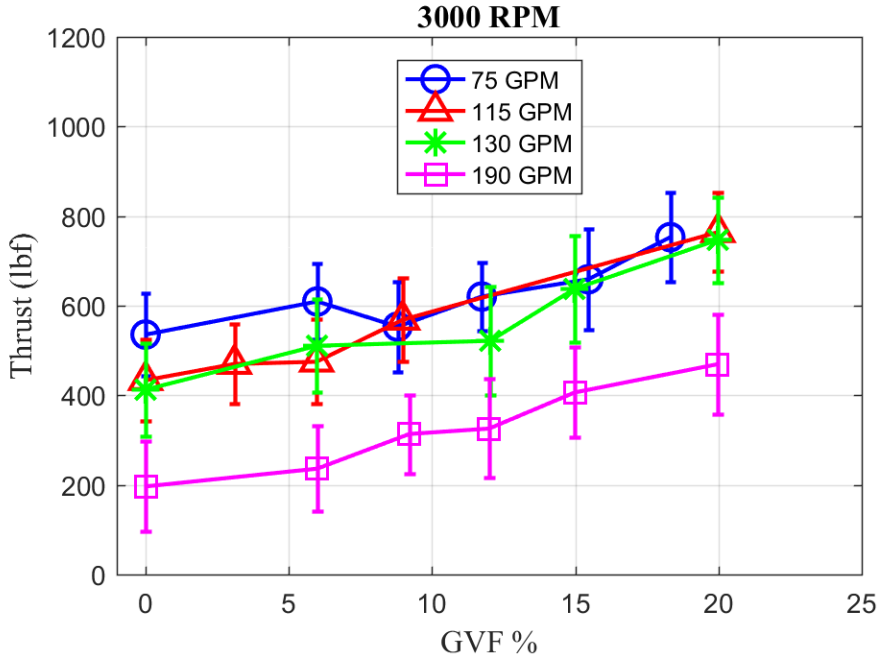

Figure 4-26: GVF vs Thrust @ 3000 RPM

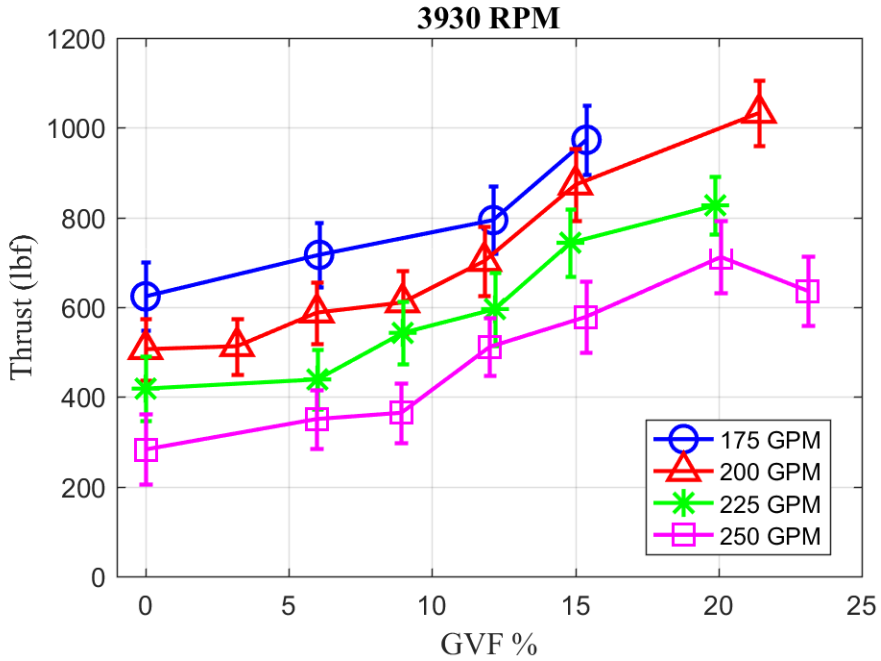

Figure 4-27: GVF vs Thrust @ 3930 RPM

From Figure 4-25 to Figure 4-27, it is shown that the thrust forces on the thrust bearing of this canned motor pump increases with GVF. This is beneficial for the stable operation of the canned motor, because more thrust force means the pump thrust bearing are forming a more stable liquid film to hold the pump shaft rotor. With more GVF injected into the stator jacket, pump can run stable at higher flow rate at that specific rotation speed. For example, for the 3930 RPM case, the maximum flow rate of the pump is 275 GPM. At this flow rate, the pump is running at a critical condition, and the thrust force value can goes below 100 lbf sometimes. This is very dangerous for the pump operation. Uplift of the shaft rotor could happen at any time. However, with the injection of air, the thrust forces increase to 200 lbf.

The pump's axial thrust load is the resultant force due to pressure difference of the pump impeller front shroud and rear shroud. From the stator jacket pressure data and hydraulic head data, the force at the front shroud side doesn't change with GVF. For this canned motor pump, there are also 4 expeller vanes on the rear shroud of two impellers. The expeller vane will reduce shaft seal pressure and reduce the axial thrust. If the total axial thrust increases, it indicates the flow rate passing through the expeller vane decreases. Thus, the GVF causing thrust increase means less internal cooling flow passing the second impeller expeller vane back to stator jacket.

The pressure distribution inside the canned motor pump is monitored and recorded during the test. By analyzing pressures at different positions along pump internal flow passage, the internal multiphase flow condition can be predicted.

The thrust bearing cavity relative pressure is the pressure difference between the thrust bearing cavity and the stator jacket. The thrust bearing cavity relative pressure increases as the flow rate increases for all speed condition from Figure 4-28 to Figure 4-30. This is very easy to understand. Since the flow diverts into two directions from the stator jacket, and there is a flow restriction from the stator jacket to the thrust bearing cavity. The pressure drop will increase with more flow rate. Also, with the increase of GVF, the thrust cavity relative pressure decreases. It is predicted that with more gas injected into stator jacket, there will be less fluid passing through the motor internal cooling passage, causing less pressure drop between the thrust cavity and stator jacket. With GVF increasing from 0% to 20%, bubbly flow dominates. The air bubbles will decrease the fluid viscosity, which means it is easier to flow from the stator jacket to the discharge.

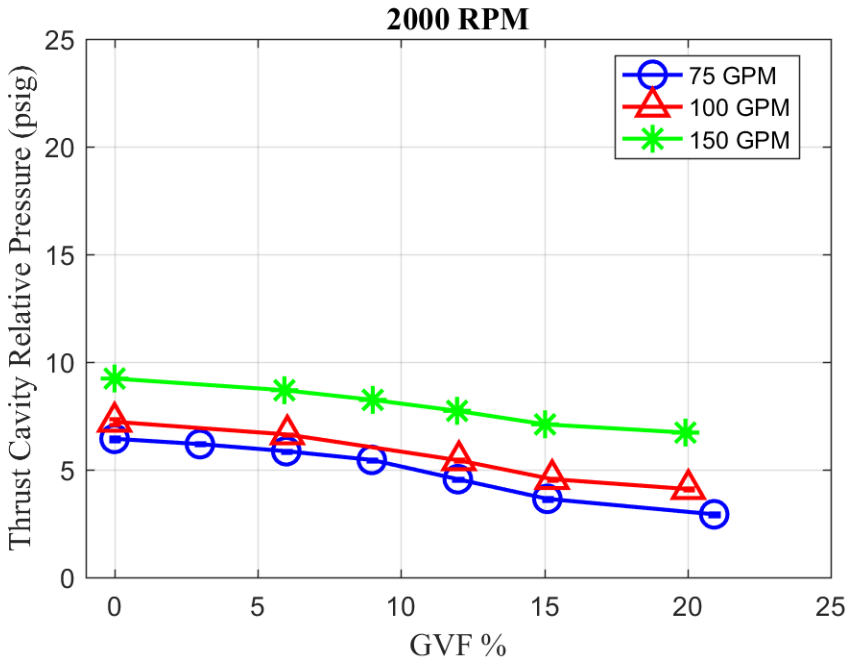

Figure 4-28: GVF vs Thrust Cavity Relative Pressure @ 2000 RPM

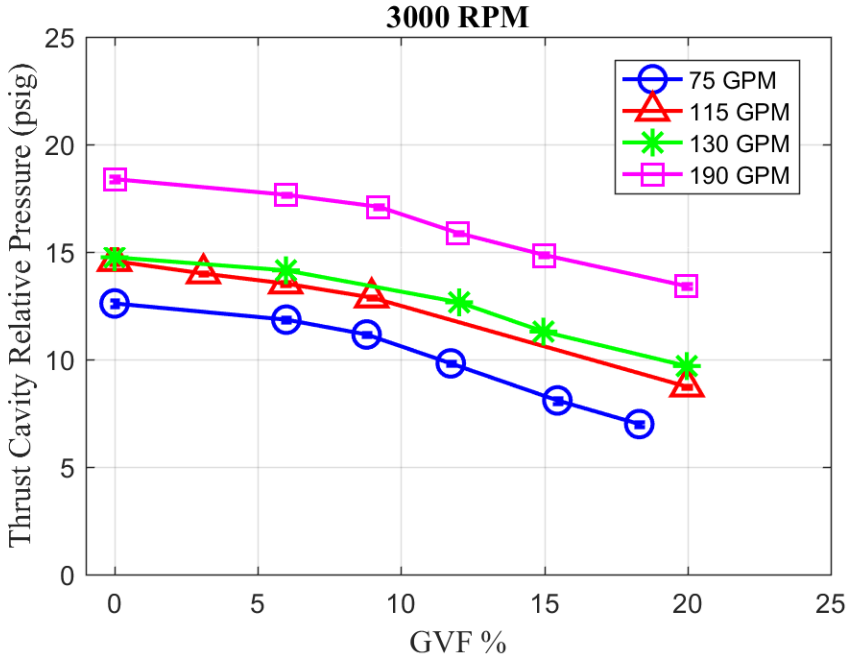

Figure 4-29: GVF vs Thrust Cavity Relative Pressure @ 3000 RPM

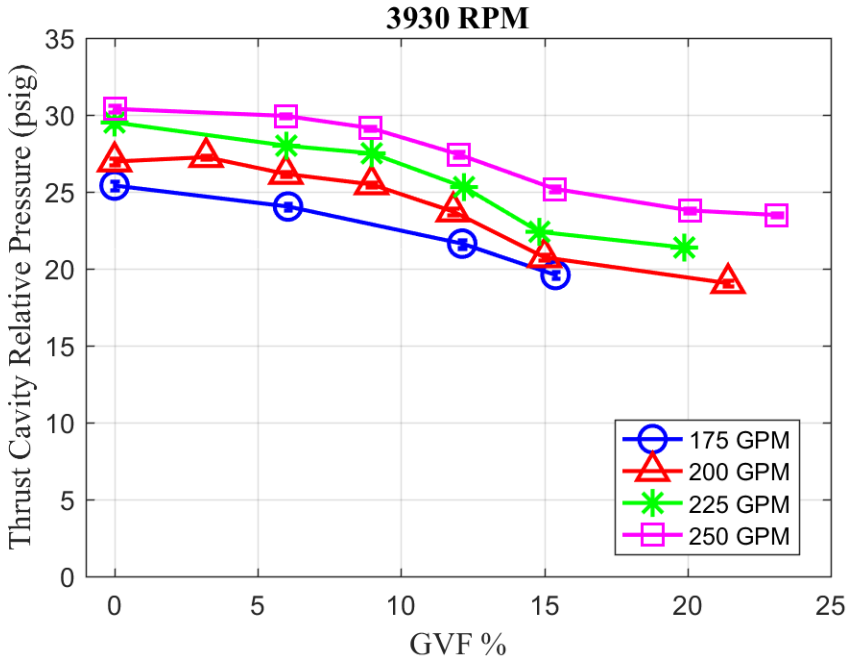

Figure 4-30: GVF vs Thrust Cavity Relative Pressure @ 3930 RPM

The hub plate cavity is on the same route of the pump internal flow passage. Thus, the hub plate cavity relative pressure has the same trend as the thrust bearing cavity as seen from Figure 4-31 to Figure 4-33. However, the absolute value of hub plate cavity pressure is less than the thrust cavity pressure, since the flow has to overcome the flow restriction in the thrust bearing, journal bearings and shaft can annulus area. With the pressure value of the thrust cavity, stator jacket, pump outlet and hub plate cavity, the whole internal flow loop can be analyzed for different flow conditions.

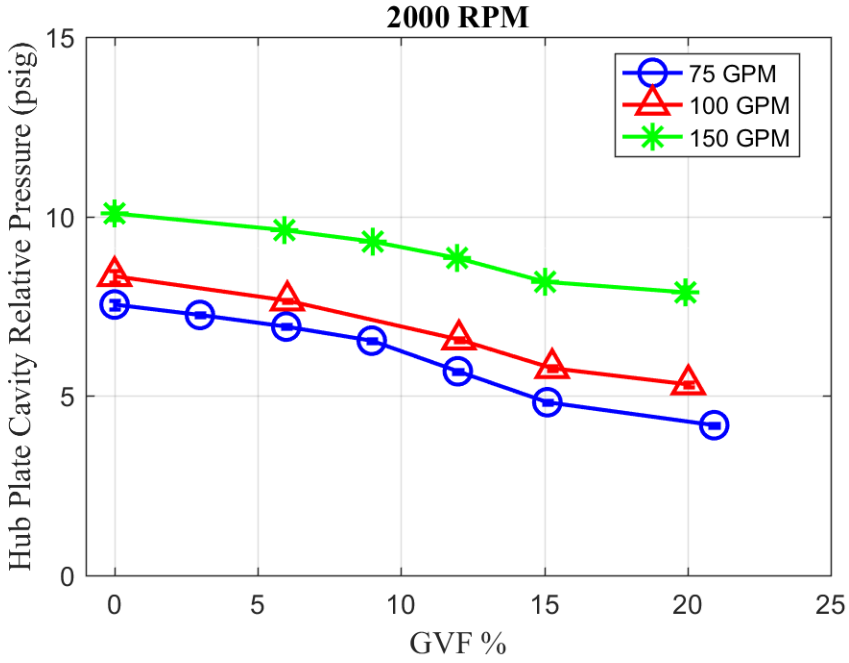

Figure 4-31: GVF vs Hub Plate Cavity Relative Pressure @ 2000 RPM

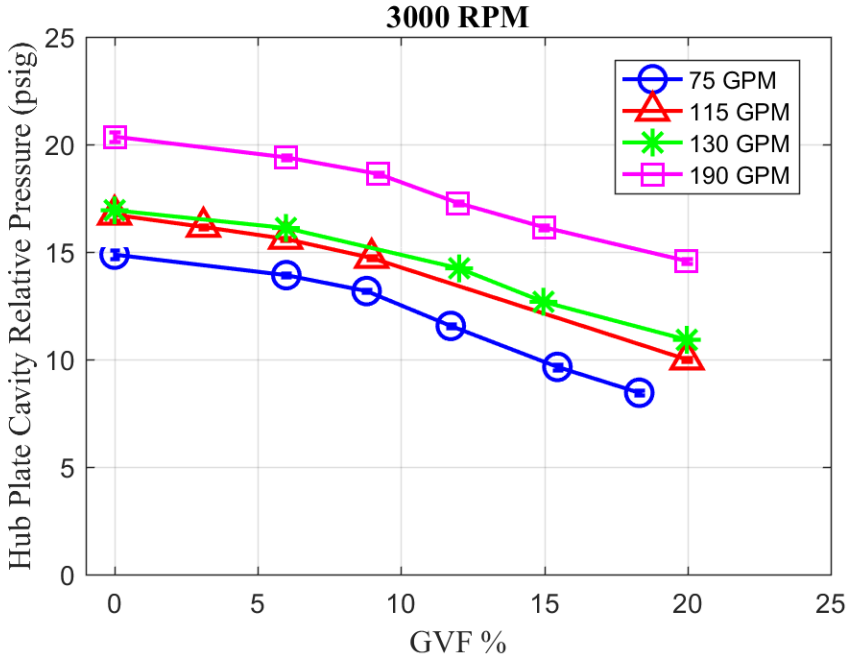

Figure 4-32: GVF vs Hub Plate Cavity Relative Pressure @ 3000 RPM

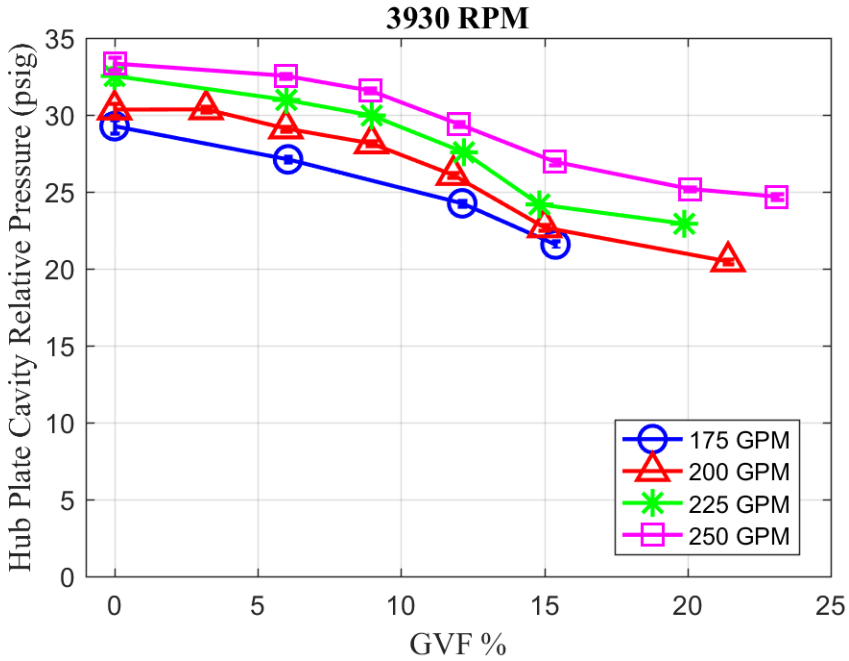

Figure 4-33: GVF vs Hub Plate Cavity Relative Pressure @ 3930 RPM

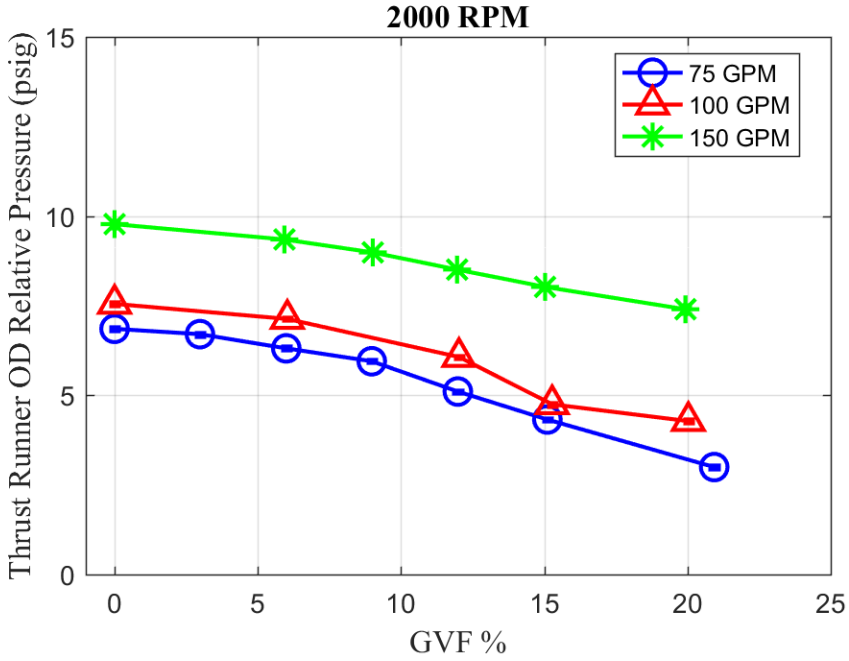

Figure 4-34: GVF vs Thrust Runner OD Relative Pressure @ 2000 RPM

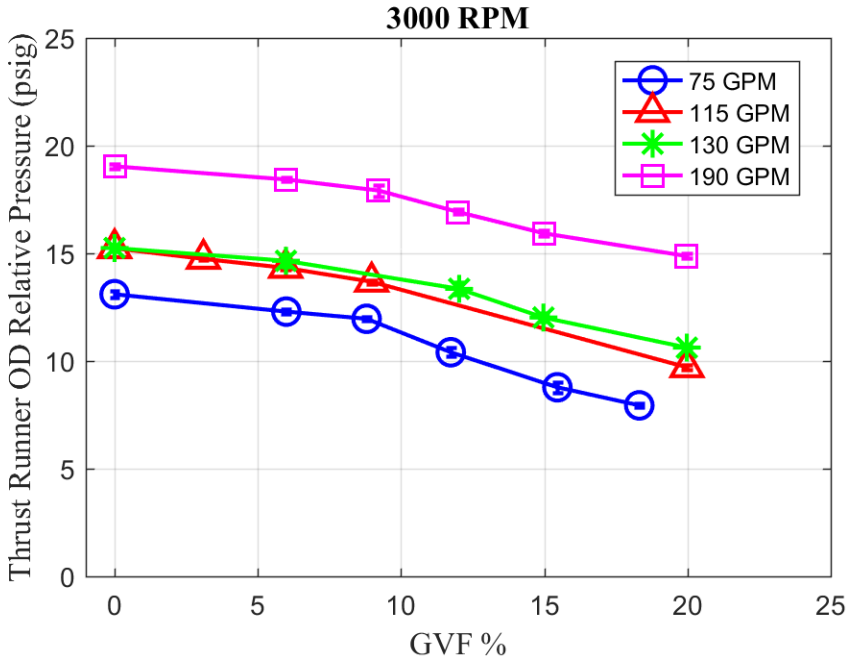

Figure 4-35: GVF vs Thrust Runner OD Relative Pressure @ 3000 RPM

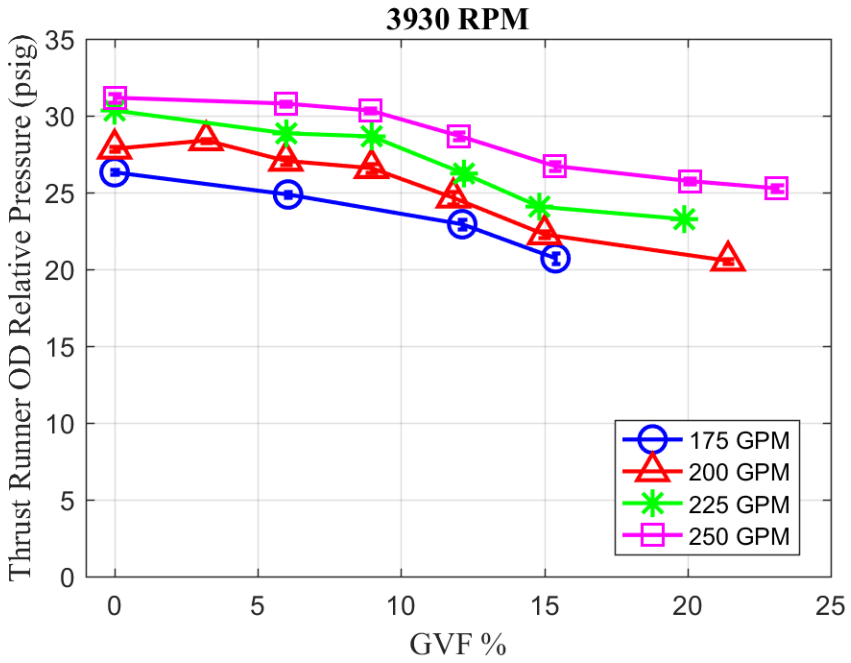

Figure 4-36: GVF vs Thrust Runner OD Relative Pressure @ 3930 RPM

The thrust runner OD relative pressure measures the pressure difference between the stator jacket and thrust runner OD (Outer Diameter) position. There is about a 5 psig differential pressure drop when GVF increasing from 0% to 20 % for 3000 RPM and 3930 RPM. For 2000 RPM case, the pressure drop is about 2.5 psig as shown in Figure 4-34 to Figure 4-36.

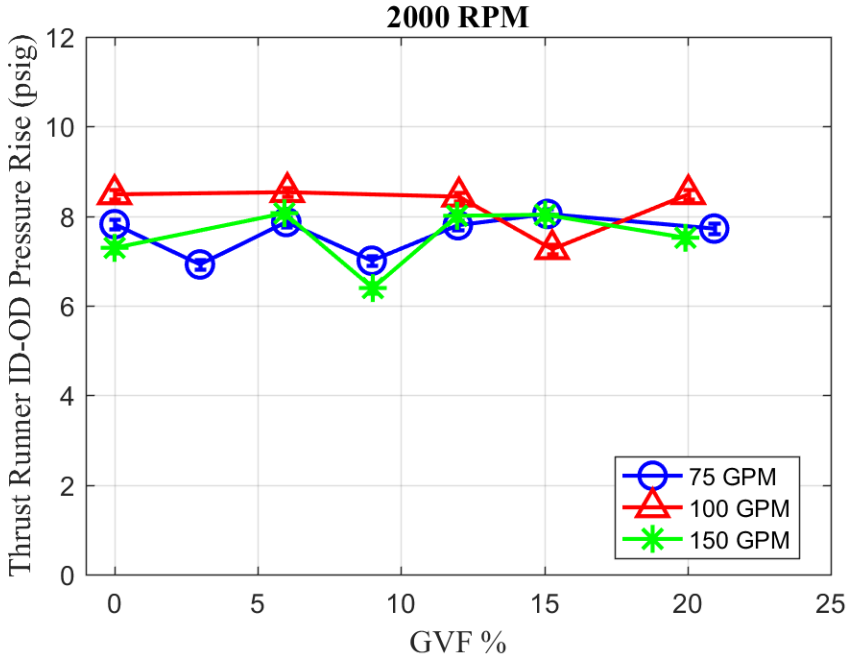

Figure 4-37: GVF vs Thrust Runner ID-OD Pressure Rise @ 2000 RPM

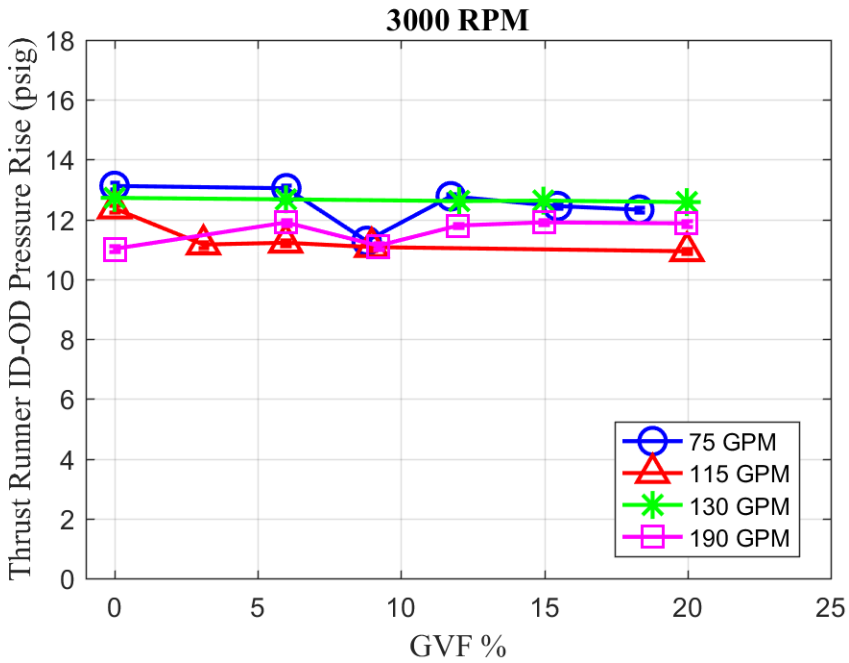

Figure 4-38: GVF vs Thrust Runner ID-OD Pressure Rise @ 3000 RPM

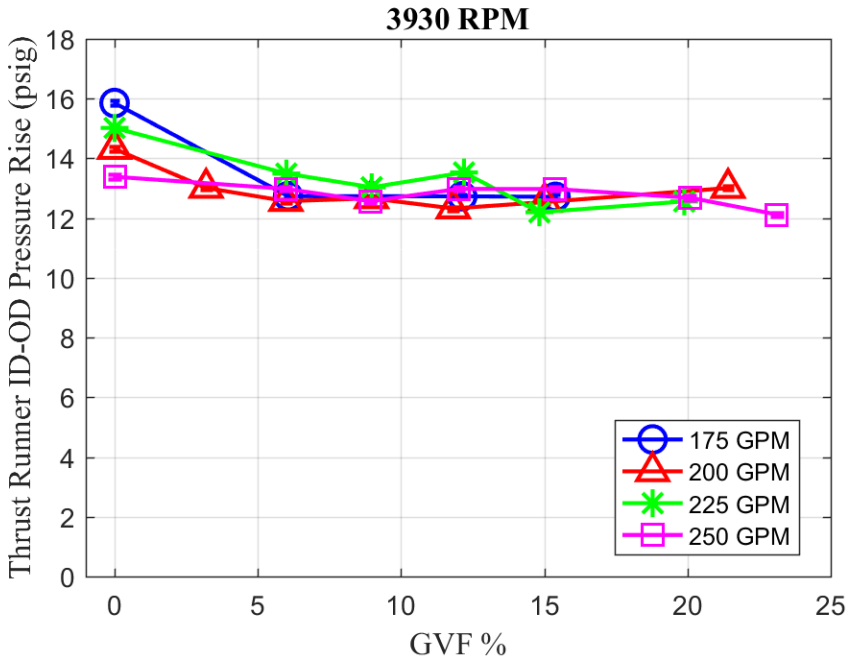

Figure 4-39: GVF vs Thrust Runner ID-OD Pressure Rise @ 3930 RPM

In Figure 4-37 to Figure 4-39, the thrust runner ID-OD pressure rise measures the pressure difference between the thrust runner ID (inner diameter) and OD positions. There is about a 13 psig pressure drop for the 3930 RPM case, 12 psig for 3000 RPM case and 9 psig for 2000 RPM case. The GVF in the stator jacket doesn't change the pressure distribution from ID to OD, which can be interpreted as air content is so little that pressure distribution on the thrust runner is not affected.

4.1.5 Vibration Level Analysis

During the test, two tri-axial accelerometers are installed at the top and bottom flange of the canned motor pump. The vibration levels of the canned motor pump are monitored during the test. The time series of measured vibration data are transformed through FFT

and interpreted in the frequency domain. Each accelerometer is installed so that x-axis corresponds to pump radial direction, y-axis corresponds to pump tangential direction and z-axis corresponds to axial direction. In Figure 4-40 through Figure 4-45, the Frequency vs Vibration acceleration amplitude is shown for 2000 RPM, 3000 RPM and 3930 RPM respectively. In Figure 4-46 to Figure 4-48, over-speed 4250 RPM vibration characteristic is shown for different flow rate conditions. By comparing top side accelerometer and bottom side accelerometer, the vibration level is relative higher on the top than the bottom side, since the pump is anchored to the ground at bottom side. The amplitude peak at specific frequencies indicate pump's operation condition and impeller blade numbers. Thus, for 2000 RPM, 3000 RPM and 3930 RPM, there are peak amplitude at 34 Hz, 53 Hz and 67 Hz. This pump impeller has 6 blades. Thus, amplitude peak occurs at 120 Hz and 240 Hz for all conditions.

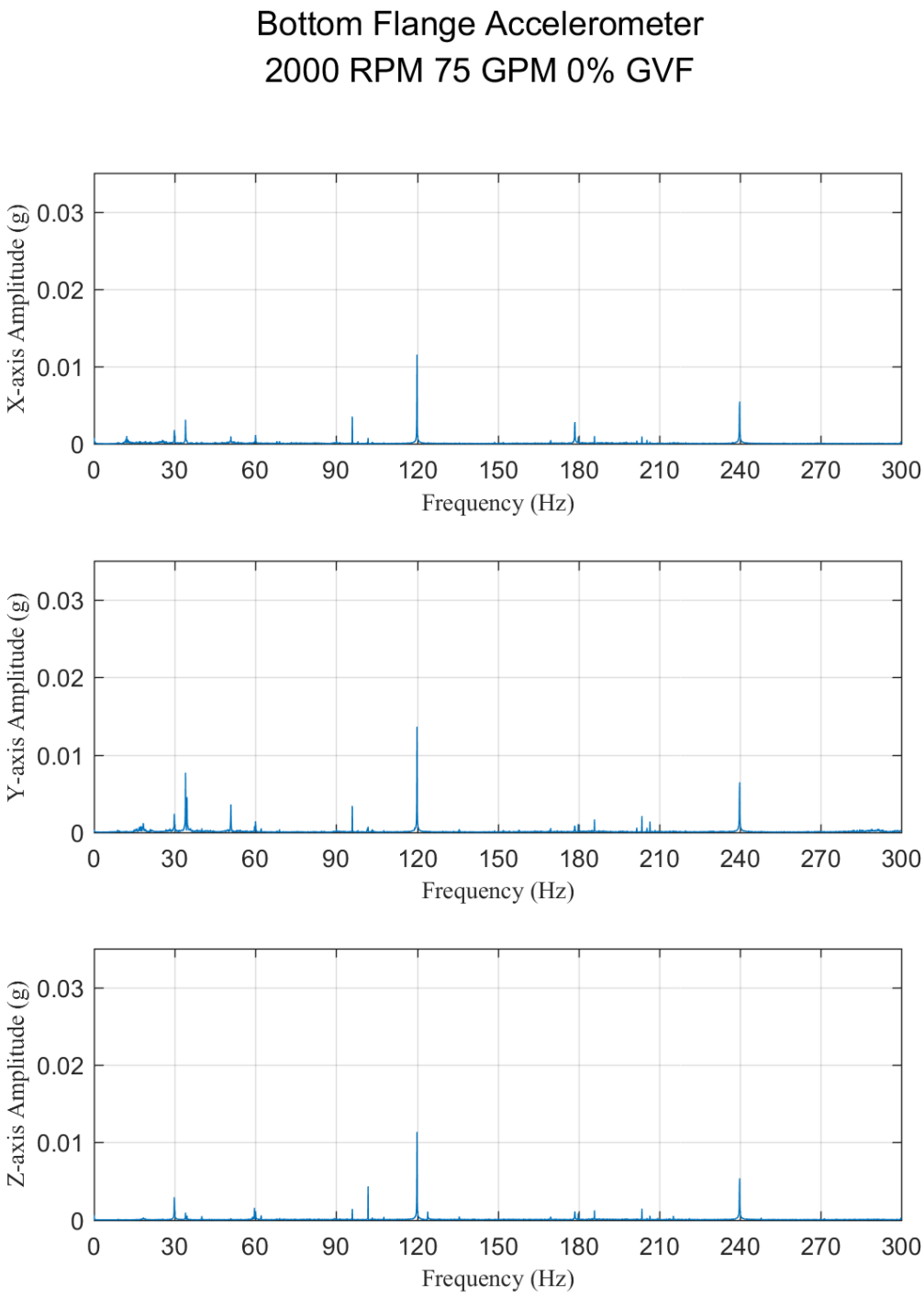

Figure 4-40: Bottom Flange Accelerometer @ 2000 RPM

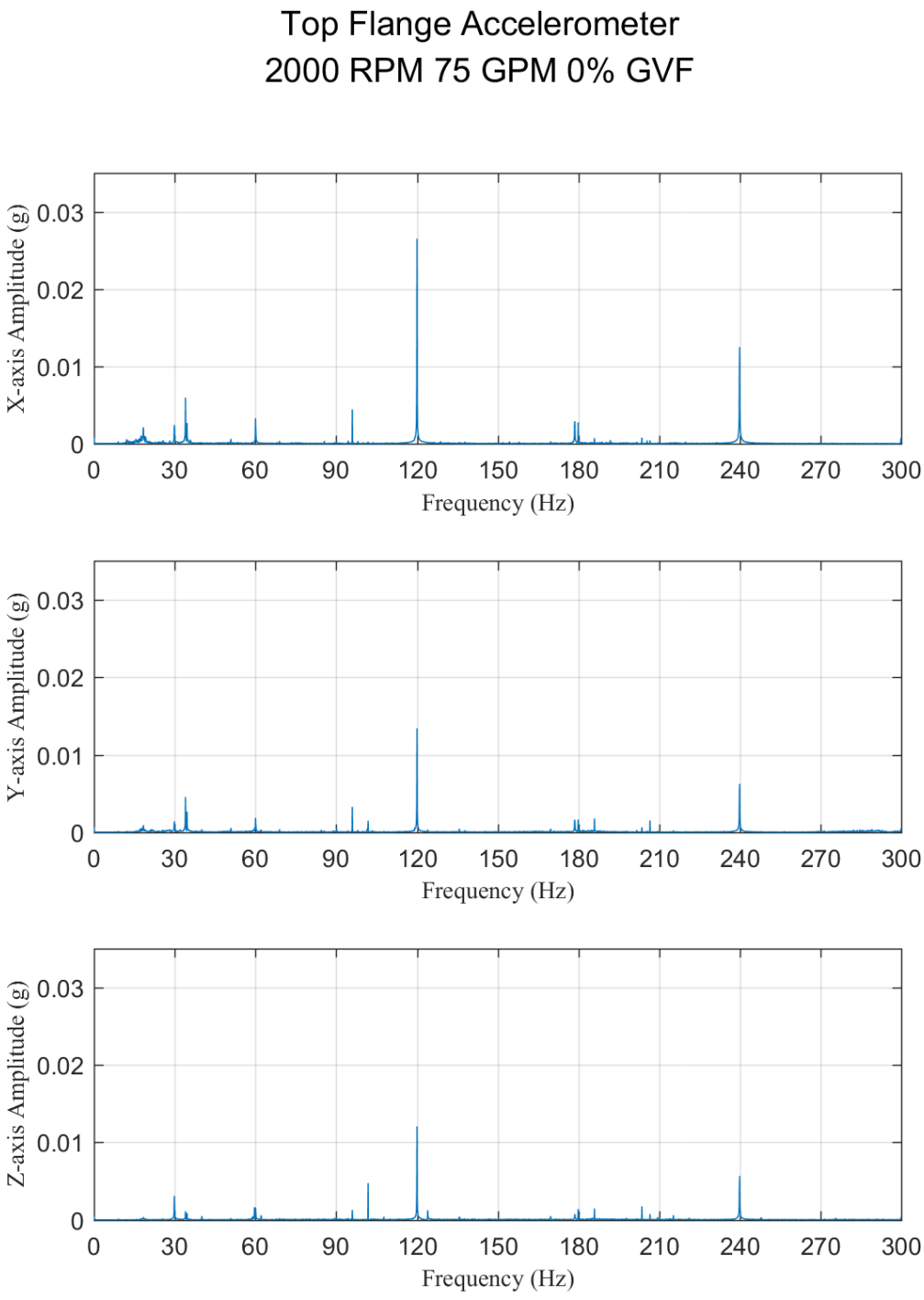

Figure 4-41: Top Flange Accelerometer @ 2000 RPM

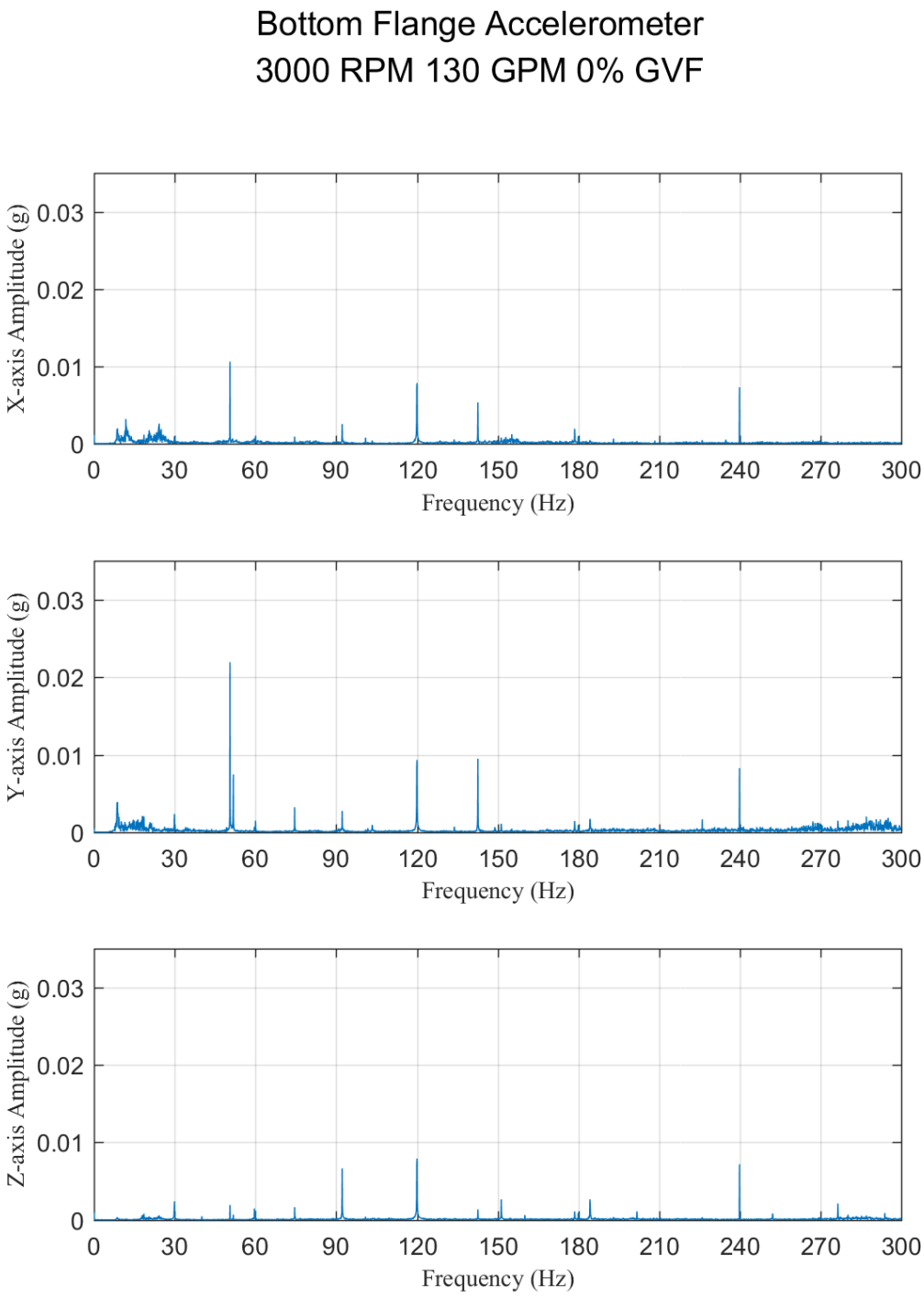

Figure 4-42: Bottom Flange Accelerometer @ 3000 RPM

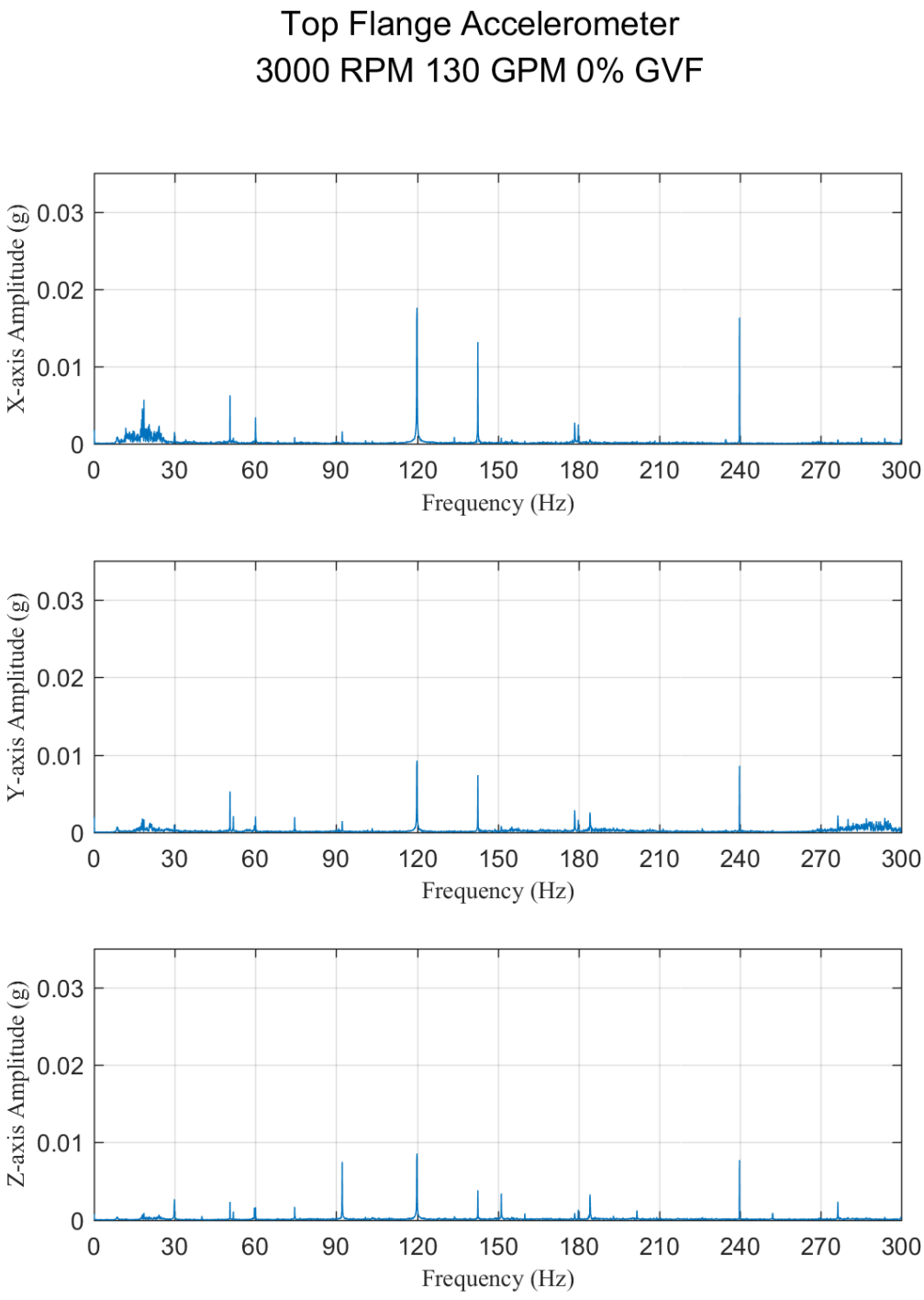

Figure 4-43: Top Flange Accelerometer @ 3000 RPM

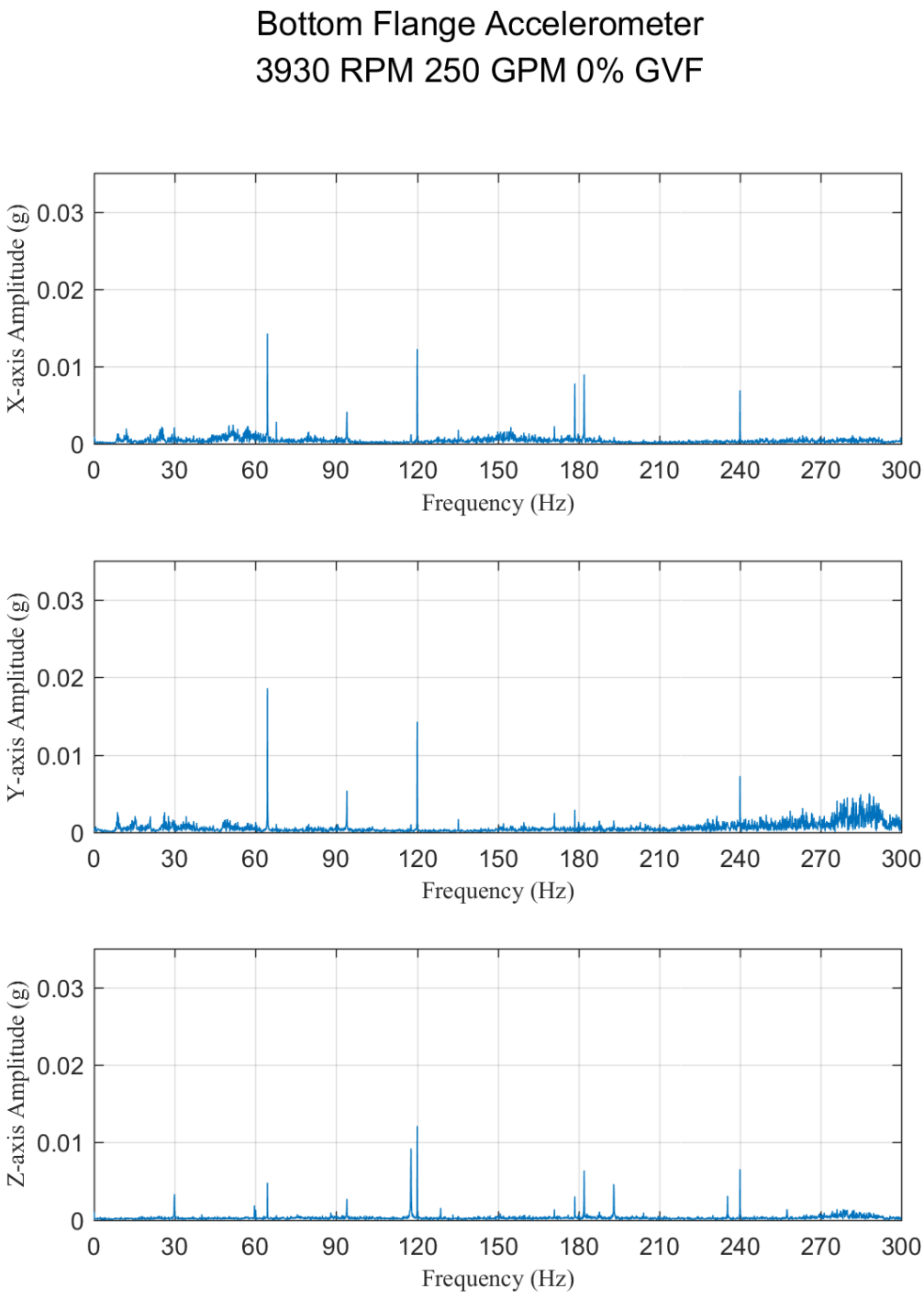

Figure 4-44: Bottom Flange Accelerometer @ 3930 RPM

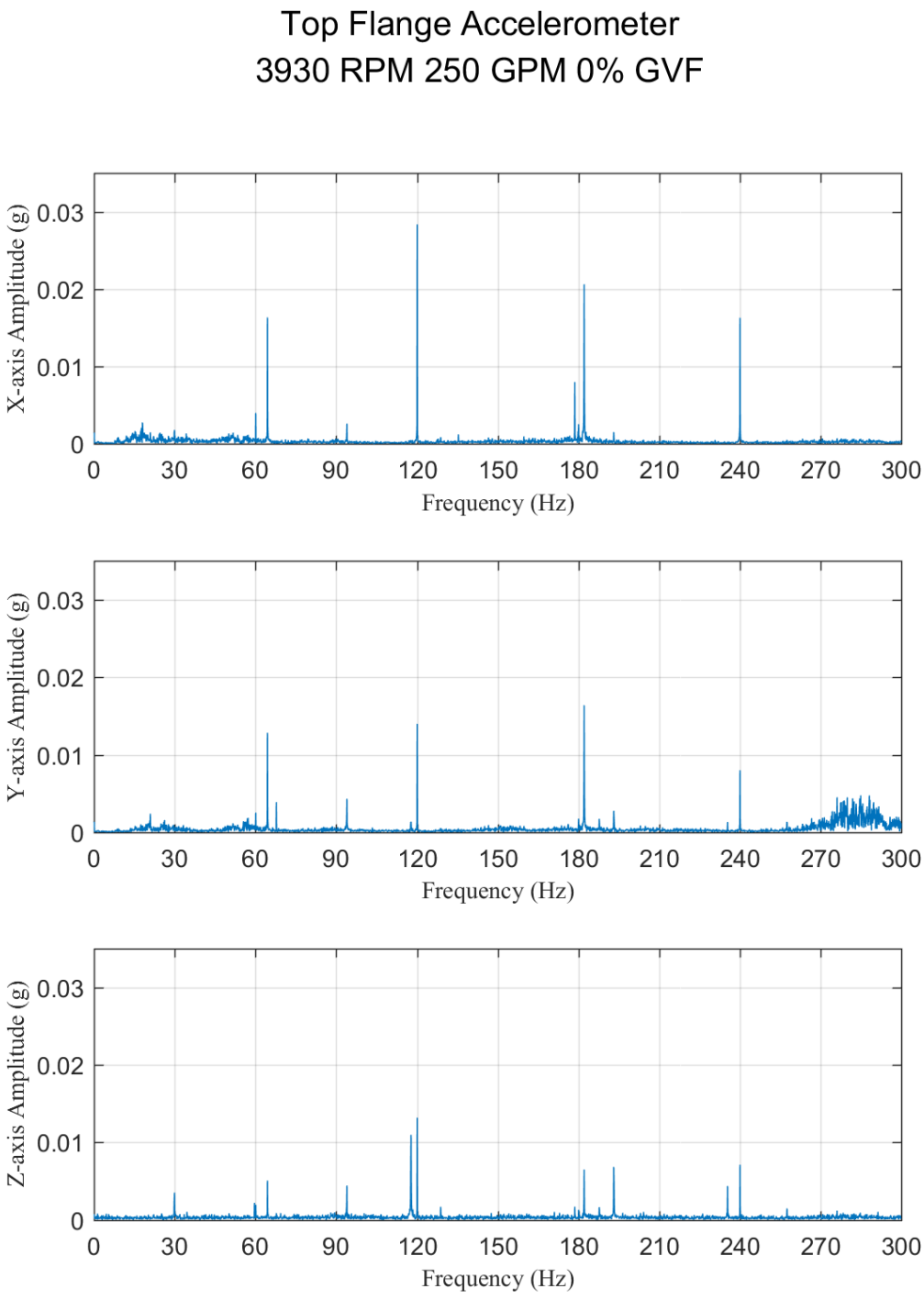

Figure 4-45: Top Flange Accelerometer @ 3930 RPM

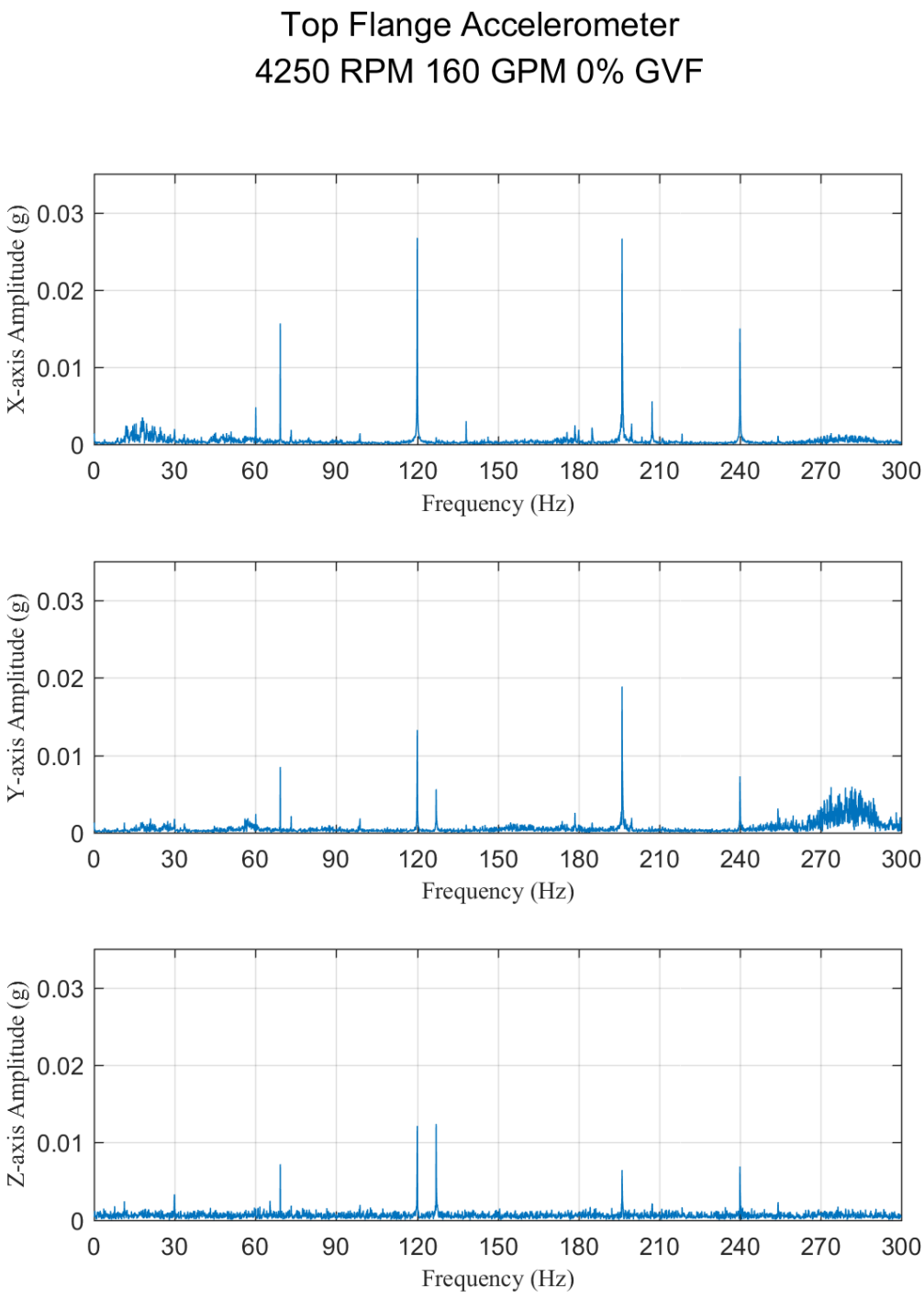

Figure 4-46: Top Flange Accelerometer @ 160 GPM

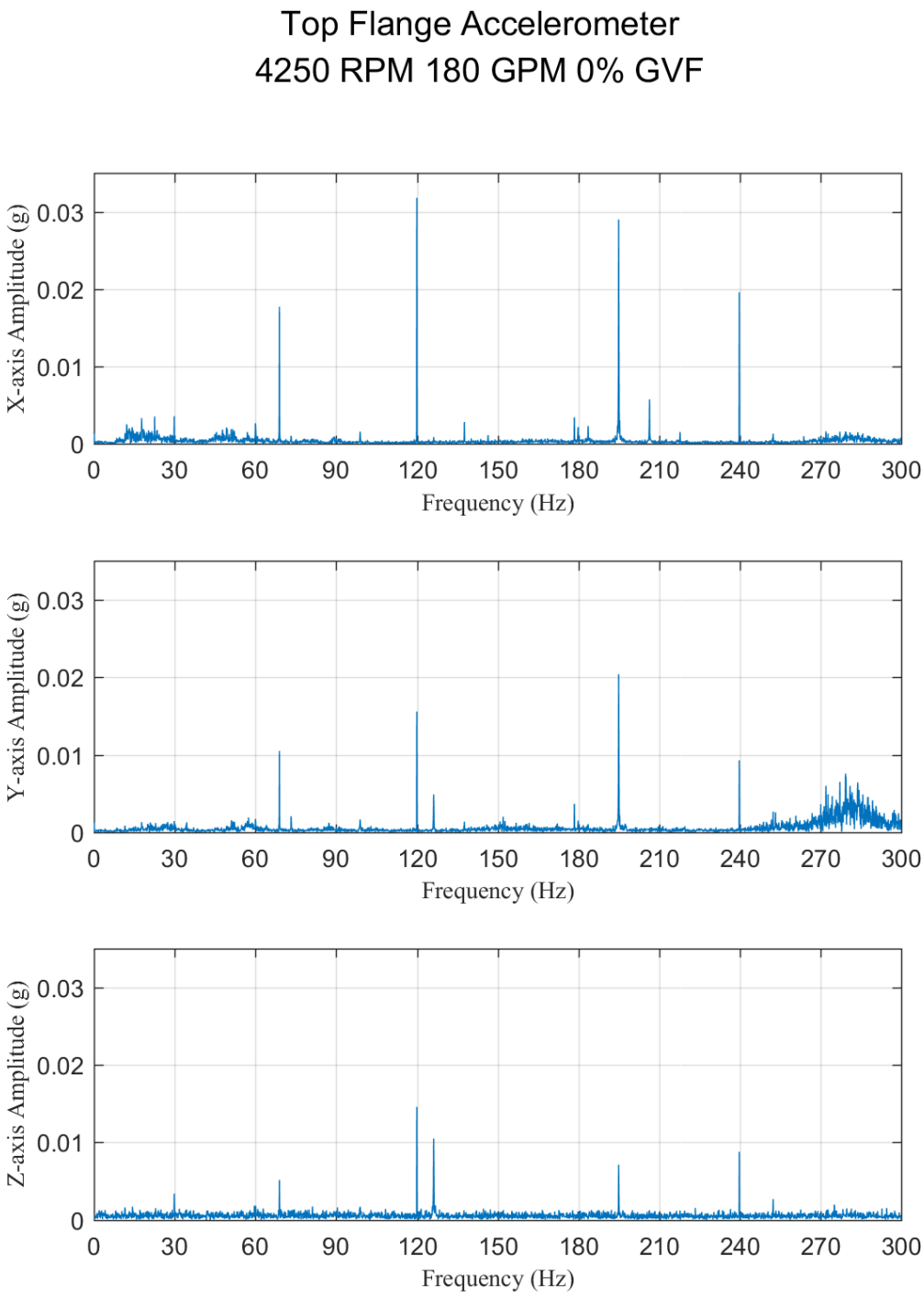

Figure 4-47: Top Flange Accelerometer @ 180 GPM

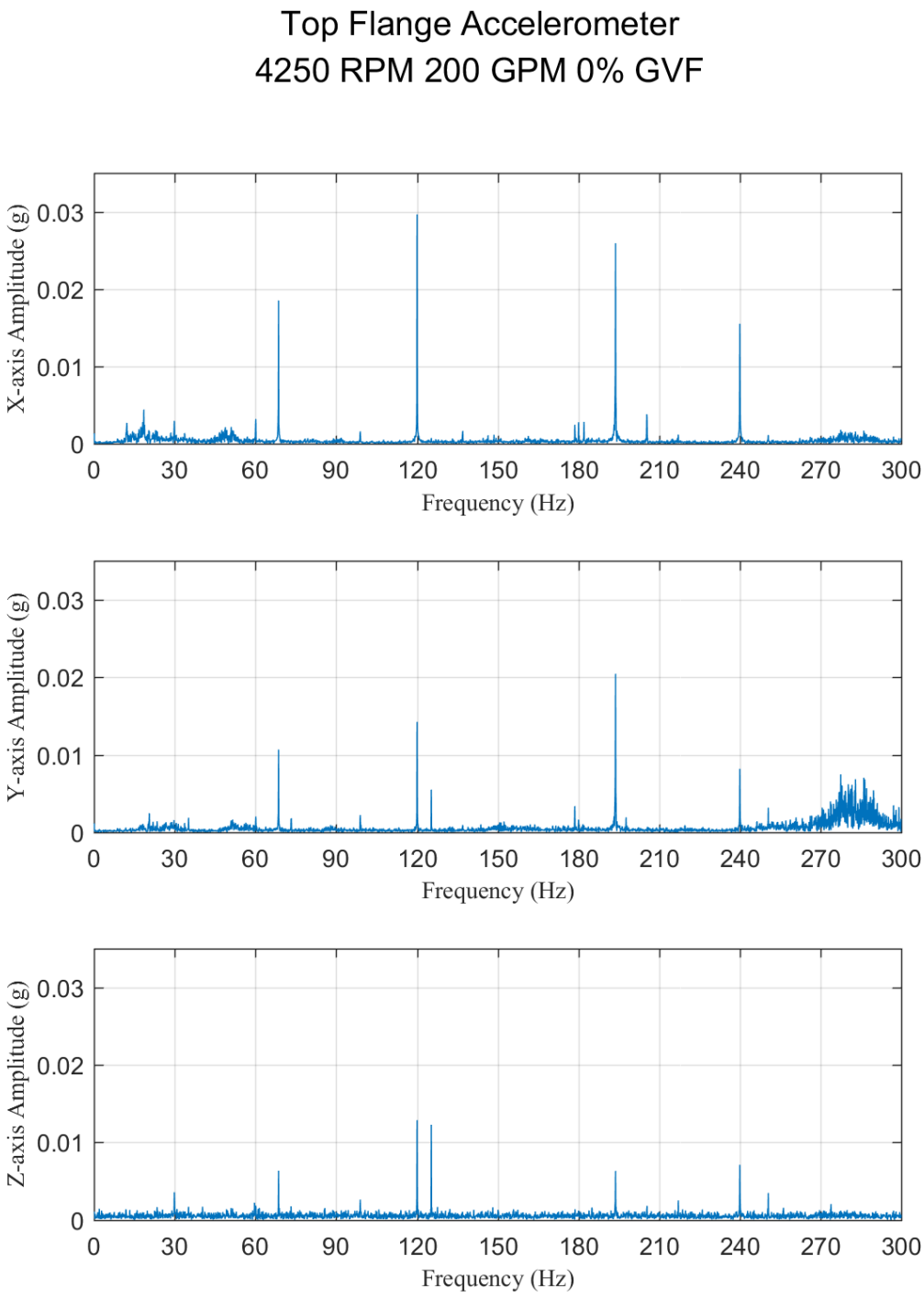

Figure 4-48: Top Flange Accelerometer @ 200 GPM

4.1.6 Thermal Analysis of the Canned Motor Pump

The motor winding temperature is monitored and recorded during all the test. It is important to maintain the motor winding temperature in an acceptable range during normal operation. Thus, during each multiphase test period, a single phase steady state thermal run is operated. The pump is operated at 3930 RPM and 250 GPM with no air injecting for 3-4 hours until the motor temperature reaches stable value.

One of the thermal run test result is shown in Figure 4-49. The motor temperature reaches around 280 deg F during the test with the water inlet temperature kept at 110 deg F. The maximum allowable motor winding temperature according to Curtiss Wright is 428 deg F. Thus, it is concluded that the motor can survive under full speed and high flow rate operation condition. For multiphase flow cases, the motor temperature and GVF are shown in Figure 4-50. It can be seen at full speed that even with air injected in the stator jacket, the maximum motor temperature reaches only 290 deg F.

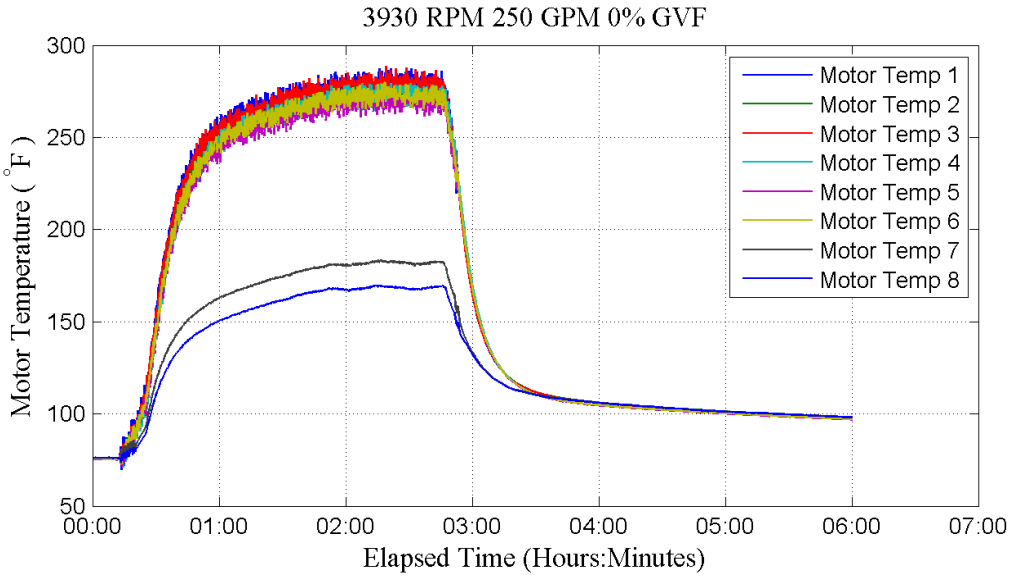

Figure 4-49: Single Phase Steady State Thermal Run

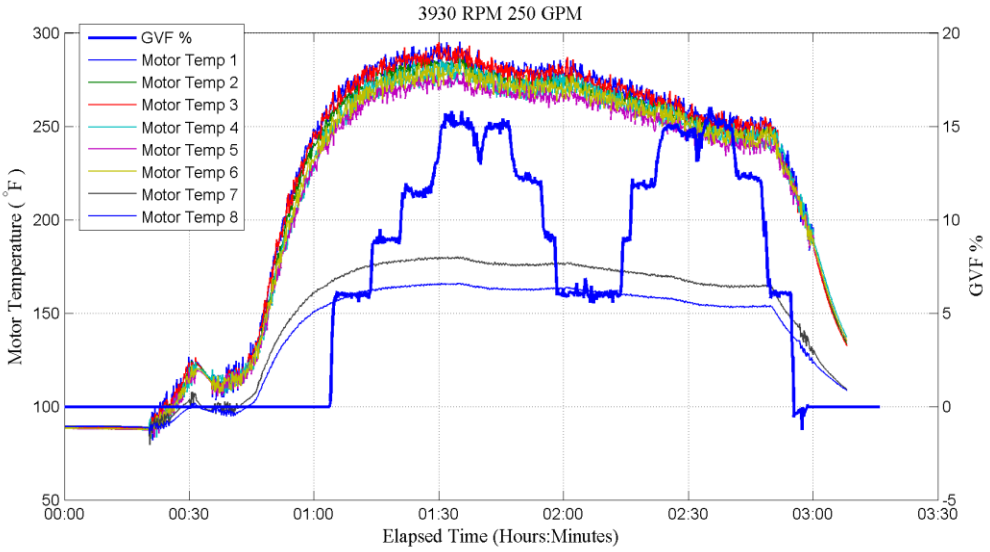

Figure 4-50: Motor Temperature under Multiphase Condition

The pump fluid temperature is measured at the pump inlet, hub plate cavity and pump discharge port. During the test, the fluid temperature will rise due to: (1) pump work rises

stagnation temperature, (2) motor winding heating effect and (3) friction losses in bearings and seals. Since the pump work mainly raises the fluid velocity instead of static temperature, and friction losses are minor compared to motor heating, fluid temperature changing inside the pump will indicate how effectively the motor is cooled.

Figure 4-51 to Figure 4-53 shows the temperature difference of pump discharge and pump inlet vs GVF. Air in the stator jacket has little effect on the temperature difference, which means the fluid is not heated very much by the motor with air injection. For 3000 RPM case, the lower flow rate at 75 GPM shows higher temperature difference than the 190 GPM case. This is due to the lower flow rate, fluid moving slower allows the motor more time to transfer heat to the fluid. Also, since higher rotation speed needs higher motor power, the temperature difference is also higher for full speed cases.

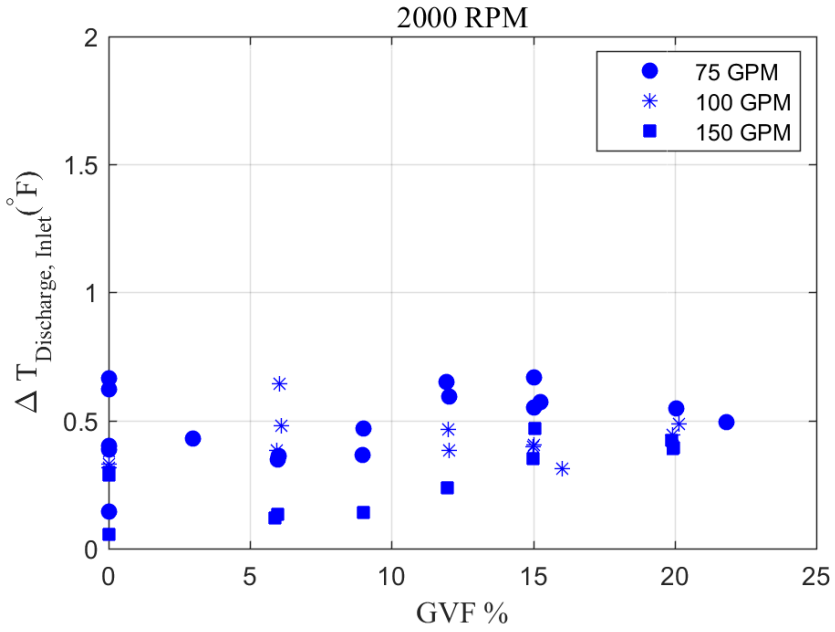

Figure 4-51: Temperature Difference of Pump Inlet and Outlet @2000 RPM

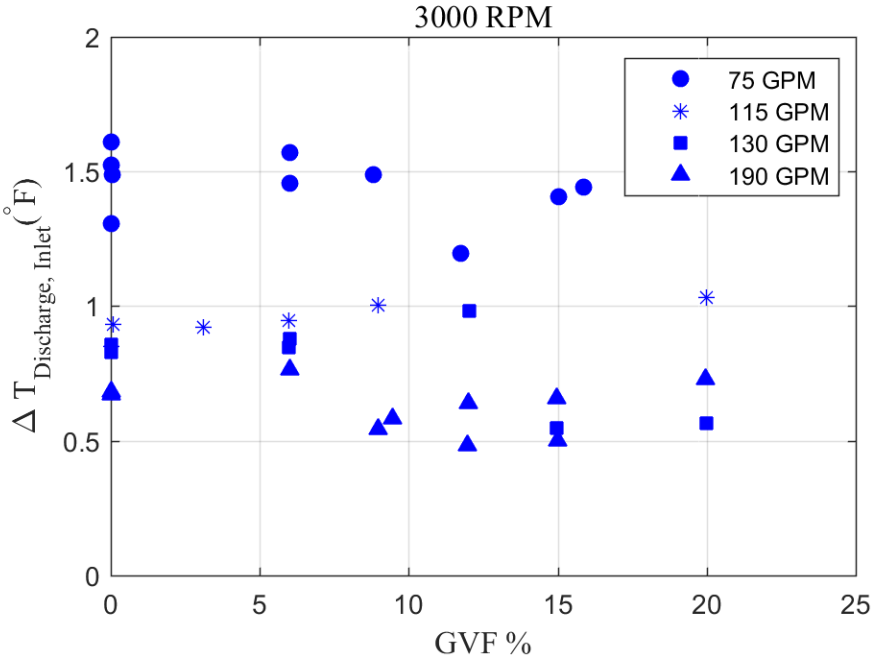

Figure 4-52: Temperature Difference of Pump Inlet and Outlet @3000 RPM

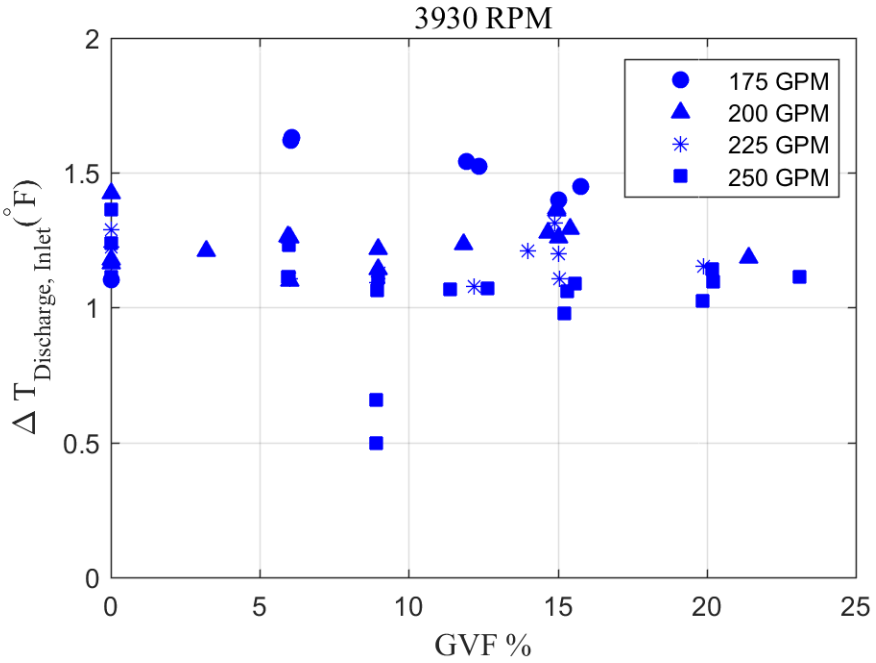

Figure 4-53: Temperature Difference of Pump Inlet and Outlet @3930 RPM

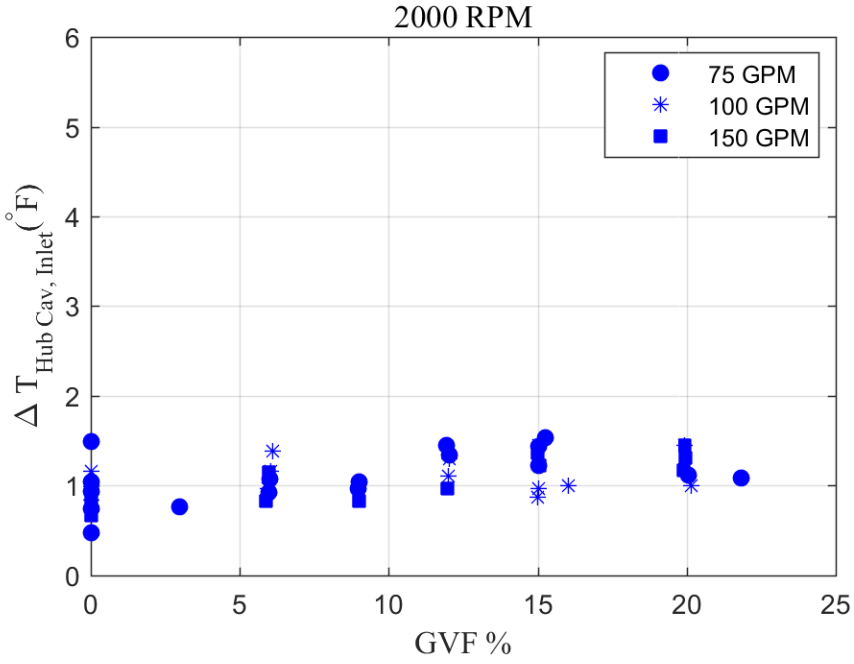

Figure 4-54: Temperature Difference of Pump Inlet and Hub Cavity @2000 RPM

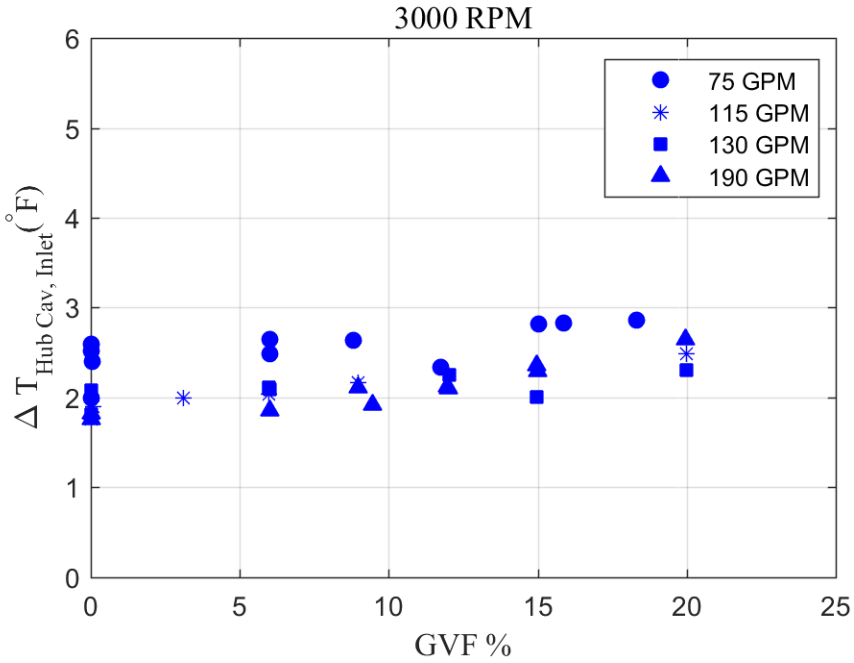

Figure 4-55: Temperature Difference of Pump Inlet and Hub Cavity @3000 RPM

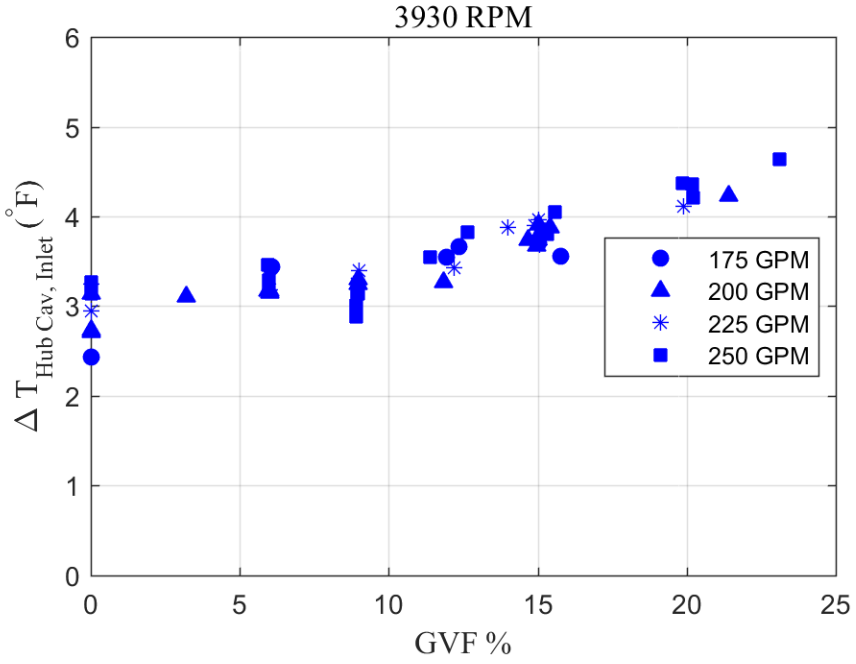

Figure 4-56: Temperature Difference of Pump Inlet and Hub Cavity @3930 RPM

In Figure 4-54 to Figure 4-56, temperature difference between the hub plate cavity and pump inlet vs GVF is plotted. Note that, the hub plate cavity is on the motor internal cooling flow path. Thus, the temperature rise in the hub plate cavity indicates that how much heat the fluid absorbed when passing through the motor bearings and motor can shaft annulus area. The stator jacket air injection will increase the temperature rise in the hub plate cavity. This is because the air injection in the stator will reduce heat conducting outward to stator jacket, and more heat will conduct inward to motor can shaft annulus. Thus, the fluid passing through the motor can shaft annulus will absorb more heat energy. The pump inlet flow rate does not significantly affect the hub plate cavity temperature rise. This is due to the motor internal cooling flow rate change is so small that this part of fluid temperature rise is not obvious.

4.2 CFD of Multiphase Flow inside Canned Motor Pump

The canned motor pump's internal flow path is simulated using CFD commercial software. The CFD results are reported in this section. Simulating the T-junction part which includes part of stator jacket, discharge pipe and thrust bearing cavity, the flow rate in the discharge pipe and thrust bearing cavity can be determined. The GVF at each exit port can also be obtained. This result is compared with the Venturi test prediction.

First, a grid independence check is performed for three different grid size cases. The outlet water mass flow rate at the discharge port and inlet pressure are chosen as criterion. Three different node numbers of meshes are generated to study grid independence. From Figure 4-57 and Figure 4-58, the change of outlet mass flow rate and inlet pressure from 0.5 million to 1.1 million nodes is 0.087% and 0.06%, and the rate of change from 1.1 million to 2.2 million nodes is 0.0092% and 0.0018%. Thus, we chose 1.1 million nodes for the future CFD simulation considering calculation accuracy and computer time cost.

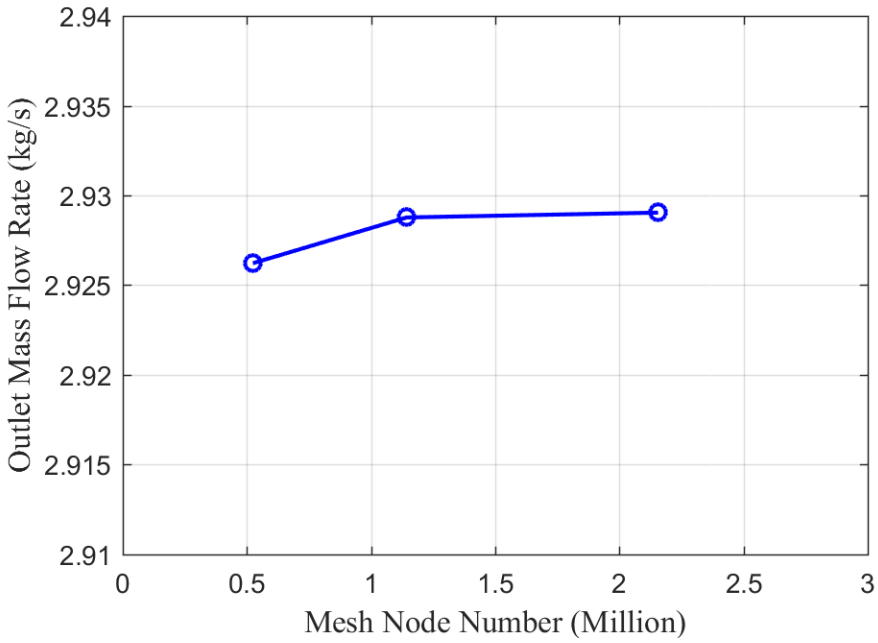

Figure 4-57: Grid Independence Check on Mass Flow Rate

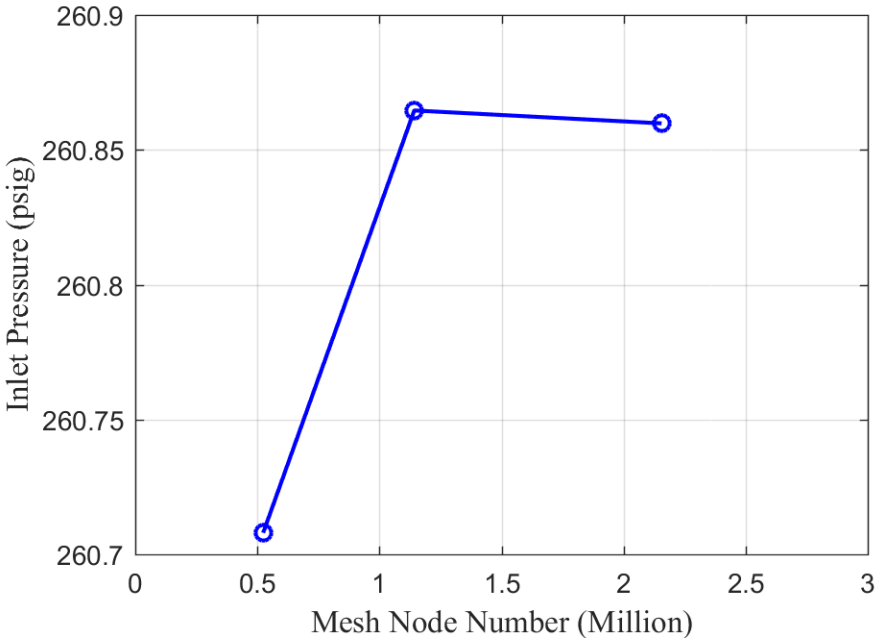

Figure 4-58: Grid Independence Check on Inlet Pressure

4.2.1 Single Phase Simulation

First, single phase flow is simulated for this flow region. Water is chosen for the simulation fluid. The inlet boundary is set as “mass flow rate” type, and both outlets are set as “pressure outlet” type. “Periodic” type is set for the cut plane of flow region, and the other boundaries are set as “wall”. Initial pressures at inlet and outlet are based on experimental measured data of the stator jacket pressure, pump discharge pressure and thrust bearing cavity pressure. The inlet mass flow rate is calculated from the stator jacket water volume flow rate and water density. This stator jacket water volume flow rate is calculated in Figure 4-5. The iteration program in Section 4.1.1 calculated the stator jacket mass flow rate based on pump inlet flow rate. CFD method presented here is using this stator jacket mass flow rate to predict pump discharge flow rate. Due to mass conservation, pump inlet flow rate equals to pump discharge flow rate. By comparing the pump discharge flow rate, the CFD method and Venturi test prediction method can be compared and validated. Results for the flow rate distribution are shown in Figure 4-59 to Figure 4-61. CFD simulation predicts that with the single phase application, more flow rate in stator jacket or pump inlet doesn’t appreciably increase the motor internal cooling flow rate. In Figure 4-61, the mass flow rate ratio of the internal flow even decrease when the pump inlet flow rate increases. The Venturi method prediction results in Section 4.1.1 are also shown in these three figures. It can be seen that the error between CFD prediction and Venturi test method prediction on flow rate distribution is negligible.

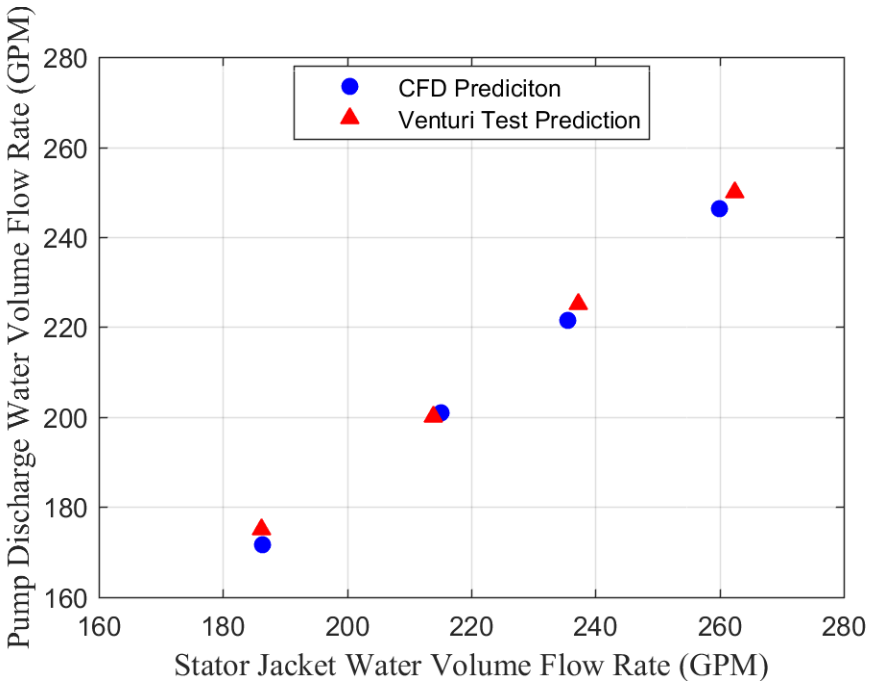

Figure 4-59: CFD prediction on Flow Rate Distribution

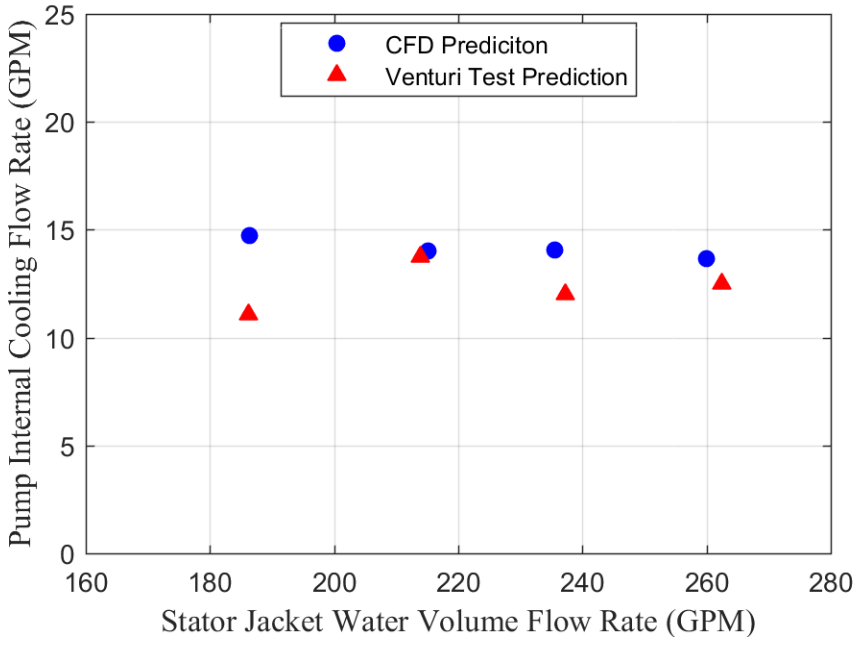

Figure 4-60: CFD Prediction on Internal Cooling Flow Rate

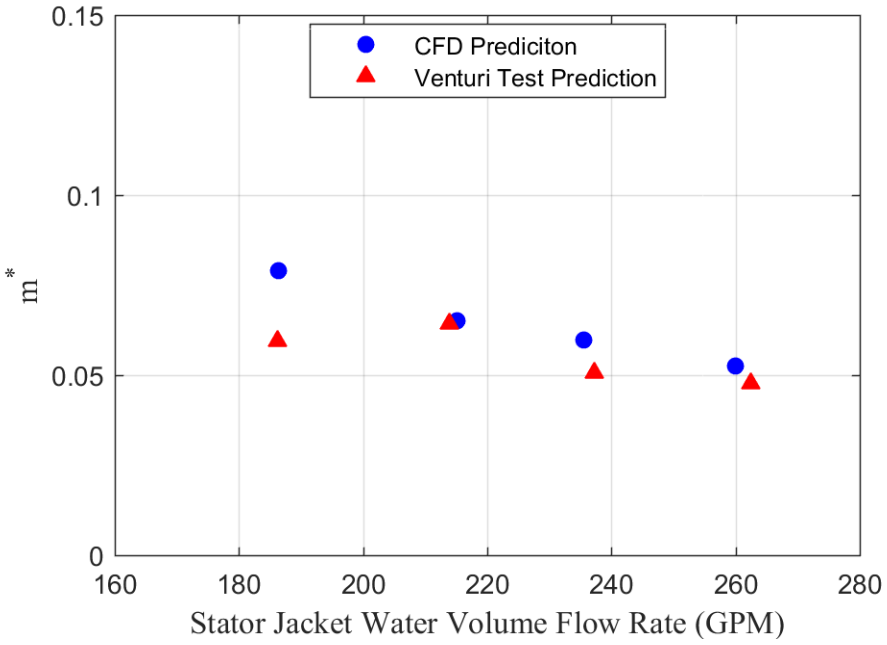

Figure 4-61: CFD Prediction on Mass Flow Rate Ratio

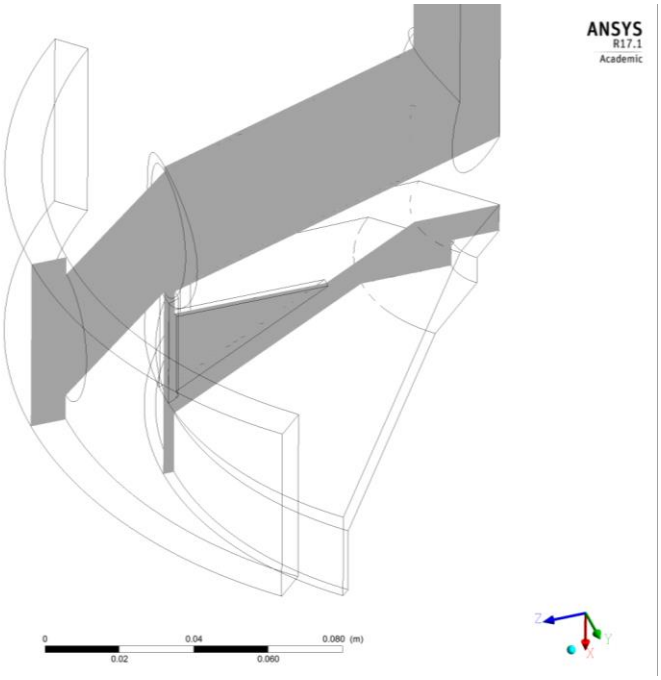

Figure 4-62: Cross Cut Plane for Post Process

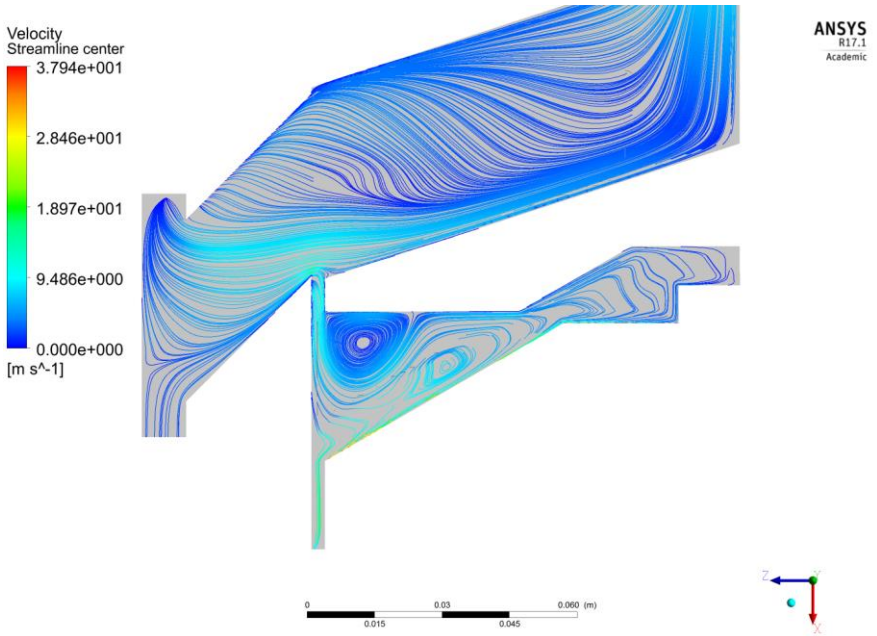

Figure 4-63: Velocity Stream Line on Cut Plane

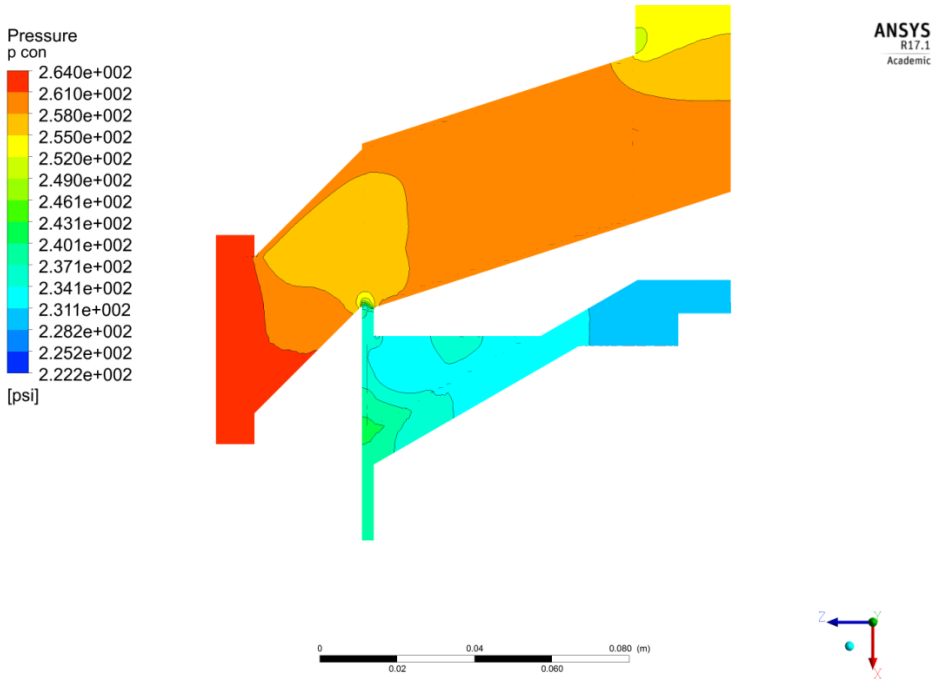

Figure 4-64: Pressure Contour on Cut Plane

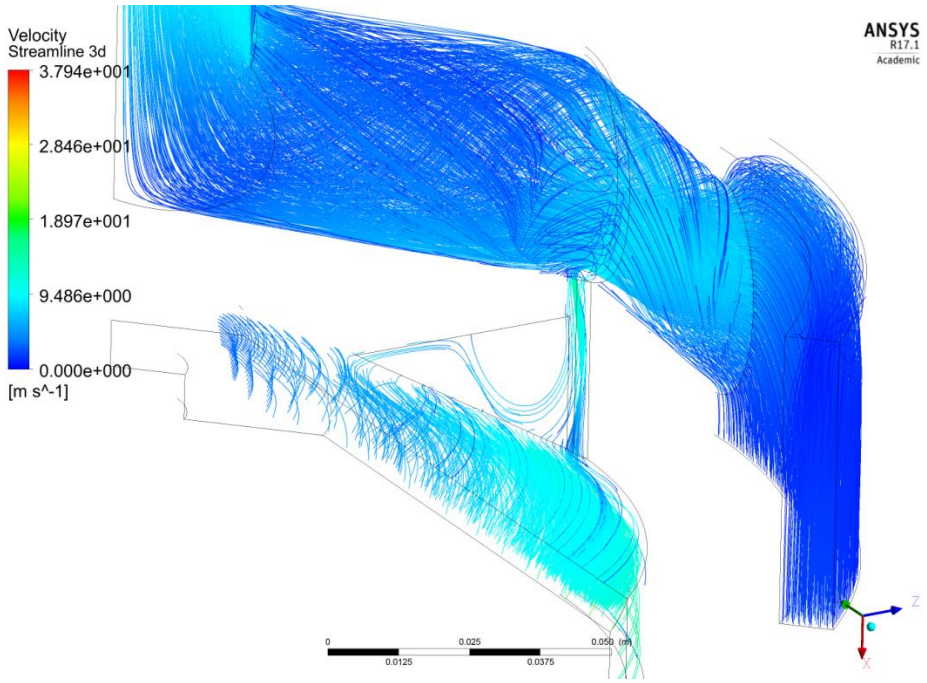

Figure 4-65: 3D Streamline of Flow Region

In Figure 4-63 to Figure 4-65, the flow field details of CFD are shown. A cross plane is created at the center of this flow region to show the flow diversion and pressure distribution. Figure 4-63 shows the water velocity streamline on the cut cross plane. Notice that there is large vortex in the thrust bearing cavity slot area. The flow area increases suddenly when fluid comes into thrust bearing cavity. A separation region forms. In the thrust bearing cavity, due to the rotation of thrust runner and fluid viscosity, fluid above the thrust runner also has a rotational movement along the pump axis. This rotation forms a centrifugal force that causes the pressure difference between the thrust runner ID and OD. At the axis of flow region, the pressure is lowest. 3D stream line is shown in Figure 4-65. There is a strong vortex flow inside the main discharge pipe.

4.2.2 Multiphase Flow Rate Distribution

For multiphase simulation cases, water and air are the simulated fluid. Air properties are determined by the ideal gas law. The inlet boundary condition is “mass flow rate”, and outlet boundary condition is “pressure outlet”. Inlet GVF is calculated based on inlet pressure and inlet mass flow rate. Outlet GVF is calculated based on mass conservation and outlet pressure. First we analyzed the water and air volume flow rate distribution respectively, and then the mass flow rate ratio is shown for further conclusion.

In Figure 4-66, the water volume flow rate in pump discharge pipe is shown. It can be seen that the discharge pipe water volume flow rate increases linearly with stator jacket water volume flow rate. Also, the Venturi test method result is shown in Figure 4-66. The water flow rate in pump discharge pipe based on CFD method is larger than that based on Venturi test method. This indicates that internal cooling flow rate from CFD method is smaller than that from Venturi test method. In Figure 4-67, the discharge pipe air volume flow rate almost equals to the stator jacket air volume flow rate. This indicates that though air volume increases in the stator jacket, most of the air still flows through pump discharge pipe. Note that Venturi test method cannot predict the air flow rate in the discharge pipe. Only the mixture mass flow rate can be obtained. Considering the air mass is negligible compared with water mass, one can regard the mixture mass flow rate as water mass flow rate. However, since air volume in discharge pipe is not negligible, GVF in the discharge pipe cannot be obtained by the mixture mass flow rate only.

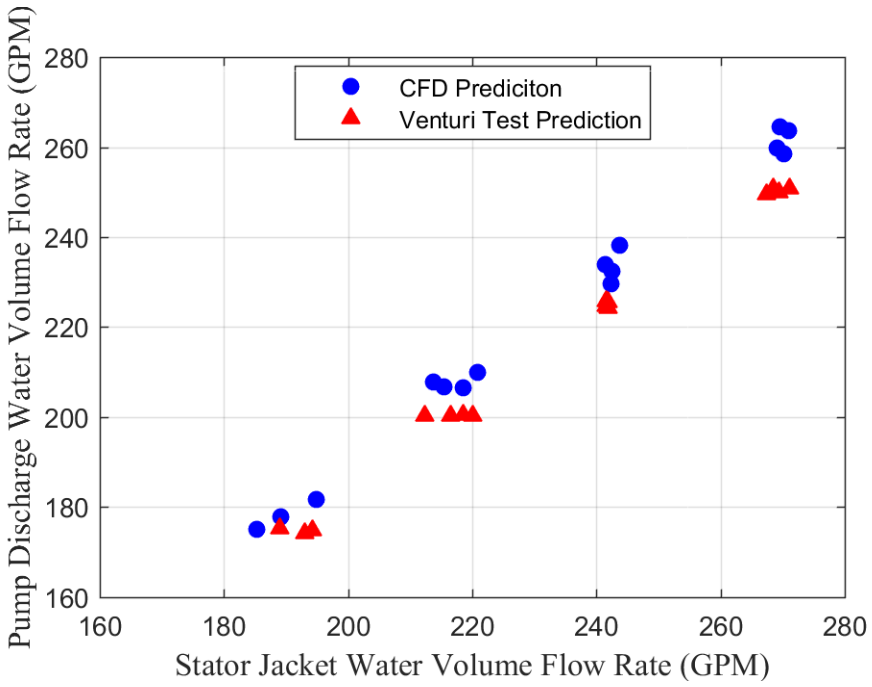

Figure 4-66: CFD prediction and Venturi test prediction on $Q_{\text{water discharge}}$

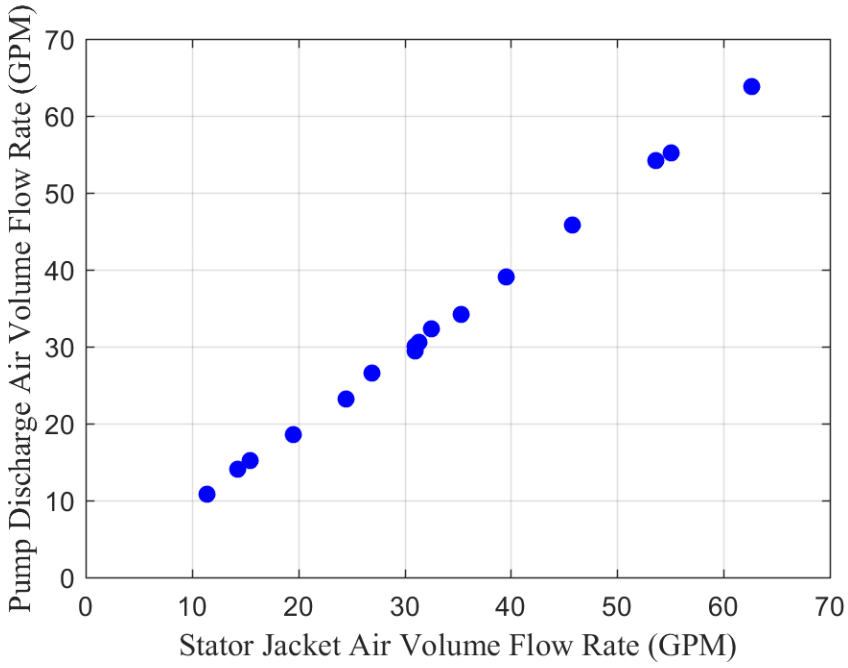

Figure 4-67: CFD Prediction on $Q_{\text{air discharge}}$

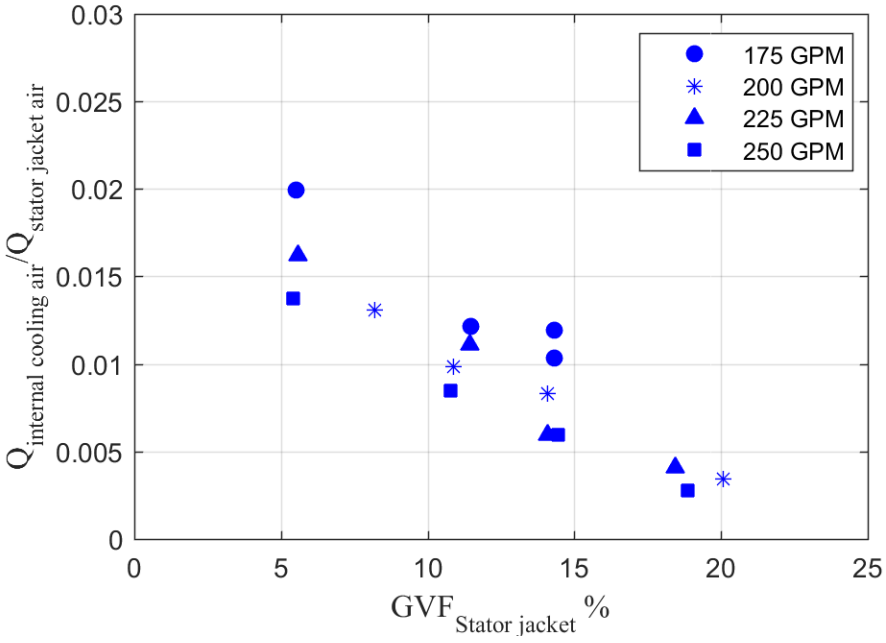

Figure 4-68: CFD Prediction on Air Volume Flow Rate Ratio

From Figure 4-68, a non-dimensional ratio is used to evaluate the amount of air distribution in the canned motor pump. The ratio of internal cooling air volume flow rate over the stator jacket air volume flow rate decreases with the increase of GVF in the stator jacket. The simulation result indicates that more air in the stator jacket reduces the drag forces that the fluid has to overcome through the discharge pipe, in which case more air is diverted to the discharge pipe.

The same trend also exists in the water distribution in Figure 4-69. As the stator jacket GVF increases, the ratio of internal cooling water flow rate over the stator jacket water flow rate also decreases. This trend is consistent with the experimental test result about the thrust force changing and thrust bearing cavity pressure changing. Lower internal

cooling water flow rate will increase axial thrust force, less pressure drop in thrust bearing cavity.

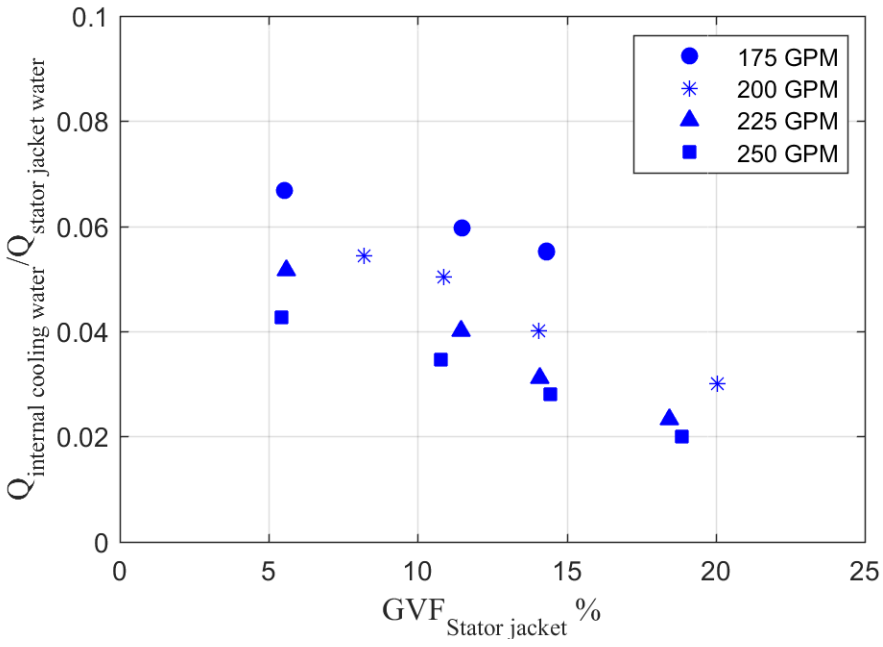

Figure 4-69: CFD Prediction on Water Volume Flow Rate Ratio

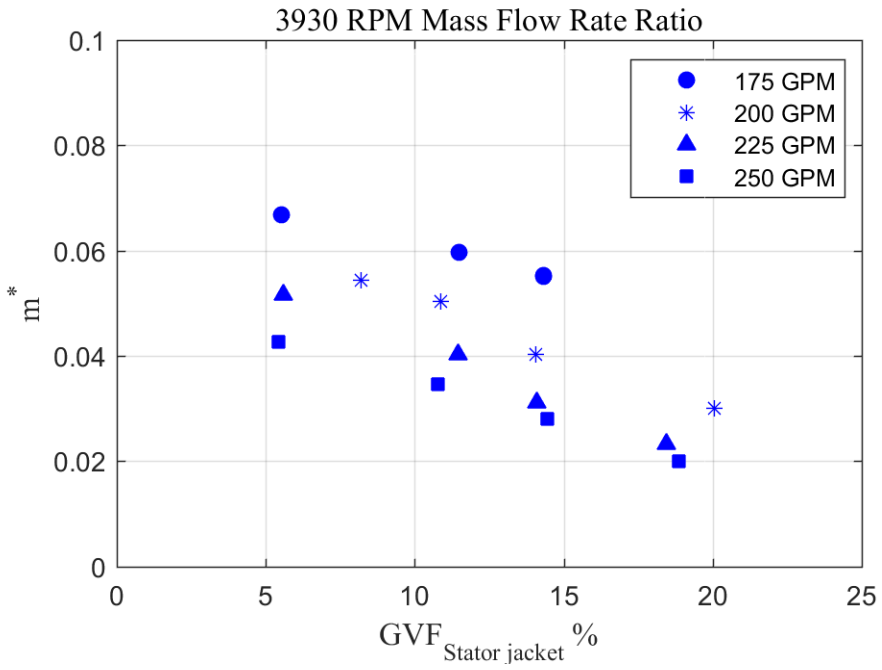

Figure 4-70: CFD Prediction on Mixture Mass Flow Rate Ratio

In Figure 4-70, the mixture mass flow rate ratio possesses the same distribution as the water volume flow rate ratio shown in Figure 4-69. This is due to the mixture mass flow rate is primarily a function of the water mass flow rate, and quality of mixture is almost zero.

The averaged GVF of the stator jacket, pump discharge pipe and thrust cavity outlet are shown in Figure 4-71. The GVF difference between stator jacket and pump discharge pipe is almost unnoticeable, while the GVFs at the thrust bearing cavity outlet all stay below 5%. It doesn't change much with stator jacket GVF.

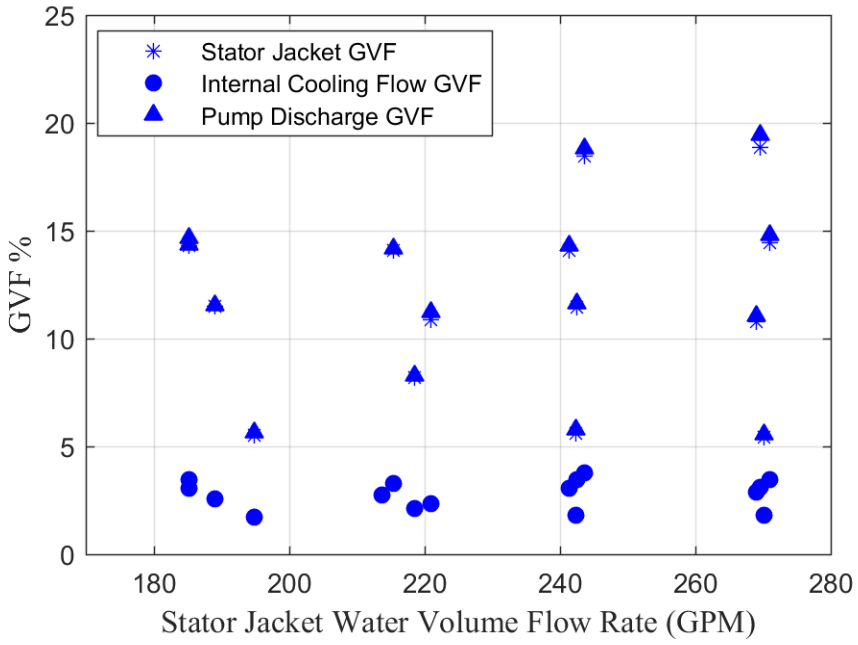

Figure 4-71: CFD of Averaged GVF at Boundary

4.2.3 Multiphase Flow Field Analysis

The flow field of the multiphase simulation is shown in this section. The cases shown here are the cases with same discharge water flow rate (200 GPM) and different stator jacket GVF. The inlet boundary condition setting is based on experimental results. First the streamlines of the center cross section for different stator jacket GVF are shown in Figure 4-72. There is a large vortex formed in the thrust bearing cavity. This is partly due to the fluid flowing quickly into the thrust bearing cavity, forming a jet flow, and the sudden enlarged area at the thrust cavity causes a separation region. The rotation of the runner also makes the fluid inside the thrust cavity to rotate. Thus, above the thrust runner, there is a circulation region. At the center of the vortex, fluid velocity is very low. And also, near the thrust runner axis, the linear rotational speed is also very low. These two low

velocity fluid regions have lower turbulence intensity. Thus, the air bubbles will more likely concentrate at these two region and form bigger bubbles. This trend is clearly shown in Figure 4-.

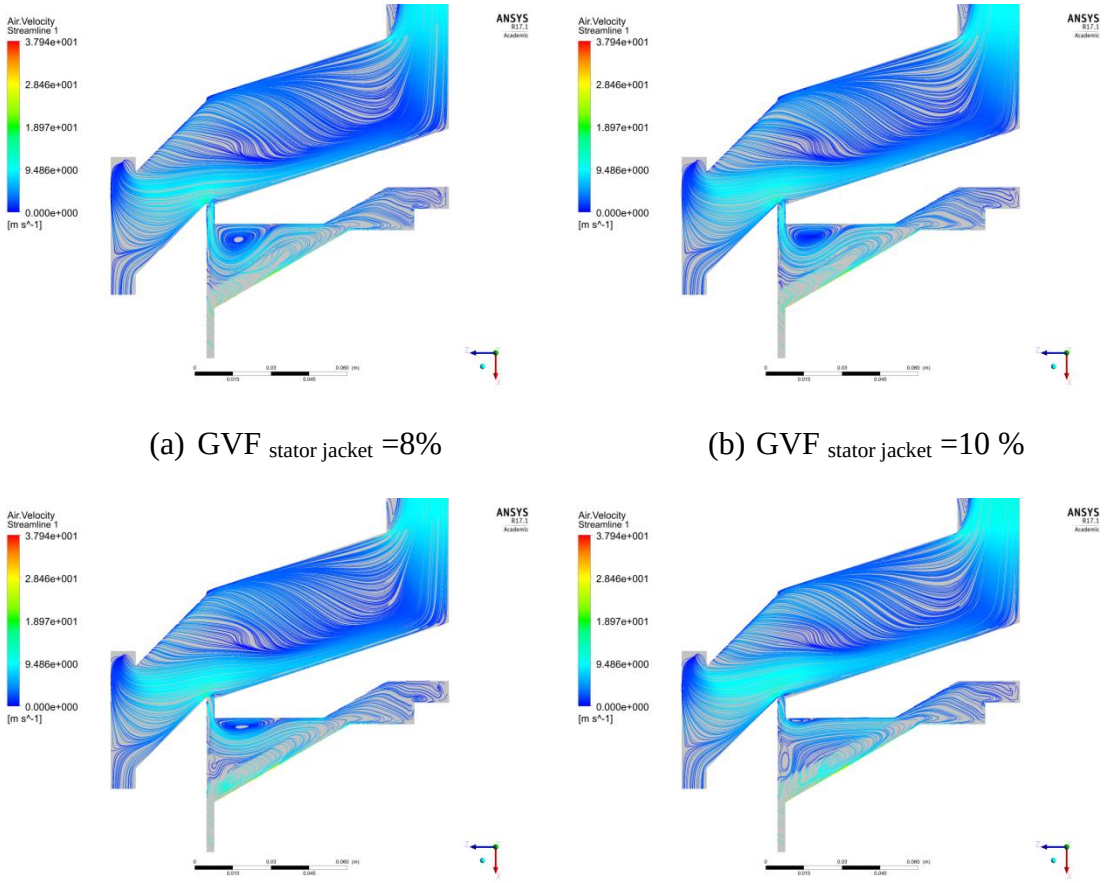

(a) GVF $_{\text{stator jacket}}$ =8%

(b) GVF $_{\text{stator jacket}}$ =10 %

(c) GVF $_{\text{stator jacket}}$ =14%

(d) GVF $_{\text{stator jacket}}$ =20%

Figure 4-72: Water Velocity Stream Line

As the stator jacket GVF increases, the air content inside the flow region also increases. Thus, local GVF is higher in the pump discharge pipe for higher GVF cases. However, in low GVF cases, a larger bubble is located at the vortex region. For GVF=20% case, air concentrating at the thrust runner slot becomes much smaller. From comparison of air

streamline in Figure 4-74 and Figure 4-75, we can find the reason. For the 20% case, the vortex region in the thrust bearing cavity is not forming because the water/air velocity (about 7m/s) coming down into the thrust bearing cavity is not large enough to form a separation zone. For the 8% cases, the velocity at throat slot is about 10 m/s. The high velocity flow penetrates deep into the thrust bearing cavity slot, forming a big vortex. At the swirl center, velocity is very low. Air is more likely concentrated in that position. Also, some air is concentrating near the pump axis. As the air flows into the thrust bearing cavity, it rotates with the thrust runner. Because air has lower density than water, water is thrown to the outer periphery of the thrust runner. Thus, more air stays near the axis center.

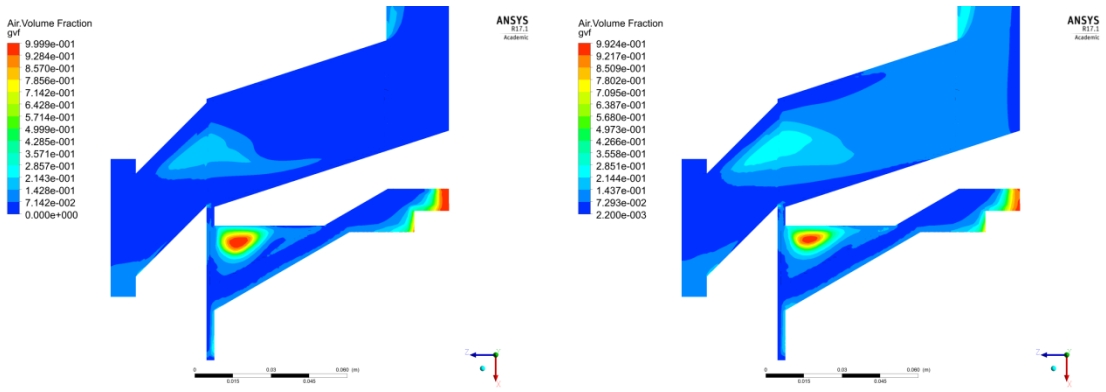

(a) GVF $_{\text{stator jacket}}$=8% (b) GVF $_{\text{stator jacket}}$=10%

Figure 4-73: GVF Contour for Different Stator Jacket GVF

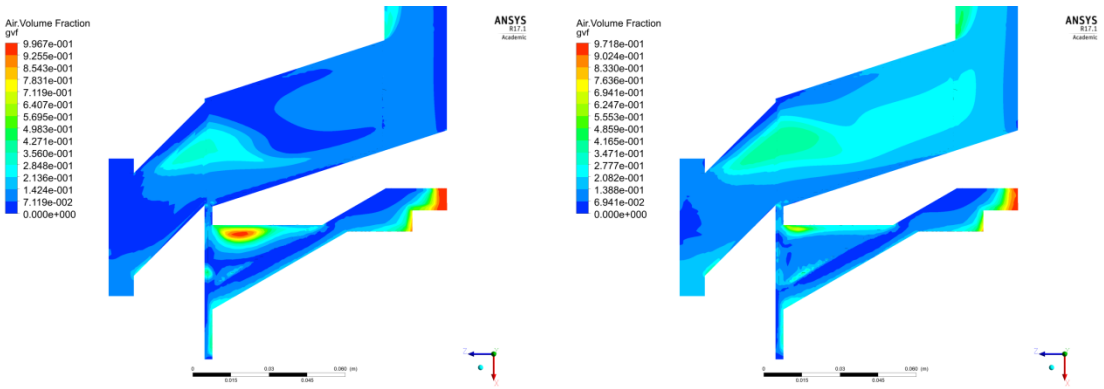

(c) GVF $_{\text{stator jacket}}$=14%

(d) GVF $_{\text{stator jacket}}$=20%

Figure 4-73: Continued

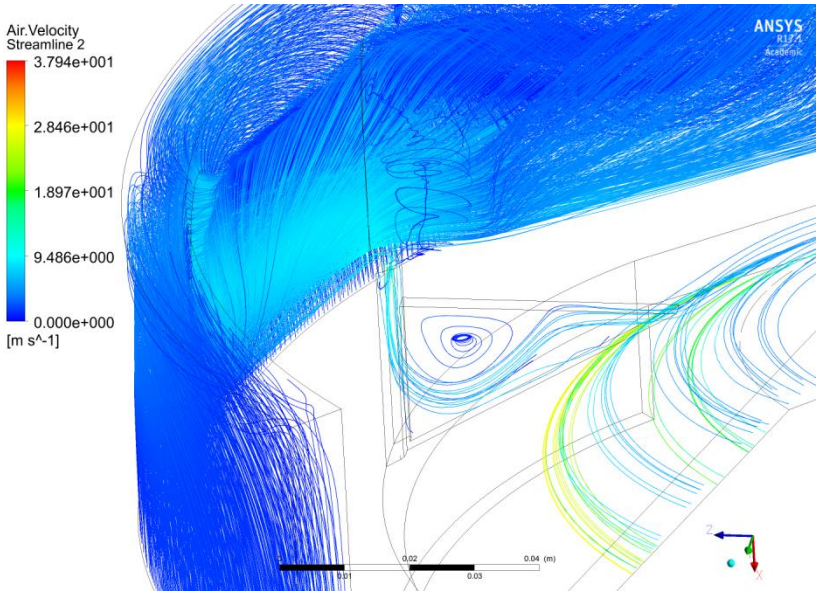

Figure 4-74: Air Stream Line for GVF $_{\text{stator jacket}}$ =8%

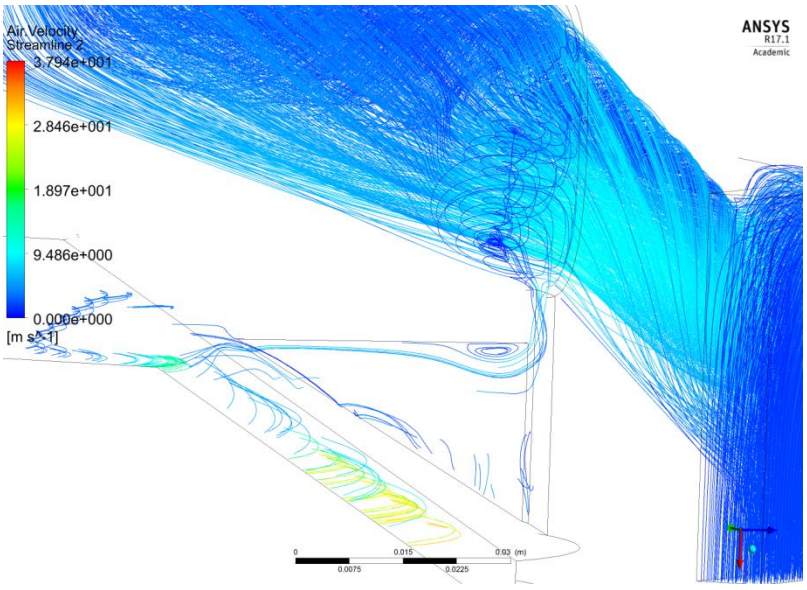

Figure 4-75: Air Stream Line for GVF $_{\text{stator jacket}}$ =20%

4.2.4 Bubble Diameter Effect

Different bubble diameter sizes are set to check its effect. The bubble diameter in this simulation is set as 0.002 inch, 0.005 inch, 0.0075 inch, 0.01 inch and 0.012 inch. The water flow rate at the inlet is set to make sure the discharge pipe water flow rate is 175 GPM, and stator jacket GVF is set to be 14%. The GVF contours for different bubble diameter set are shown in Figure 4-. For very small bubble case (d=0.002 in), the fluid is fully homogenized and well mixed. Thus, there are no large bubbles formed even in the low speed low turbulence intensity region. The largest GVF distribution in the most flow region is about 14%, the same as the inlet condition. With an increase of bubble diameter, the liquid and gas begin to separate. For large bubble case (d>=0.01 in), there is an obvious high GVF region in the thrust bearing cavity. This indicates big bubbles are concentrating

there. In the main discharge pipe area, the flow vortex also causes air concentrate near the axis and water distributed towards the outside wall.

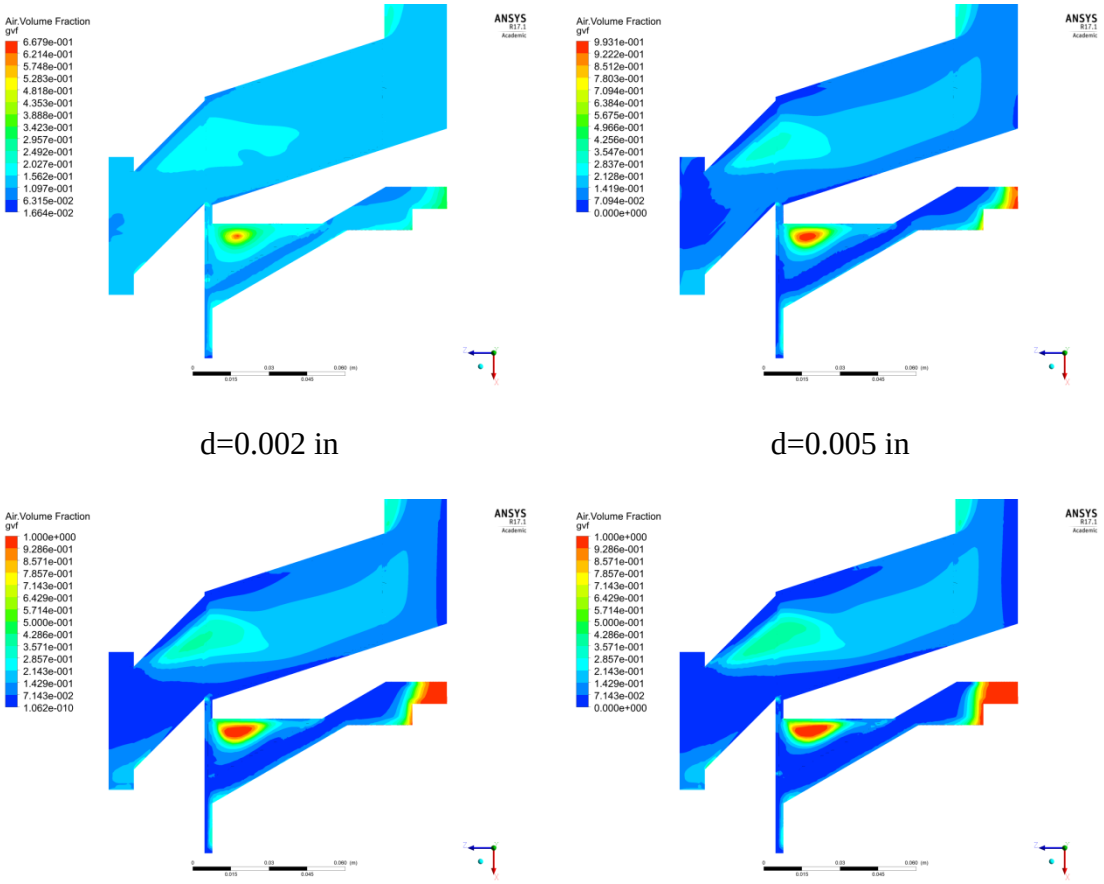

Figure 4-76: GVF Contour for Different Bubble Diameter

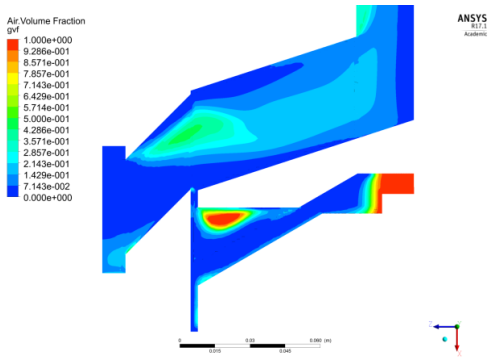

d=0.012 inch

Figure 4-76: Continued

4.2.5 Boundary Condition Parameter Study

After simulating the flow region based on boundary condition from experimental result, a parameter study is applied to evaluate the deterministic factor that affects the flow distribution. The simulated cases are listed in Table 4-1. Water inlet mass flow rate is set to 3 kg/s and rotation speed for thrust runner is 3930 RPM for all cases. Pump inlet pressure is calculated based on flow rate, pressure drop across the region and predefined outlet pressure.

First, the results for inlet air mass changing cases are shown in Figure 4-77 and Figure 4-78. Inlet GVF is chosen as representing inlet air mass flow rate since the inlet pressure doesn't change much for these cases. The pump discharge GVF increases linearly with stator jacket GVF, while thrust bearing cavity GVF change is not obvious when the stator jacket GVF is less than 15%. In Figure 4-78, the mass flow rate ratio is shown for both mixture and air. As we defined before, m^* is the mass flow rate in the thrust bearing cavity divided by stator jacket mass flow rate. m^*_a is the air mass flow rate ratio. As the stator

jacket GVF increases, mixture mass flow rate ratio doesn't obviously change. However, the air mass flow rate ratio decreases by about 50% from 7% stator jacket GVF to 15% stator jacket GVF. This indicates that m^*_a doesn't change with the stator jacket air mass flow until the stator jacket GVF is larger than 15%. After that, the air mass flow rate ratio is almost flat, this indicates that the air mass flow rate in the thrust bearing cavity outlet will increase with more stator jacket air mass flow rate. This can also be observed in Figure 4-. When the stator jacket GVF is larger than 15%, thrust bearing cavity GVF also increases with stator jacket GVF.

Parameters	Inlet Air Mass Flow Rate (kg/s)	Pump Discharge Pressure (psig)	Pump Thrust Bearing Cavity Pressure (psig)
Inlet Air Mass Flow Rate Cases	0.005, 0.0075, 0.01, 0.0125, 0.015, 0.0175, 0.02	250	240
Pump Discharge Pressure Cases	0.01	200, 210, 220, 230, 240, 250	200
Thrust Bearing Cavity Outlet Pressure Cases	0.01	250	200, 210, 220, 230, 240, 250

Table 4-1: Parameter Study on Boundary Conditions

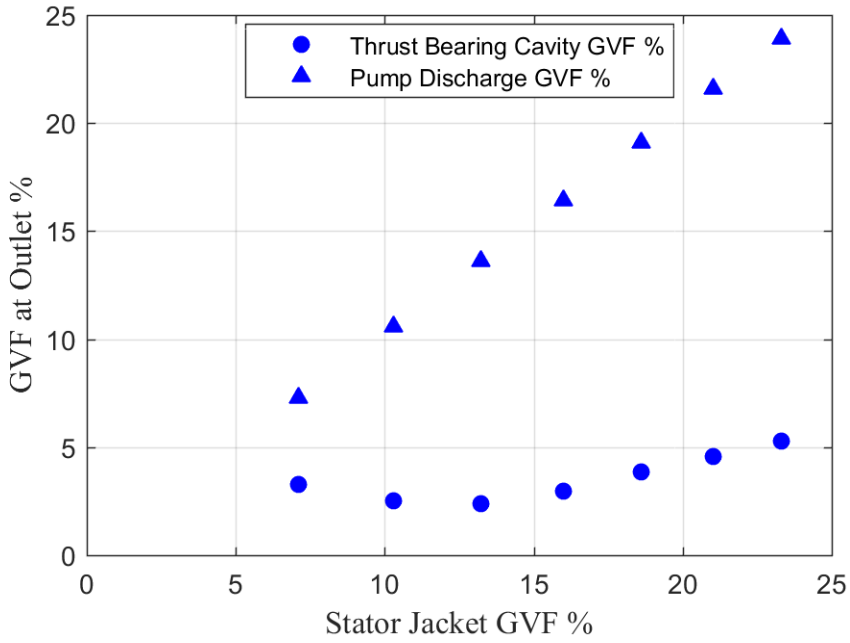

Figure 4-77: Outlet GVF vs Inlet GVF

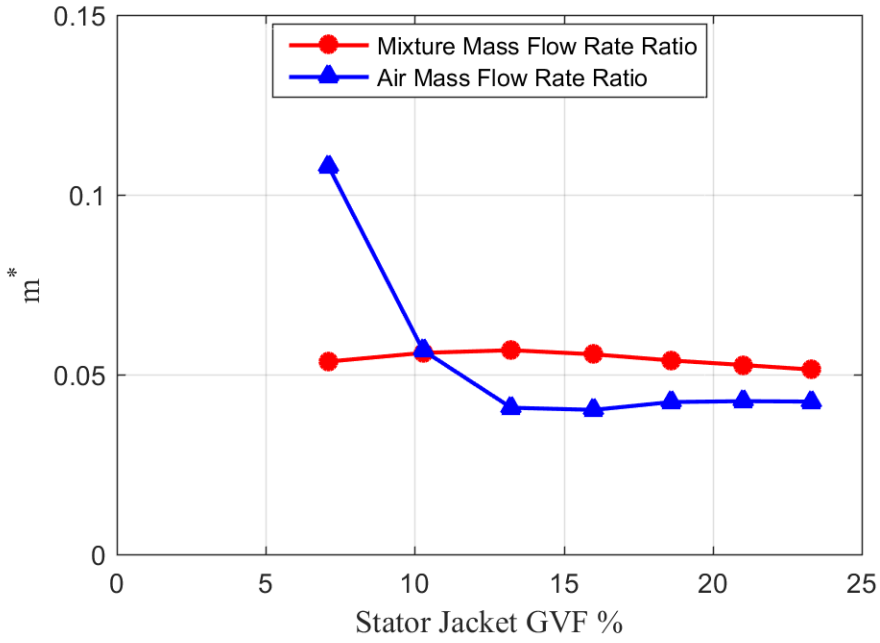

Figure 4-78: Mixture Mass Flow Rate Ratio vs Inlet GVF

In Figure 4-80 shows the GVF distribution at center cross section. As the inlet air mass flow rate increases, GVF inside the main pump discharge port increases. However, the GVF in the thrust bearing cavity doesn't increase so much. Other than that, the GVF distribution in side thrust bearing cavity shows the same trend as the previous cases.

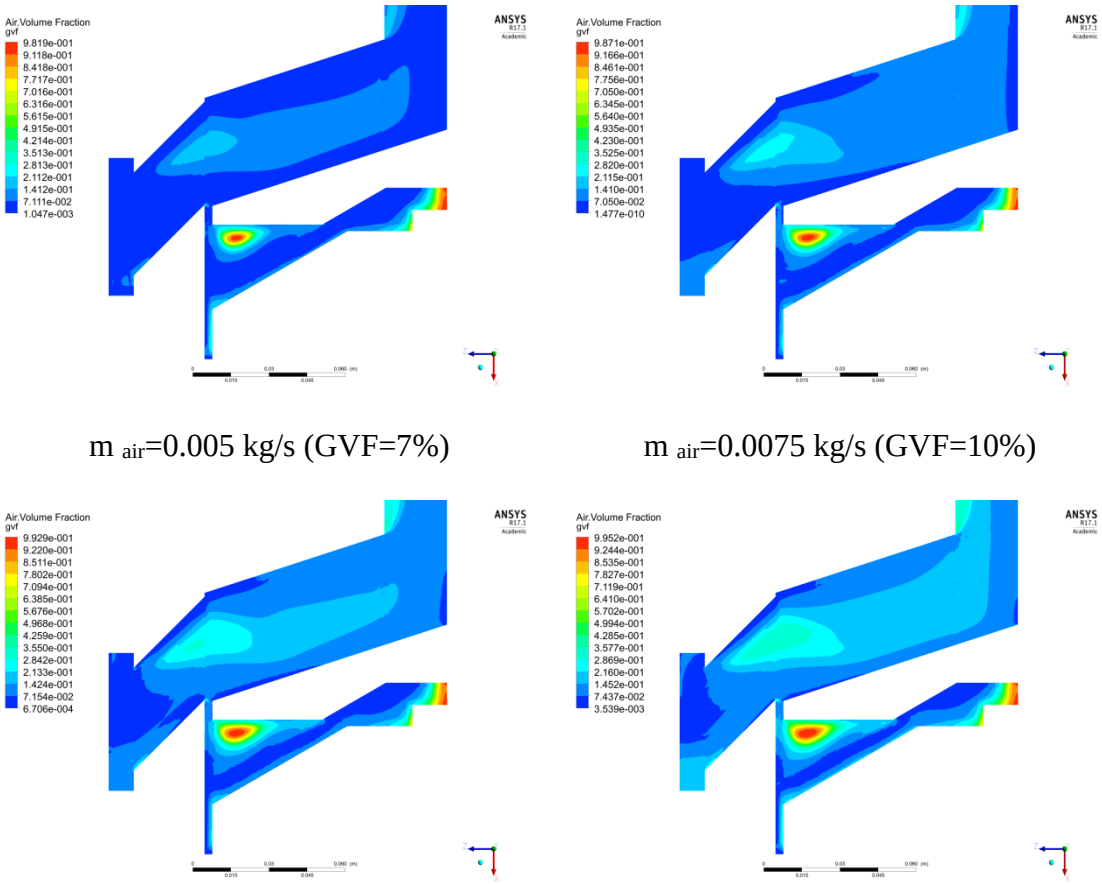

m_{air}=0.005 kg/s (GVF=7%)

m_{air}=0.0075 kg/s (GVF=10%)

m_{air}=0.01 kg/s (GVF=13%)

m_{air}=0.0125 kg/s (GVF=16%)

Figure 4-79: GVF Distribution for Different Inlet Air Mass

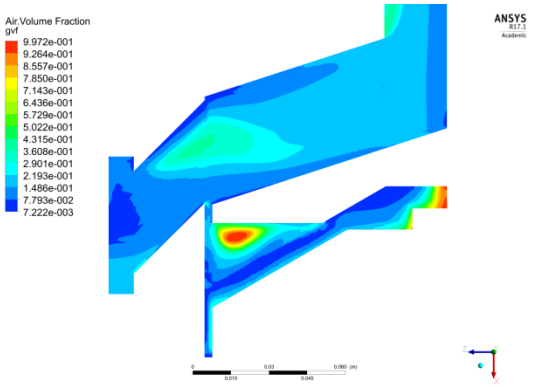

m $_{air}$=0.015 kg/s (GVF=18%)

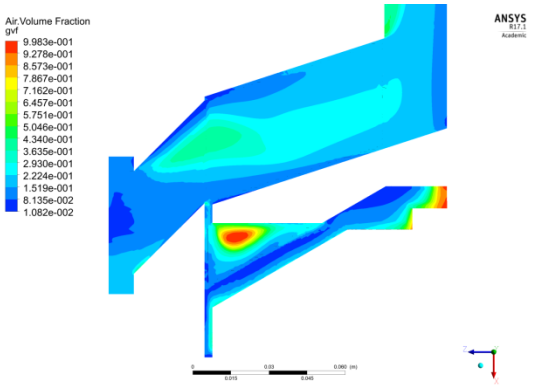

m $_{air}$=0.0175 kg/s (GVF=21%)

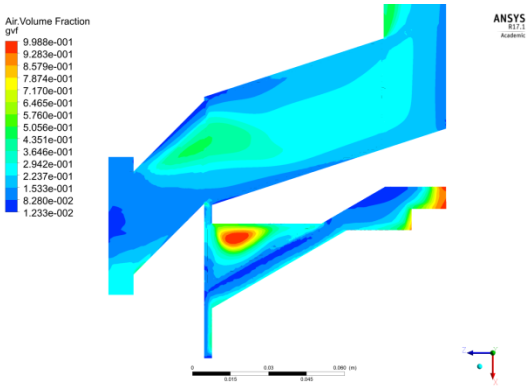

m $_{air}$=0.02 kg/s (GVF=23%)

Figure 4-79: Continued

In Figure 4-80 and Figure 4-81, the GVF and mass flow rate ratio is shown for changing outlet pressure cases. As the discharge outlet pressure is changing, the stator jacket pressure (inlet pressure) is also changing. There are about 8 psi pressure difference between stator jacket and pump discharge for all the 3 kg/s water cases. As stator jacket pressure increases, the GVF in the stator jacket and pump discharge pipe decreases since air is compressed along with the fixed mass flow rate. GVF in the thrust bearing cavity doesn't change much with the stator jacket pressure. Because the thrust bearing cavity

pressure doesn't change, thus, the pressure drop from stator jacket to thrust bearing cavity is increasing with more stator jacket pressure. This indicates that more water is flowing into the thrust bearing cavity. Thus, the mixture mass flow rate ratio increases with the stator jacket pressure. However, air mass flow rate ratio increases first, and then stays at a stable level when the stator jacket pressure increased to 240 psig. The pressure drop at this point is about 40 psi.

GVF distribution and streamlines also shows varying flow fields and corresponding GVF in Figure 4-82 and Figure 4-83. It is found that the pressure difference between the pump discharge port and the thrust bearing cavity port will result in a different flow field difference. For the thrust bearing cavity outlet pressure set at 200 psig, the pressure difference between pump discharge and thrust cavity outlet is varied, (0, 10, 20, 30, 40 and 50 psi). In Figure 4-83, when DP is 0, flow naturally diverts into two streams in the flow field. Flow velocity in the thrust bearing cavity slot is below 10 m/s. It follows the geometry change inside the slot. When DP is 10 and 20 psi, there is an obvious flow vortex region in the slot. This was already seen in the previous calculated cases. However, when DP is greater than 30 psi, the flow swirl begins to move downwards to the outlet. It is also closer to the thrust cavity wall. This causes less thrust bearing cavity GVF and mass flow rate. The GVF inside thrust bearing cavity slot becomes more averaged. No obvious high GVF concentration is found in the thrust cavity, except near the rotation axis area.

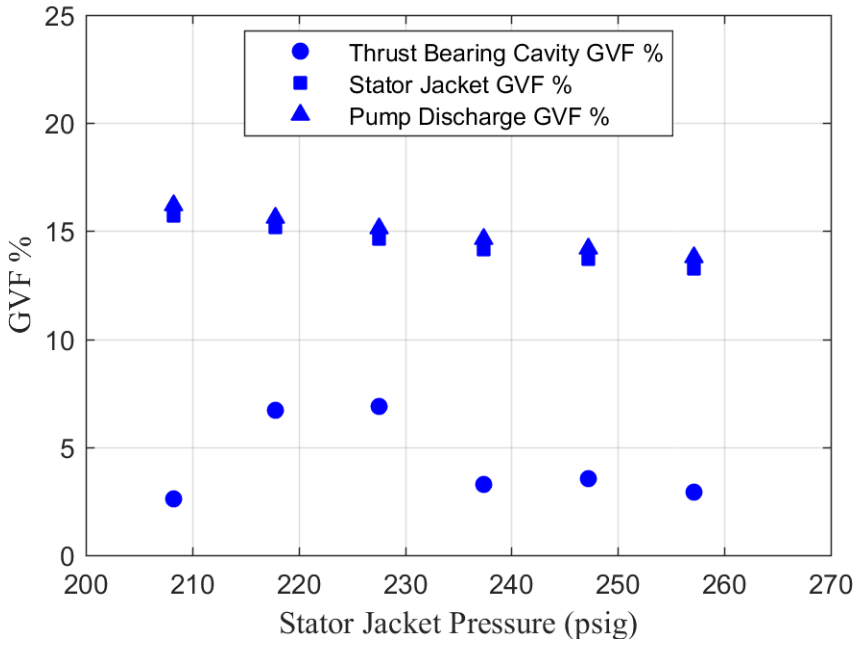

Figure 4-80: GVF at Boundary for Different Stator Jacket Pressure

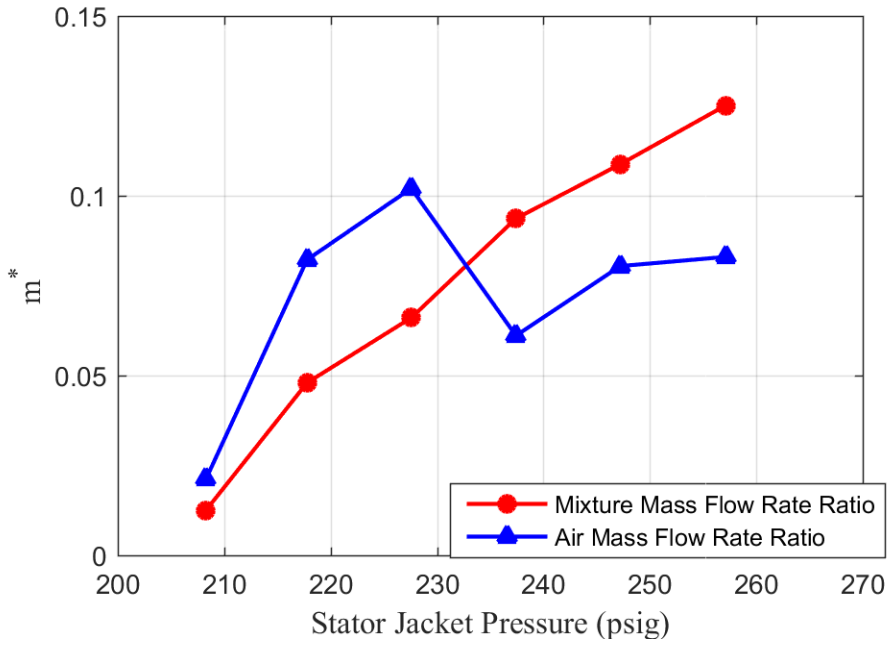

Figure 4-81: Mass Flow Rate Ratio at Boundary for Different Stator Jacket Pressure

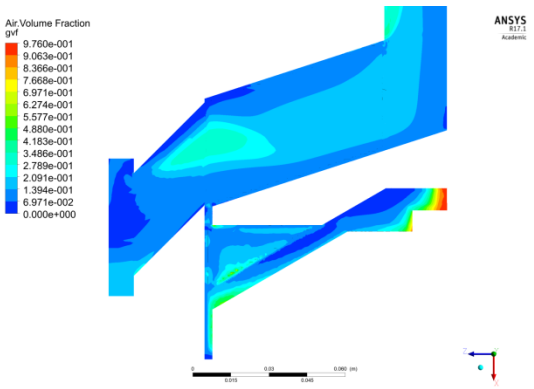

P $_{discharge}$=200 psig

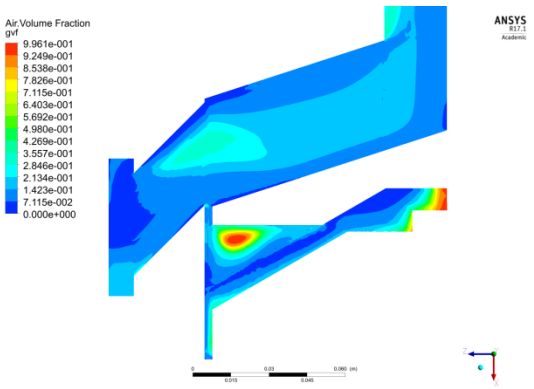

P $_{discharge}$=210 psig

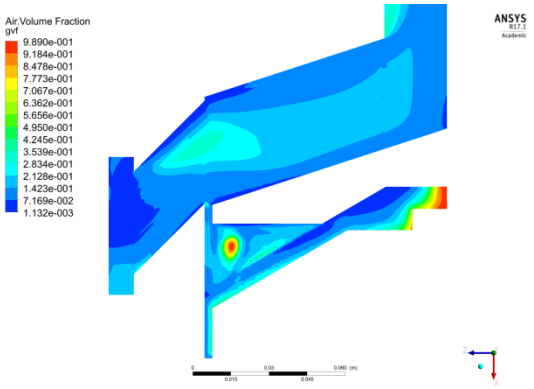

P $_{discharge}$=220 psig

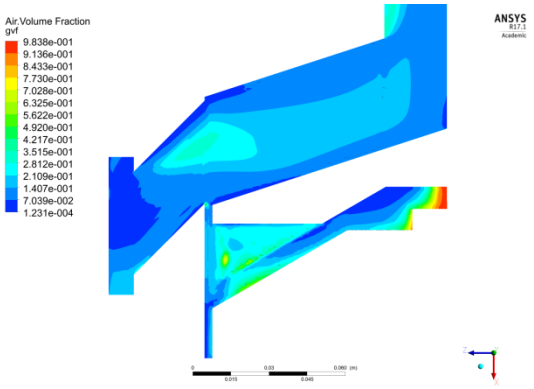

P $_{discharge}$=230 psig

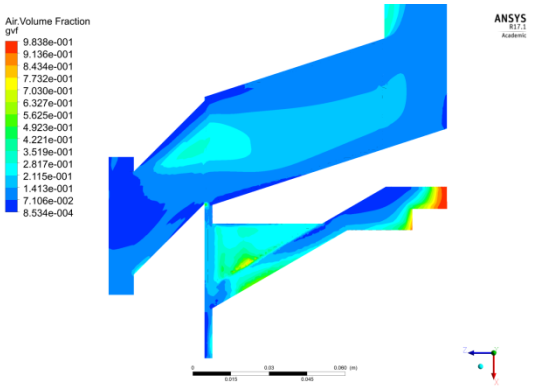

P $_{discharge}$=240 psig

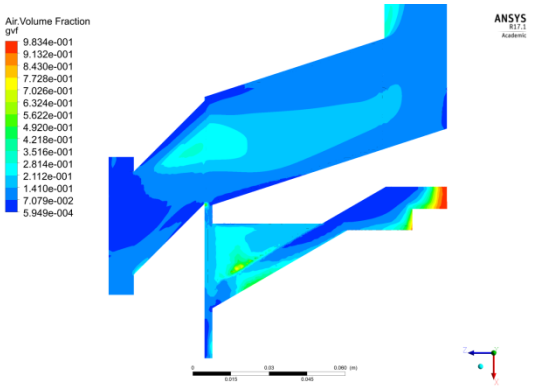

P $_{discharge}$=250 psig

Figure 4-82: GVF Distribution for Different Discharge Pressure

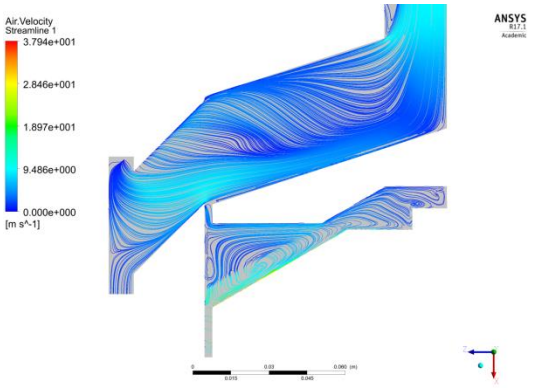

P $_{discharge}$=200 psig

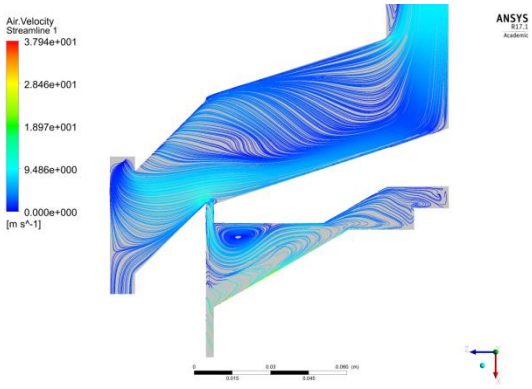

P $_{discharge}$=210 psig

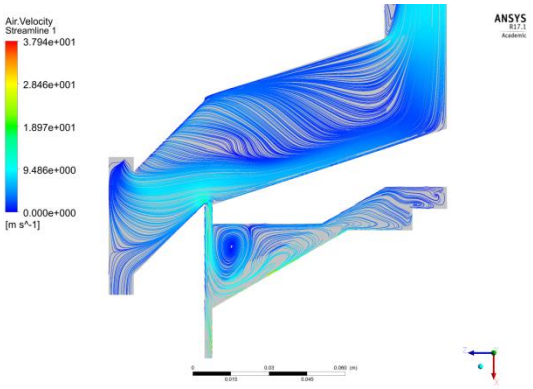

P $_{discharge}$=220 psig

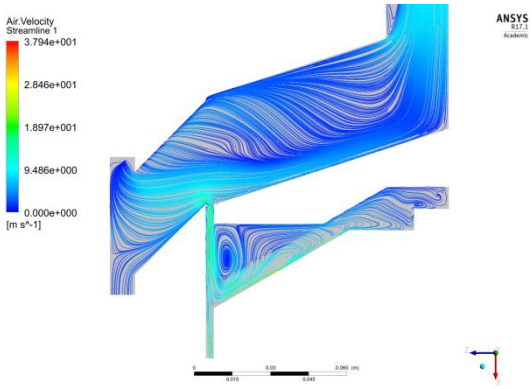

P $_{discharge}$=230 psig

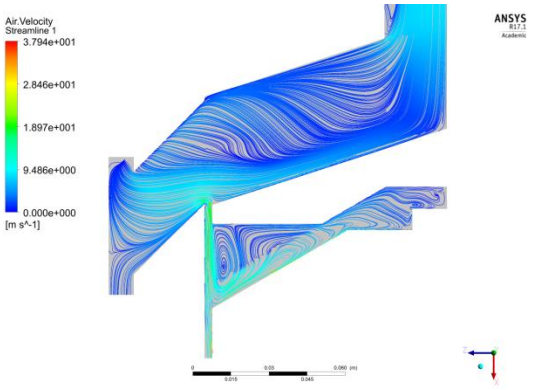

P $_{discharge}$=240 psig

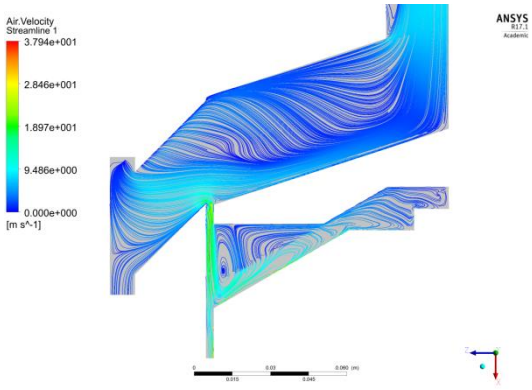

P $_{discharge}$=250 psig

Figure 4-83: Streamline for Different Discharge Pressure

In Figure 4-84 and Figure 4-85, the thrust bearing cavity pressure effect is shown. In these cases, the stator jacket pressure and pump discharge pressure do not change. Thus, with more thrust bearing cavity pressure, the pressure drop between discharge pipe and thrust bearing cavity is decreasing. Thus, less fluid will flow into the thrust bearing cavity. This is indicated from Figure 4-85. The absolute value of GVF in the thrust bearing cavity is at a relative low level (below 5%).

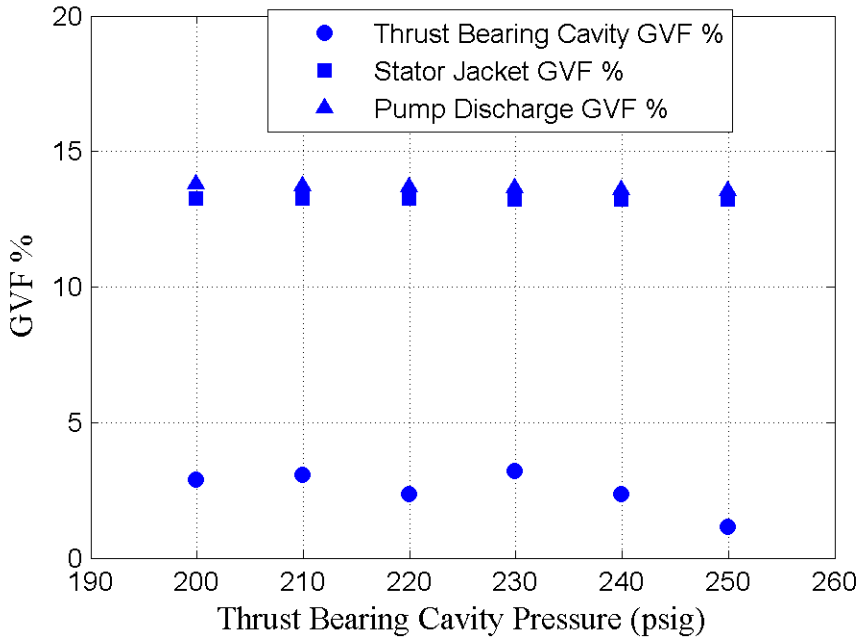

Figure 4-84: GVF for Different $P_{\text{thrust cavity}}$

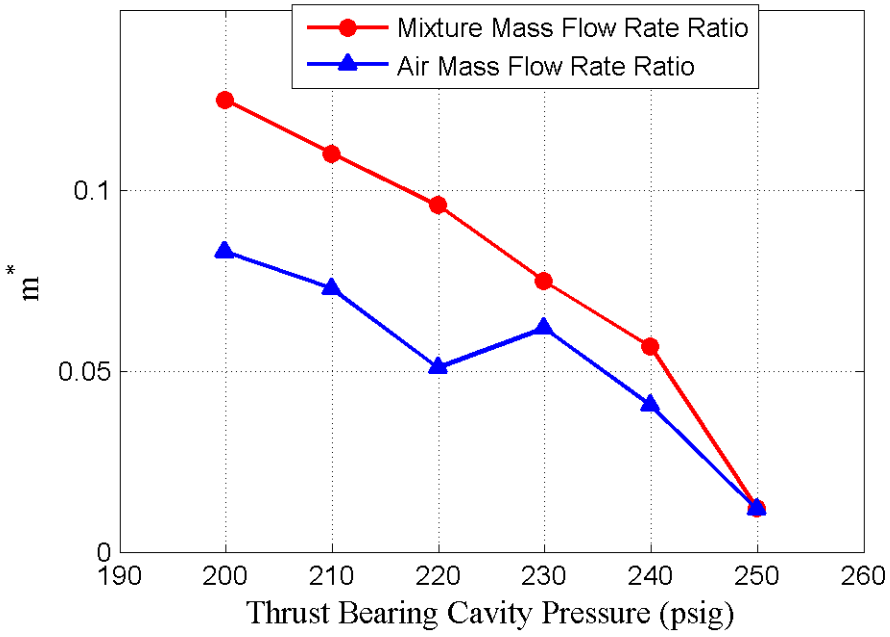

Figure 4-85: m^* for Different $P_{\text{thrust cavity}}$

4.3 Impedance Needle Probe for Multiphase Flow Measurement

Impedance needle probe calibration results are reported in this section. First, a calibration test is conducted with known water flow rate and GVF to correlate impedance probe output to the GVF.

4.3.1 Calibration Test

The calibration result of the impedance needle probe is reported in this section. During the calibration test, the impedance needle probe is installed on a 2" PVC pipe with needles pointing towards the pipe center. Also, 1.5D before the probe, there is a slotted orifice plate acting as a flow homogenizer. According to Gautham's research (Annamalai, Pirouzpanah et al. 2016), the 1.5D downstream of slotted orifice plate is the position where

multiphase flow is mostly homogenized. As described in Section 3.1.4, Y^* is applied to quantify the relative admittance of the multiphase fluid flow. It is found that when the excitation frequency is below 2 MHz, Y^* value has a linear relation with GVF within a certain range. The detailed calibration results are shown in Figure 4-86 for four different frequencies. Comparing the difference between these four frequencies, Y^* change can be neglected due to frequency change and water flow rate change. Thus, it is only GVF dependent. This will provide a good calibration parameter for GVF measurement. When excitation frequency is larger than 2 MHz, Y^* cannot be collapsed to one curve to summarize all flow conditions.

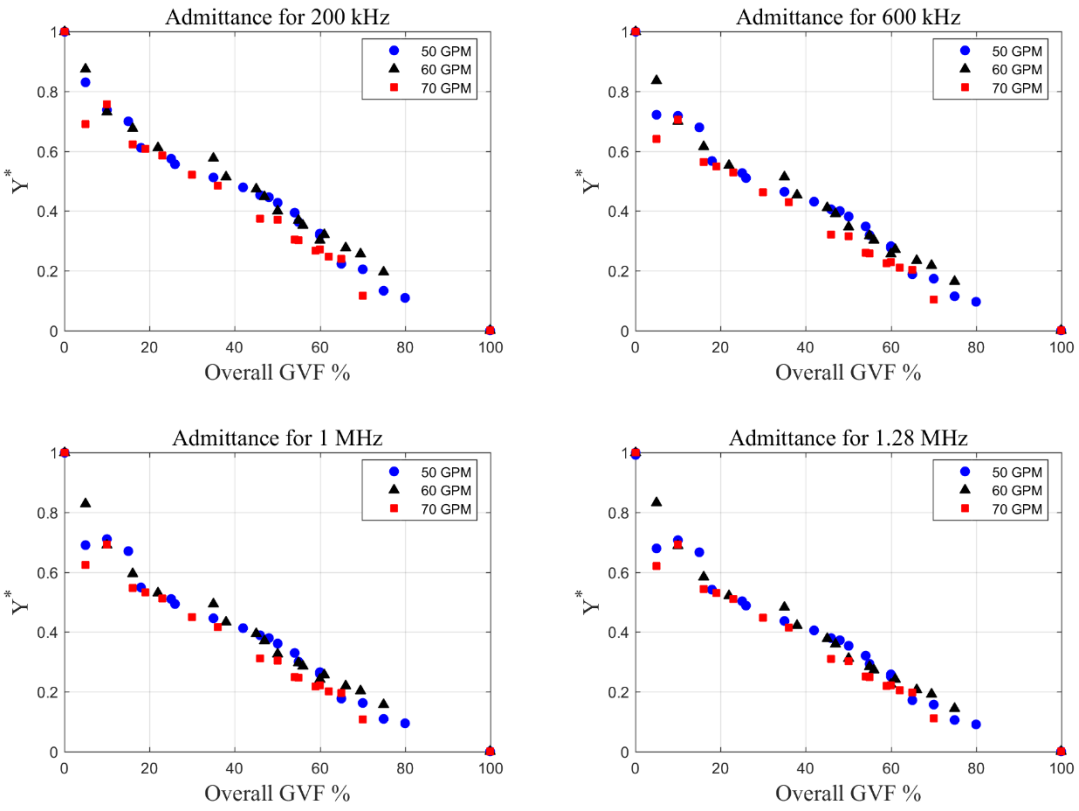

Figure 4-86: Relative Admittance Measured from Calibration Test

Figure 4-87 shows a linear curve fit of Y^* vs GVF. When GVF is less than 10%, a different curve fit should be used. When GVF=0%, by Y^* definition, it is 1. When GVF=100%, Y^* is 0. With a piecewise curve for 0%-10% and 10%-80% GVF, one can measure the GVF with measured Y^* from the impedance needle probe.

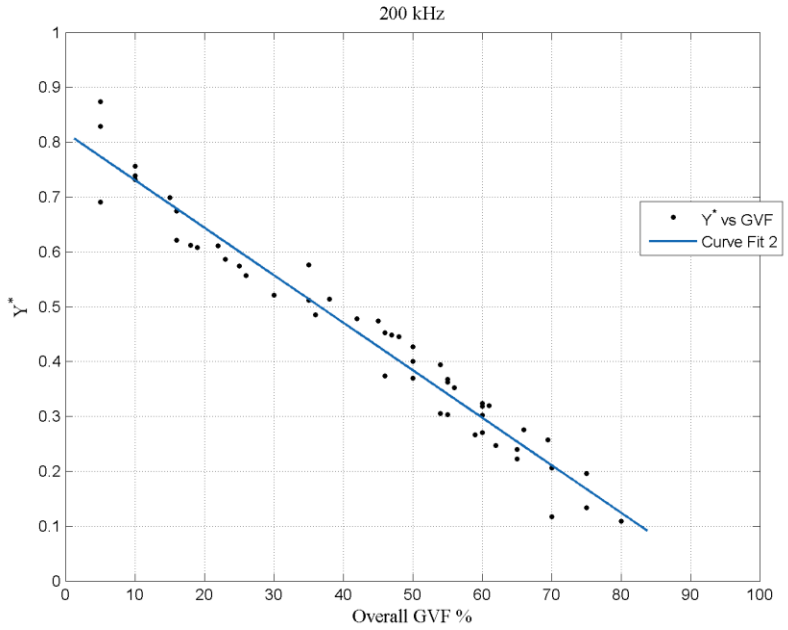

Figure 4-87: Linear Curve Fit for Y^* vs GVF

Figure 4-88 shows the phase function of CPSD between excitation signal and output signal. When the excitation frequency is 200 Hz, data can be fitted with a 2nd order polynomial expression. For frequency between 600 kHz and 1.28 MHz, $\cos(\phi/2)$ is larger than that of 200 kHz. The data can be fitted to a linear expression, especially for GVF larger than 20%.

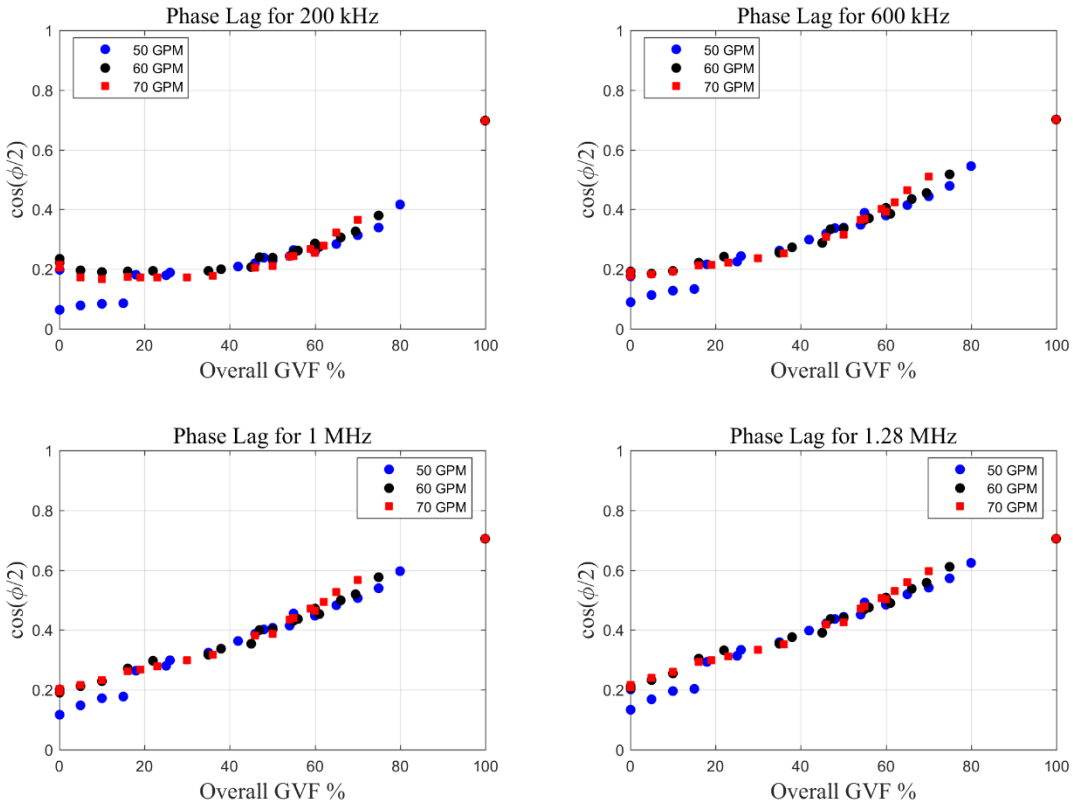

Figure 4-88: Phase of CPSD vs GVF

The CPSD (cross power spectral density) is a form of cross-correlation function between two time series signals. The phase of CPSD is the phase shift between two time series signals. When the overall GVF changes in the pipe, local GVF between the two electrodes also changes. The conductance and capacitance change the signal's transit speed, so that the phase shift between two signals also changes. While fluid's admittance measurement suffers large errors due to uncontrollable disturbance during test (fluid properties, temperature, ion concentration), it is more desirable to show the variance of GVF by calculating the phase of CPSD.

5. CONCLUSIONS AND FUTURE WORK

In this study, the experimental test of a canned motor pump under multiphase flow conditions was carried out. The multiphase CFD simulation of the canned motor pump internal flow was performed. Finally, multiphase flow measurement technique was investigated by using a needle impedance probe.

The canned motor pump was tested with water flowing through pump inlet and air injected after pump diffuser vane. The pump head and efficiency were not affected by injection of air. However, pump internal pressure distribution variance indicated that air injection changed the flow distribution between pump mainstream flow and internal cooling flow. Flow distribution change also affect the pump axial thrust force value. Higher GVF in stator jacket decreased pump internal cooling flow rate, which increased pump axial thrust force.

The canned motor pump's thermal stability was also monitored during the test. Fluid temperature was controlled in an acceptable range. Motor temperatures in different positions were monitored with different pump operation conditions and flow conditions. Results showed that GVF in stator jacket though caused fluid temperature raised in internal cooling flow; it didn't significantly affect motor temperature.

The Venturi feature in stator jacket was calibrated by measuring the pressure drop and gas liquid mixture mass flow rate. With calibration data, the Venturi feature's discharge coefficient was averaged for all calibration data. An iteration program was applied to calculate stator jacket mixture mass flow rate and stator jacket GVF based on measured

pressure drop, discharge coefficient and pump inlet flow rate. The result showed that stator jacket water flow rate increased with pump inlet flow rate, while internal flow mass flow rate ratio decreased with stator jacket GVF. This trend is consistent with the conclusion obtained from pump internal pressure distribution.

Multiphase CFD simulation was carried out to simulate the water/air mixture flow separation inside canned motor pump. The simulated flow region is a T-junction where flow in stator jacket diverts into the pump discharge port and pump thrust bearing housing. Two phase turbulence flow model was applied during the simulation in ANSYS Fluent. Water and air phase momentum equations were solved together coupling with interfacial force model. CFD results showed that most of the air in stator jacket was directed into pump discharge port. The averaged GVF at the thrust bearing cavity outlet was below 5%, even though stator jacket GVF was 20%. The flow rate distribution also indicated that higher stator jacket GVF decreased flow rate in thrust bearing cavity. Thus, the CFD prediction on flow rate trend was validated by experiment results. Bubble diameter and pressure at outlet were changed to check its effect on flow distribution. Larger bubble diameter increased GVF in the thrust bearing cavity. The pressure difference between pump discharge and thrust bearing cavity determined the flow field inside the thrust bearing cavity. With higher velocity in thrust bearing cavity slot, flow separation vortex occurred and formed large air bubbles at the vortex center.

The multiphase flow measurement in a pipe flow is also a part of this study. The needle impedance probe was designed and built for easy installation on a pipe. Multiphase flow

tests were carried out to calibrate the probe's output signal. Two parameters can be correlated with GVF in a pipe flow: admittance of multiphase mixture and phase of CPSD. The calibration results showed that dimensionless admittance had a linear relation with GVF at 10%-80% for 200 kHz case. The phase of CPSD showed less uncertainty and also linear relation with GVF at 20%-80% for 200 kHz to 1.28 MHz. It is concluded that the phase of CPSD is a promising parameter to measure the GVF.

Future work can be addressed in the following respects: (1) The canned motor pump's rotor orbits will be better measured at the thrust bearing cavity and hub plate cavity rather than at the impeller disk. The improved rotor orbits combining accelerometer data will provide more depth knowledge on canned motor pump's operation under multiphase flow. (2) The phase of CPSD correlating with GVF has not been found in any existing literatures. Thus, it is recommended that more flow regimes should be tested to check its correlation with this parameter.

REFERENCES

Alexandrina Untaroiu, T. W. D., Paul E. Allaire, Richard Armentrout (2009). "Cfd Analysis of a Canned Pump Rotor Considering an Annular Fluid with Axial Flow." Orlando, Florida, USA, Proceedings of ASME Turbo Expo 2009: Power for Land, Sea and Air. **Volume 6: Structures and Dynamics, Parts A and B:** pp. 1013-1022.

Andreussi, P., A. Di Donfrancesco and M. Messia (1988). "An Impedance Method for the Measurement of Liquid Hold-up in Two-Phase Flow." International Journal of Multiphase Flow **14**(6): 777-785.

Annamalai, G., S. Pirouzpanah, S. R. Gudigopuram and G. L. Morrison (2016). "Characterization of Flow Homogeneity Downstream of a Slotted Orifice Plate in a Two-Phase Flow Using Electrical Resistance Tomography." Flow Measurement and Instrumentation **50**: 209-215.

Azzopardi, B. J. and P. A. Smith (1992). "Two-Phase Flow Split at T Junctions: Effect of Side Arm Orientation and Downstream Geometry." International Journal of Multiphase Flow **18**(6): 861-875.

Azzopardi, B. J. and P. B. Whalley (1982). "The Effect of Flow Patterns on Two-Phase Flow in a T Junction." International Journal of Multiphase Flow **8**(5): 491-507.

Buel, J. R., H. M. Soliman and G. E. Sims (1994). "Two-Phase Pressure Drop and Phase Distribution of a Horizontal Tee Junction." International Journal of Multiphase Flow **20**(5): 819-836.

Charron, Y. and P. B. Whalley (1995). "Gas-Liquid Annular Flow at a Vertical Tee Junction—Part I. Flow Separation." International Journal of Multiphase Flow **21**(4): 569-589.

Corneliussen, S., Couput, Jean-Paul, Dahl, Eivind, Dykesteen, Eivind (2005). Handbook of Multiphase Flow Metering, Rev. 2, Norwegian Society for Oil and Gas Measurement.

Devia, F. and M. Fossa (2003). "Design and Optimisation of Impedance Probes for Void Fraction Measurements." Flow Measurement and Instrumentation **14**(4-5): 139-149.

Fossa, M. (1998). "Design and Performance of a Conductance Probe for Measuring the Liquid Fraction in Two-Phase Gas-Liquid Flows." Flow Measurement and Instrumentation **9**(2): 103-109.

Hagen, O. (1969). "Paper 9: Canned Motor Pump Design." Proceedings of the Institution of Mechanical Engineers **184**(11): 88-97.

Hogsett, S. and M. Ishii (1997). "Local Two-Phase Flow Measurements Using Sensor Techniques." Nuclear Engineering and Design **175**(1–2): 15-24.

Hwang, S. T., H. M. Soliman and R. T. Lahey (1988). "Phase Separation in Dividing Two-Phase Flows." International Journal of Multiphase Flow **14**(4): 439-458.

Ishii, M. (1971). Thermally Induced Flow Instabilities in Two-Phase Mixtures in Thermal Equillibrium, PhD. Dissertation.Georgia Institute of Technology, Atlanta, Georgia.

Ishii, M. and N. Zuber (1979). "Drag Coefficient and Relative Velocity in Bubbly, Droplet or Particulate Flows." AIChE Journal: 843-855.

Ishii, M. H., Takashi (2011). Thermo-Fluid Dynamics of Two-Phase Flow, Springer-Verlag New York.

Kisner, R., D. Fugate, A. Melin, D. Holcomb, D. Wilson, P. Silva and C. C. Molina (2013). "Evaluation of Manufacturability of Embedded Sensors and Controls with Canned Rotor Pump System." United States. , UNT Digital Library. http://digital.library.unt.edu/ark:/67531/metadc839101/. .

Li, J., J. T. Song and Y. H. Cho (2010). "Thermal Analysis of Canned Induction Motor for Coolant Pump Considering the Eddy Current Loss in Cans." Material Science Forum (Volume 670)**:** 466-476.

Liao, Y., D. Lucas, E. Krepper and M. Schmidtke (2011). "Development of a Generalized Coalescence and Breakup Closure for the Inhomogeneous Musig Model." Nuclear Engineering and Design **241**(4): 1024-1033.

Lo, S. (1996). "Application of the Musig Model to Bubbly Flows." AEA Technology: AEAT-1096.

Lucas, D., E. Krepper and H.-M. Prasser (2007). "Use of Models for Lift, Wall and Turbulent Dispersion Forces Acting on Bubbles for Poly-Disperse Flows." Chemical Engieering Science **62**(15): 4146-4157.

Luo, H. and H. F. Svendsen (1996). "Theoretical Model for Drop and Bubble Break-up in Turbulent Flows." AlChE Journal **42**(5): 1225-1233.

Mandhane, J. M., G. A. Gregory and K. Aziz (1974). "A Flow Pattern Map for Gas—Liquid Flow in Horizontal Pipes." International Journal of Multiphase Flow **1**(4): 537-553.

Morrison, G. L., K. R. Hall, J. C. Holste, M. L. Macek, L. M. Ihfe, R. E. DeOtte and D. P. Terracina (1994). "Comparison of Orifice and Slotted Plate Flowmeters." Flow Measurement and Instrumentation **5**(2): 71-77.

Morrison, G. L., D. Terracina, C. Brewer and K. R. Hall (2001). "Response of a Slotted Orifice Flow Meter to an Air/Water Mixture." Flow Measurement and Instrumentation **12**(3): 175-180.

Mudde, R. F., J. S. Groen and H. E. A. van den Akker (1993). "Two-Phase Flow Redistribution Phenomena in a Large T-Junction." International Journal of Multiphase Flow **19**(4): 563-573.

Munholand, L. and G. Soucy (2005). "Comparison of Four Conductive Needle Probe Designs for Determination of Bubble Velocity and Local Gas Holdup." Review of Scientific Instruments **76**(9): 095101.

Paranjape, S., S. N. Ritchey and S. V. Garimella (2012). "Electrical Impedance-Based Void Fraction Measurement and Flow Regime Identification in Microchannel Flows under Adiabatic Conditions." International Journal of Multiphase Flow **42**: 175-183.

Powell, R. L. (2008). "Experimental Techniques for Multiphase Flows." Physics of Fluids **20**(4): 040605.

Prince, M. J. and H. W. Blanch (1990). "Bubble Coalescence and Break-up in Air-Sparged Bubble Columns." AlChE Journal **36**(10): 1485-1499.

Ruddy, A. V. (1980). "An Analysis of the Effect of Journal Bearings with Helical Grooves on the Stability of a Vertically Mounted Canned Motor Pump." Tribology International **13**(5): 237-241.

Rzehak, R. and S. Kriebitzsch (2015). "Multiphase Cfd-Simulation of Bubbly Pipe Flow: A Code Comparison." International Journal of Multiphase Flow **68**: 135-152.

Sahand Pirouzpanah, G. L. M. (2013). Temporal Gas Volume Fraction and Bubble Velocity Measurement Using an Impednace Needle Probe. ASME 2013 Fluid Engineering Division Summer Meeting, Incline Village, Nevada, USA.

Schleicher, E., M. J. D. Silva and U. Hampel (2008). "Enhanced Local Void and Temperature Measurements for Transient Multiphase Flows." IEEE Transactions On Instrumentation And Measurement **57**(2): 401-405.

Shoham, O., S. Arirachakaran and J. P. Brill (1989). "Two-Phase Flow Splitting in a Horizontal Reduced Pipe Tee." Chemical Engineering Science **44**(10): 2388-2391.

Shoham, O., J. P. Brill and Y. Taitel (1987). "Two-Phase Flow Splitting in a Tee Junction—Experiment and Modelling." Chemical Engineering Science **42**(11): 2667-2676.

Sihombing, D. J. (2015). Temperature Effect in Multiphase Flow Meter Using Slotted Orifice Plate Master's thesis, Texas A&M University.

Silva, M. J. D. (2008). Impedance Sensors for Fast Multiphase Flow Measurement and Imaging Doctor's Dissertation, Technische Universität Dresden.

Silva, M. J. D., E. Schleicher and U. Hampel (2007). "A Novel Needle Probe Based on High-Speed Complex Permittivity Measurements for Investigation of Dynamic Fluid Flows." IEEE Transactions On Instrumentation And Measurement **56**(4): 1249-1256.

Stark, M. and G. E. Bollibon (1967). US3475631 A.

Takacs, G. (2009). Electrical Submersible Pumps Manual: Design, Operations, and Maintenance. Oxford, Gulf Professional Publishing/Elsevier.

Thomas, H. and S. Michael (1967). US3450056 A.

Uga, T. (1972). "Determination of Bubble-Size Distribution in a Bwr." Nuclear Engineering and Design **22**(2): 252-261.

Walters, L. C., H. M. Soliman and G. E. Sims (1998). "Two-Phase Pressure Drop and Phase Distribution at Reduced Tee Junctions." International Journal of Multiphase Flow **24**(5): 775-792.

Wang, X. and X. Sun (2009). "Cfd Simulation of Phase Distribution in Adiabatic Upward Bubbly Flows Using Interfacial Area Transport Equation." Nuclear Technology **167**(1): 71-82.

Yamoah, S., R. Martinez-Cuenca, G. Monros, S. Chiva and R. Macian-Juan (2015). "Numerical Investigation of Models for Drag, Lift, Wall Lubrication and Turbulent Dispersion Forces Forthe Simulation of Gas–Liquid Two-Phase Flow." Chemical Engineering Research and Design **98**: 17-35.